Characterization of Composites with Aligned Carbon Nanotubes (CNTs) as Reinforcement

by

Enrique J. García

B.Eng + M.Eng. (Mechanical)
Universidad de Zaragoza, Spain

DEA (Mechanical)
Universidad de Zaragoza, Spain; Université de Pau, France;
École de Mines de Douai, France; University of North London, UK

Submitted to the Department of Aeronautics and Astronautics
in partial fulfillment of the requirements for the degree of

Master of Science in Aeronautics and Astronautics

at the

MASSACHUSETTS INSTITUTE OF TECHNOLOGY

May 2006

Author …….
Department of Aeronautics and Astronautics
May 20, 2006

Certified by ……
Brian L. Wardle
Boeing Assistant Professor
Thesis Supervisor

Accepted by …….
Jaime Peraire
Professor of Aeronautics and Astronautics
Chair, Committee on Graduate Students

Characterization of Composites with Aligned Carbon Nanotubes (CNTs) as Reinforcement

by

Enrique J. García

Submitted to the Department of Aeronautics and Astronautics
in partial fulfillment of the requirements for the degree of
Master of Science in Aeronautics and Astronautics

Abstract

Carbon nanotubes' (CNTs) superlative combination of electrical, thermal, and especially mechanical properties make them ideal candidates for composite reinforcement. Nanocomposites and hybrid composite architectures employing traditional advanced composites and CNTs offer significant potential mechanical and multifunctional performance benefits. CNT/polymer composites and two different hybrid architectures are experimentally investigated in this work. A novel process for rapidly growing dense, long, high-quality aligned CNT forests is employed. The first architecture is comprised of aligned fibers with CNTs grown radially on their surface. For the second architecture, dense forests of vertically aligned CNTs are placed between the plies of a laminate, in the through-thickness direction. Fundamental issues related to realizing hybrid composite architectures are investigated experimentally: wetting of the CNTs by commercially available polymers for the different architectures, effective reinforcement of the polymer matrices due to the addition of CNTs, and retention of mechanical (stiffness and strength) properties of the fibers after the CNT growth process. Wetting of CNT forests by several commercial polymers (including a highly-viscous epoxy) is demonstrated at rates conducive to creating a fully-dispersed CNT/matrix region for the two hybrid architectures previously described. Direct measurements of the mechanical properties of nanocomposites are reported for the first time in the literature. Increases in the Young's modulus of the polymer as high as 220% with just 2% volume fraction of aligned CNTs are observed. Equivalent reinforcement had been obtained previously by other authors with 5% volume fraction of randomly oriented CNTs. Single-fiber tension tests indicate no mechanical degradation (stiffness and strength) for alumina fibers undergoing the CNT growth process. Preliminary results on the fabrication of the two hybrid architectures are also presented. All the experimental results presented in this work indicate that hybrid CNT/composite architectures are feasible and future work focuses on mechanical and multifunctional property characterization of these and other hybrid architectures, and scaling to a continuous CNT growth process.

Thesis Supervisor: Brian L. Wardle
Title: Boeing Assistant Professor

Acknowledgments

This thesis would not be complete without thanking everyone that helped me and supported me for the last two years. It is impossible to put into words my gratitude to all of you, so, please, excuse me if I am not able to transmit my appreciation in these few lines.

First to my supervisor, Brian L. Wardle, who has not only been the most effective anchor during my research, but also a true colleague in this endeavor: thank you for your guidance and especially for your positiveness and support when results were elusive. Thank you for believing in this project and in me, and for everything I have learnt from you. Your dedication, motivation, and insight have been fundamental in the success of this project. I wish you all the best in the future.

Second, to the people who worked with me at different points of the research, thank you for your motivation and insight: to A. John Hart, Sunil D. Gouda, and Katrina Sorensen. This would not have been possible without your work and dedication.

To Alan Schwartzman from MIT´s Nanolab, Kurt Broderick and the rest of the staff at MTL, and especially to John Kane from TELAMS, thank you so much for your invaluable help to develop the processes and tests that conform this research. Your insightful knowledge and hands-on experience make MIT excel.

Next, I would like to thank the people who had to deal with me every day (and some nights): my lab mates. Thank you all for the support and advice, the hard work and the laughs we shared.

To my friends, here, in Spain, and around the world, thank you for your constant support at every moment, especially in the downsides. Thank you for never letting me down.

To my family, who has been behind me from the very beginning and supported me when I decided to completely change my life moving from industry back to school. Thank you for your love and support through the years and for letting me live my dream.

Of course, to Ana, I will never be able to thank you enough for sharing with me this amazing experience at the other end of the phone, for your endless support and for believing in me. I hope I will be able to repay you and to let you know how much all your help has meant to me in the past and especially over the last two years!

Last, and most importantly, I want to thank the Lord my God, who has given me both the ability and opportunity - undeserving - to live my dreams.

The author would like to acknowledge the Fundación La Caixa, which awarded the scholarship that has made all this possible.

Dedico este trabajo a mi familia al completo, por el infinito apoyo que he recibido en todo momento y en especial a mi madre, a mi padre, a mi hermana y a Ana, mi paciente novia. ¡Esto no hubiese sido posible sin vosotros!

This work is dedicated to my entire family, for the infinite support they transmitted me all the time, and especially to my mother, my father, my sister, and my patient girlfriend, Ana. This would have not been possible without you!

Contents

List of Figures

List of Tables

List of Symbols

Symbol	Description	Units
D_0	External diameter in a MWCNT	[nm]
E^b	Bending elastic modulus of a CNT	[GPa]
E^a	Axial elastic modulus of a CNT	[GPa]
E^w	Wall elastic modulus of a CNT	[GPa]
$Ø_{int}$	Diameter of the inner wall of a MWCNT	[nm]
$Ø_{ext}$	Diameter of the outer wall of a MWCNT	[nm]
H	Material hardness	[GPa]
P_{max}	Maximum load applied by the nanoindenter	[mN]
A	Projected area of indentation	[nm^2]
h_p	Depth of penetration (Berkovich nanoindentation)	[nm]
θ	Face angle of the indenter	[deg]
a	Radius of the circle that defines the contact area in spherical nanoindentation	[µm]
R	Radius of the spherical indenter	[µm]
S	Contact stiffness in nanoindentation unloading	[N/m]
P	Load applied by the nanoindenter	[mN]
β	Nanoindentation geometry constant	-
E_r	Reduced elastic modulus for nanoindentation	[GPa]
E	Longitudinal Young's modulus of the specimen	[GPa]
v	Longitudinal Poisson's ratio of the specimen	-

E_i	Isotropic Young's modulus of the indenter	[GPa]
ν_i	Isotropic Poisson's ratio of the indenter	-
ε	Geometry correction factor for nanoindentation	-
$E_{nanocomp}$	Longitudinal Young's modulus of the nanocomposite	[GPa]
E_{CNT}	Longitudinal Young's modulus of the CNT	[GPa]
V_{CNT}	Volume fraction of CNTs	-
E_{matrix}	Isotropic Young's modulus of the polymer matrix	[GPa]
d_{nc}	Diameter of the nanocomposite pillar after contraction	[µm]
D_{nc}	Diameter of the nanocomposite pillar at its base (original diameter of the CNT pillar)	[µm]
h_{nc}	Height of the regularly contracted part of the nanocomposite pillar	[µm]
H_{nc}	Height of the transition region of the nanocomposite pillar	[µm]
x	Stress	[MPa]
$p(x)$	Probability of failure of the fiber at a particular stress, x	
S	Standard deviation of tensile strength	[MPa]
$\bar{x}$	Average tensile strength	[MPa]
α	Scale factor of the Weibull distribution	-
β	Location parameter of the Weibull distribution	[MPa]

Chapter 1. Introduction

1.1 Composites Using Carbon Nanotubes (CNTs)

Carbon nanotubes (CNTs) have been the focus of considerable research since their discovery by Iijima in 1991 [1]. Numerous studies have proven their impressive electronic properties, such as a capacity of carrying electric current 1000x higher than copper wires [19]-[20]. CNTs also have outstanding thermal properties. Ruof and Lorents measured thermal stability up to 2800 ºC, and thermal conductivity about twice as high as diamond [21]. These properties have been investigated for electronic devices. In addition to the exceptional electronic and thermal properties associated with carbon nanotubes, they also posses exceptional mechanical properties [22]-[44]: Theoretical and experimental results point to an elastic modulus higher than 1 TPa, compared to 0.2 TPa for steel and 0.07 TPa for aluminum, and strengths 10 to 100 times higher than the strongest steel at a fraction of the weight [2]. Due to their remarkable mechanical properties many researchers have focused on using carbon nanotubes as reinforcement for different materials.

Reinforcement of different matrices through the use of carbon nanotubes and nanoclays has been a major focus of research around the world. The problems associated with large filler particles (mainly stress concentrations) are considerably reduced due to

the size of the nanotubes. Moreover, no other filler provides such a high strength and stiffness combined with a low density. Analytical models and extensive work on reinforcement of polymer, ceramic, and metal matrices have been developed in the last few years.

Carbon nanotubes have also been studied as reinforcement for traditional composite materials. The outstanding mechanical properties of composite materials have allowed them to increase their presence in the aeronautical industry in the last 20 years. Composite materials have mechanical properties comparable to those of the best metal alloys but with about a third of the weight. Because of their exceptional in-plane mechanical properties, multilayered composite materials are effectively used in structural parts traditionally reserved for metal alloys. However, the relatively poor mechanical properties of the matrix and the fiber/matrix interfacial bond limit their use in particularly demanding applications. Composite materials fail through numerous modes at various lenghtscales. Carbon nanotubes increase the capacity of load transfer between matrix and fiber: On the one hand, they reinforce the matrix, increasing its load-carrying capability; on the other hand, they increase the effective interface area, favoring the load transfer.

Composite laminates contain matrix-rich regions that reduce their overall performance. In composite laminates, the thin, unreinforced pure matrix layer that exists between plies has poor mechanical properties (stiffness, strength, fracture toughness) when compared to in-plane properties of the laminate. Delamination and matrix cracking between plies are the dominant modes of damage and therefore responsible for the reduction of properties in the direction normal to the plane. In recent years several different solutions have tried to overcome this limitation: 3D-braiding, weaving and

stitching (*e.g.*, z-pinning) are the most promising solutions to date. All these processes increase to some extent the through-thickness mechanical properties of layered composite materials, but also reduce the laminate's performance in the in-plane directions of the laminate [75]-[83]. A possible method to increase a composite's resistance to delamination without compromising the in-plane properties is the use of carbon nanotubes (CNTs) in the interface between layers that would not only improve the mechanical properties of the inter-ply region, but also can help reduce the crack propagation by bridging the two plies across the crack.

1.2 Overview of Thesis

The focus of this research is on exploiting CNT's outstanding nanoscale properties toward the development of macroscopic structural materials. This work focuses on polymer-matrix composites because of the extensive number of present applications. As mentioned previously, carbon nanotubes have superior mechanical, electrical, and thermal properties, which make them a perfect candidate for multifunctional composite materials. Though the study of multifunctional composites using carbon nanotubes is extremely interesting, there are too many unknowns in their design that must be solved before being able to take full advantage of the outstanding combination of properties that carbon nanotubes offer. Importantly for this research, the mechanical properties of CNT/polymer and CNT/polymer/fiber composites have not been completely determined yet. Taking all these considerations into account, the focus of this research is the mechanical characterization of polymer based composites using

carbon nanotubes and their possible use in structural applications. Specific objectives of this project are:

- Preliminary investigation of the wide potential of the CNTs for mechanical reinforcement. The wide potential stems from the numerous architectures of CNT/polymer matrix/advanced fibers that have been identified.
- Determine experimentally the effectiveness of the wetting of carbon nanotubes by different polymer matrices, using different wetting processes and polymers.
- Obtain direct measurements of the mechanical properties (Young's modulus and strength) of CNT/polymer nanocomposites.
- Explore two different architectures for hybrid composites containing carbon nanotubes, advanced fibers, and polymer matrices.
- Develop experimental setups and fabrication processes for several hybrid architectures to verify their feasibility.
- Develop fabrication and characterization of hybrid multilayered composites containing CNTs in the plies' interface. This research will also address the viability of a continuous process to fabricate CNT-reinforced prepregs.

The approach taken in this work is mainly experimental. Wetting of the CNTs with different polymer matrices were studied on CNTs grown in the form of dense forests and also in the form of pillars of different sizes and shapes. The mechanical properties of the CNT/polymer nanocomposites were tested using a nanoindenter and a flat punch to apply a compression test on nanocomposite (CNT/polymer) pillars. Two different hybrid architectures were studied to address the issues associated with traditional composites

described previously: Forests of carbon nanotubes placed vertically between plies of traditional composite materials, and carbon nanotubes grown on the surface of advanced fibers and wet by a polymer matrix. For both hybrid architectures the wetting of the CNTs with polymer matrices was carefully explored experimentally.

The following aspects fall outside the scope of the current project:

- Ceramic- and metal-matrix composites are not considered here, but numerous studies have established possibilities of improvement on both types of composites [4]-[6].
- The study of electrical and thermal properties of carbon nanotubes or composites containing carbon nanotubes.
- A thorough study of CNTs used in multifunctional applications. As mentioned previously, answering fundamental questions about the mechanical properties of these nano- and hybrid composites is considered to be most important.

This work will first present a thorough review of previous analytical and experimental results in the processing and mechanical characterization of pure CNTs and composite materials based on CNTs: CNT/polymer nanocomposites and hybrid composites (CNT/polymer matrix/advanced fiber composite materials). Second, the work will present results obtained in this research for the fabrication and mechanical characterization of nanocomposites using different commercially available polymer matrices. Third, preliminary results regarding the feasibility of the manufacturing of two promising hybrid architectures will be presented. Finally, conclusions will be extracted together with recommendations for future work.

Chapter 2. Literature Review

In this chapter, research into processing, characterization and modeling of carbon nanotubes (CNTs) and their composites (polymer matrix focus) is reviewed. The chapter is divided into two major parts that address two related issues: First, a review of the research focused on CNTs themselves, their fabrication and characterization, to fully understand their possible applications; second, a comprehensive review of the literature related to CNT-based polymer composites, the effectiveness of the reinforcement, and known issues. As mentioned in Chapter 1, the focus will be on polymer-matrix composites, the characterization of their mechanical properties and their application as structural materials.

2.1 Carbon Nanotubes: Description, Processing and Characterization

CNTs have a combination of outstanding mechanical, electrical, and thermal properties that make them eligible for numerous applications. Being interested in structural applications for CNT composites, a better understanding of their molecular structure, the manufacturing processes that allow their fabrication (growth), and the effect that both structure and process have on the CNT's mechanical properties are

fundamental. Electrical and thermal properties of the nanotubes are also interesting for other applications and have been the focus of numerous studies. However, as the focus of this research is the structural applications of carbon nanotubes, these studies are not included in the present review.

2.1.1 CNT Structure

Graphite is a 2-D sheet of carbon atoms arranged in a crystalline hexagonal structure held together by strong covalent bonds. The sheets are layered and very weakly held together by van der Waals forces. Carbon nanotubes are usually described as a sheet of graphite rolled into a perfect tube. As in the case of graphite, each carbon atom has 2 single (C-C) and one double (C=C) covalent bonds. Nanotubes, or CNTs, can usually be divided into two groups: single-walled and multi-walled nanotubes (SWCNT and MWCNT, respectively). This is in contrast to nanofibers, nanofilaments, and nanorods, which are not rolled structures of carbon, but more weakly arranged. SWCNTs can be thought of as rolling a single layer of graphite, whereas MWCNT consist of several concentric SWCNTs, believed to be held together primarily by Van der Waals forces (second order forces, relatively weak compared to carbon-carbon bonds). The structure of a carbon nanotube is described by its chirality. This property defines how the sheets of graphite are "rolled" into a tube, based on the geometry of the carbon bonds around the circumference. The two limit values of the chiral angle are 0 degrees (the so-called zig-zag structure) and 30 degrees (armchair structure). The intermediate cases are usually called chiral nanotubes [2]. The structures of the two limit values mentioned previously,

zig-zag and armchair, are shown in Figure 2.1. The influence of chirality on the mechanical properties of CNTs is discussed in section 2.1.3.

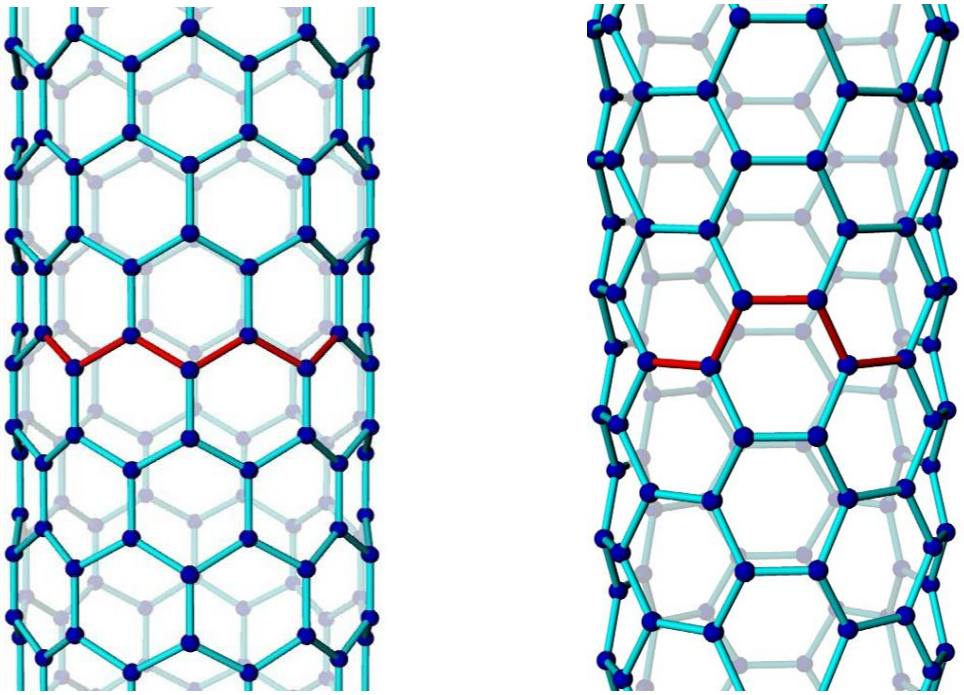

(a) Zig-zag SWCNT **(b) Arm-chair SWCNT**

Figure 2.1: Extremes of CNT atomic structure (i.e., chirality) of (a) zig-zag and (b) armchair single-walled CNTs. Spheres represent Carbon atoms, whereas the lines connecting the spheres represent carbon-carbon bonds.

2.1.2 Processing

Carbon nanotubes are synthesized using a wide variety of different techniques, such as arc-discharge [7]-[9], laser ablation [10]-[11], gas-phase catalytic growth from carbon monoxide [12]-[13], and chemical vapor deposition (CVD) [14]-[18]. The first two methods (arc-discharge and laser ablation) present important limitations to the large-scale production needed to successfully introduce these materials in structural applications: First, both methods have a finite carbon source which limits the volume of CNTs that can be produced. The gas-phase methods (catalytic growth from CO and

CVD) replace continuously the carbon source (gas), allowing continuous processing of CNTs. The costs associated with the production of large quantities of CNTs using arc-charge or laser ablation are viewed as high compared to the gas-phase techniques. Second, both methods produce a higher number of by-products or impurities than the CVD processes. The purification process needed to obtain carbon nanotubes amenable to be used in structural applications further increases the cost. Third, the temperatures needed for both processes, arc-discharge and laser ablation, are above 3000 ºC. The cost of the equipment and energy necessary to complete the processes is high when compared to the gas-phase methods, which require lower temperatures (below 1000 ºC). Finally, these processes tend to form ropes or bundles of nanotubes instead of detached CNTs. The effective mechanical properties of these ropes decrease considerably when compared to straight single nanotubes, as stated by Yu *et al.* [44]. Gas-phase methods, on the contrary, allow the synthesis of large quantities of detached carbon nanotubes that can be used immediately after the synthesis process.

The two gas-phase methods mentioned in the previous paragraph, catalytic growth and chemical vapor deposition, permit different approaches to the synthesis of CNTs. Gas-phase catalytic growth using CO as the carbon source is a refined process that enables the production of large quantities of very long and pure SWCNTs randomly oriented [12]. The technology has been commercialized for large-scale production [2]. Chemical vapor deposition (CVD) is also a large-scale production process with a relatively low price of production when compared to other processes. The CVD process requires the dissociation of a high-carbon-content hydrocarbon gas in the presence of a catalyst (a transition metal) at elevated temperatures (from 500 ºC to 900 ºC). It is

important to note that, as mentioned previously, the temperatures required for this process are well below the temperatures needed for arc-discharge or laser ablation (around 3000 ºC). After dissociation, carbon atoms are dissolved into the nanostructural catalyst, reaching a saturation point. The precipitation of carbon from the saturated catalyst nanoparticles results in the formation of carbon nanotubes [86]. Depending on the method used to obtain the high amount of energy required to dissociate the hydrocarbon gas precursor, the CVD processes can be divided into Thermal CVD or Plasma-Enhanced CVD. Thermal CVD uses heat to enable dissociation. PECVD uses heat as well as high energy electrons in plasma to dissociate the feed gas, and therefore requires significantly lower temperatures (~550 ºC) [87]. For both methods it is possible to localize the growth of CNT's through controlled catalyst deposition. Plasma-enhanced chemical vapor deposition (PECVD) is a variation of the CVD process that allows the generation of large arrays of well-aligned single- and multi-walled CNTs [14]. This arrangement likely exploits CNTs mechanical properties to the maximum. Thermal Chemical Vapor Deposition requires a higher temperature in the process, but allows interesting variations with respect to PECVD. Using the right parameters it is possible to obtain dense forests or patterns of well-aligned thin carbon nanotubes (~10 nm in diameter). The main advantage of this process when compared to PECVD is that the thermal CVD allows faster growth rates (up to 2.5 μm/s, or 150 μm/min, compared to 2 μm/min for the PECVD process) and lengths of the CNTs that can go from several microns to several mm [84]. Zhu *et al.* recently obtained 4-cm-long single-walled CNTs using thermal CVD and reported their ability to grow even longer nanotubes [85]. The length limitations of the PECVD process are due to the rapid consumption of the catalyst. This problem can be

overcome by re-catalyzing the tips of the CNTs to create longer CNTs, but the re-catalyzing process creates defects that reduce the CNT's mechanical properties.

The benefits of chemical vapor deposition over the other methods mentioned previously (arc-discharge, laser ablation and catalytic growth) can be summarized as:

- Ability for the growth of different types of nanostructures (tubes or wires) [25].
- Large area growth.
- Direct growth onto substrate (compared to the other methods that produce detached CNTs).
- Good alignment of the nanotubes produced.
- Control over variables like tube length (via time of exposure) and diameter (via control of the catalyst) [15].

Due to these advantages over the other processes, plasma-enhanced chemical vapor deposition (PECVD) and thermal chemical vapor deposition are the processes selected by many groups working on CNTs. Thermal CVD in this work.

2.1.3 Mechanical Properties Characterization

A good understanding of the properties of carbon nanotubes is critical in order to better understand the real applications that they can have. The characterization of carbon nanotubes, because of their reduced size, imposes considerable difficulties. The development of atomic force microscopy (AFM), Raman spectroscopy, transmission electronic microscopy (TEM), and X-ray scattering and tomography have allowed the characterization of carbon nanotubes and nanocomposites from the molecular level.

However, the results obtained from different studies using different techniques differ considerably. The focus of different studies has been on Young's modulus and strength along the CNT axis. Little is known about the transverse properties of the CNTs, in part due to the complexity of the tests needed.

Chirality and its effects on CNTs properties, for example, have been the subject of controversy. Chirality, as mentioned before, defines how the sheets of graphite are "rolled" into a tube. All studies related to chirality agree that it has strong impact on the electronic properties of CNTs. Nanotubes can be either metallic or semiconductor, depending on their chirality. Armchair CNTs are metallic, whereas zig-zag CNTs are semiconductors. The influence of chirality on the mechanical properties of CNTs, however, is not so clear. Yakobson [29] used atomistic theories (molecular dynamics, MD) to model the different CNT structures (armchair, chiral, and zig-zag). According to those numerical results, the effect of chirality on the elastic stiffness is insignificant (below 1%). Lu [22] developed an empirical lattice dynamics model (used previously to model graphite layers by R. Al-Jishi and G. Dresselhaus [23]), that predicted that chirality does not affect the mechanical properties of CNTs. Opposed to this theory, other studies [58] hold that the exact magnitude of the mechanical properties depend on chirality, as well as the type of nanotube (single- or multi-walled), and its dimensions (diameter and length). It is interesting to mention that Yakobson [29] also used the model to simulate high strains applied to the carbon nanotubes. According to that analysis, CNTs allow, under tension, a Stone-Wales transformation (a reversible diatomic interchange that changes the structure from four hexagons to two heptagons and two pentagons in pairs). This transformation, shown in Figure 2.2, may explain the high

resilience and strain-to-failure without plasticity (5%) observed for carbon nanotubes [43], [88].

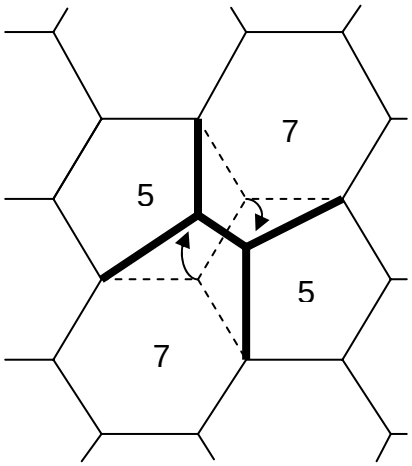

Figure 2.2: Stone-Wales transformation.

The measured mechanical properties of single- and multi-walled carbon nanotubes vary significantly from one study to the other, due somewhat to the indirect nature of the measurements. Another important factor that contributes to the scattered results is the difficulties in calculating the effective area of the nanotubes. Typically, CNTs are assumed to be cylindrical tubes with an inner and outer diameter. In the case of single-walled CNTs, this is a straight forward approximation. Multi-walled CNTs are sometimes treated as a solid cylinder or as a solid tube in the calculations (i.e., a cylinder having wall thickness equal to the difference between the outer and inner radii of the tubes) [107], and other times as a set of non-interacting concentric tubes [28].

Govindjee and Sackman [89] have discussed the validity of continuum mechanics in the estimation of nanotubes properties: First, they derived an expression to correct the error produced by homogenizing the cross section of a MWCNT, which in reality consists of discrete, separated layers of finite thickness. Second, they also pointed out that

"as the specimen size diminishes, the lattice spacing becomes important, and the discrete structure of the material can no longer be homogenized into a continuum." According to this work, calculations for the area that transform the MWCNT into a solid material can only be considered as approximations. As mentioned previously, other studies [28] model MWCNTs as concentric tubes with a particular thickness and regular spacing between the walls. Even if CNT walls are not continuum, it is possible to approximate them to a continuum wall with an effective mechanical thickness. Different studies [29]-[30] have established, by comparing atomistic level simulations and shell theory, that the wall thickness ranges between 0.066 and 0.075 nm. The inter-wall spacing is maintained by weak van der Waals forces and has been measured to be between 0.34 and 0.39 nm [31]-[33]. The inter-wall spacing is considered to be constant during tensile and bending tests [34]-[35]. TEM measurements [36] seem to confirm the lack of interaction between the different walls of a MWCNT under bending.

Different experimental methods have been used to determine the Young's modulus and the strength properties of the carbon nanotubes: measurement of the CNTs' intrinsic thermal vibration, tension, compression, and bending tests using AFM tips, and compression tests using a nanoindenter are the most important methods used prior to this work. More recently Demczyk *et al.* were able to develop a tensile testing stage device using microfabrication techniques that allowed the application of tensile strain to individual CNTs while viewed in a TEM [88]. The highest values were obtained by Treacy *et al.* [24]. In that work, TEM was used to determine that the elastic modulus of MWCNTs was 1.8 TPa. However, this value was not obtained from a direct measurement, but from the study of the intrinsic thermal vibration of the nanotubes at

different temperatures. The MWCNTs were approximated as solid tubes with an inner and an outer diameter for the calculations. No results on strength were reported. Wong *et al.* [25] used an atomic-force microscope (AFM) to directly measure the stiffness and strength of a single MWCNT through a bending test. They pinned one end of the CNT and bent the other end by means of the AFM tip. The value for the elastic modulus was reported as 1.26 TPa, whereas the tensile strength value was 28.5 GPa. As in the previously mentioned paper by Treacy *et al.*, a tube with an inner and an outer diameter was used as a representation of the MWCNT structure. Yu *et al.* [27] attached both ends of multi-walled CNTs to two opposing AFM tips and applied a tensile test. The failure mechanisms for multi-walled CNTs were micrographed for further analysis. According to the experimental results, MWCNTs failure is a two-step process: First the outer tube fails; second, the inner tubes are pulled out. This is known as "sword-sheath" or telescopic failure. Yu obtained Young's moduli for the outer layer of the MWCNT that varied from 270 to 950 GPa for a MWCNT, and the tensile strength ranged from 13 to 52 GPa. Demczyk *et al.* used, as mentioned previously, a microfabricated device to obtain direct measures of MWCNT's mechanical properties. According to their measurements, Young's modulus is 0.91 TPa, the tensile strength is around 150 GPa and the strain-to-failure is 5%. In this work the area used to calculate the stresses was determined approximating the MWCNTs to a solid tube with an inner and an outer diameter. Boyce *et al.* [28] used a nanoindenter to apply a bending test to vertically aligned CNTs (VACNTs). The effective stiffness of the CNT was directly measured and the effective bending and axial moduli (E^b and E^a), and also the wall axial moduli (E^w, the axial modulus for a nanotube wall) were derived from beam theory. For the calculations, the

MWCNTs were approximated as non-interacting concentric tubes with a mechanical thickness of 0.075 nm. The effective bending modulus (values comprised between 0.9 and 1.24 TPa) was obtained by dividing the measured stiffness by the effective moment of inertia of the nanotube ($\pi D_0/64$, where D_0 is the outer diameter of the nanotube). The effective axial modulus (0.9 to 1.23 TPa) was obtained by multiplying the wall axial modulus (E^w = 4.14 to 5.61 TPa) by the sum of the areas of the walls of the MWCNT and dividing the result for the area covered by a solid cylinder with the diameter of the external tube (πD_0^2).

Although the analytical and experimental results for modulus and strength of the CNTs are scattered (particularly early works), commonly reported values of key mechanical properties for single- and multi-walled carbon nanotubes are summarized in Table 2.1**.** CNT modulus and strength is similarly summarized in the recent Thostenson review [3].

The mechanical properties of SWCNTs are compared to those of carbon and aramid fibers and also to high-tensile steel, as shown in Table 2.2. The values for the CNT were taken for a SWCNT of diameter 10 nm, using the entire area enclosed by the tube to normalize stiffness/strength. It is important to note the extremely high values of the CNTs' specific strength and specific stiffness.

Table 2.1: Commonly referenced mechanical properties of CNTs (Øint and Øext correspond to inner and outer diameter respectively).

Method of measurement	Elastic modulus (TPa)	Tensile strength (GPa)	Type of CNT
Experimental results			
TEM–Thermal vibration of beam [24]	1.8		MWCNT (solid tube with $Ø_{int}$ and $Ø_{ext}$)
AFM – 1 end clamped, bending test [25]	1.28	28.5	MWCNT (solid cylinder)
AFM – 2 ends clamped, tensile test [26]	0.81		SWCNT
Dual AFM cantilevers, bending test [27]	0.27-0.95	13-52	MWCNT (solid tube with $Ø_{int}$ and $Ø_{ext}$)
TEM direct, tensile test [88]	0.91	150	MWCNT (solid tube with $Ø_{int}$ and $Ø_{ext}$)
Nanoindentation – bending [28]	0.9 – 1.23		MWCNT (concentric non-interacting tubes)
Analytical calculations			
Empirical Lattice Mechanics [37]	0.97		MWCNT (concentric non-interacting tubes)
Ab initio [38]	1.0		SWCNT
Molecular Structural Mechanics [39]	1.05		SWCNT
Pin-jointed Truss model [40]	0.68		SWCNT
Molecular Dynamics Simulation [41]		150	SWCNT
Molecular Mechanics Simulation [42]		93-112	SWCNT

Table 2.2: Comparison of mechanical properties of CNTs, carbon, and Kevlar fibers and high-tensile steel [50], [71]. The values for the CNT were taken for a SWCNT of diameter 10 nm, using the entire area enclosed by the tube to normalize stiffness/strength.

	CNT	Carbon fiber	Kevlar fiber	High-tensile steel
Tensile strength	130 GPa	3.5 GPa	3.6 GPa	1.3 GPa
Young's modulus	1000 GPa	230 GPa	128 GPa	210 GPa
Density	1300 kg/m^3	1740 kg/m^3	1440 kg/m^3	7870 kg/m^3
Specific strength	100 GNm/kg	2.00 GNm/kg	2.5 GNm/kg	0.17 GNm/kg
Specific stiffness	770 GNm/kg	132 GNm/kg	89 GNm/kg	27 GNm/kg

Figure 2.3 is a graphical comparison among the specific properties of the CNTs using the range of values in Table 2.1, and other materials commonly used in structural applications. Note order of magnitude in specific stiffness, and 1-2 orders of magnitude in specific strength of CNTs when compared to the best fibers.

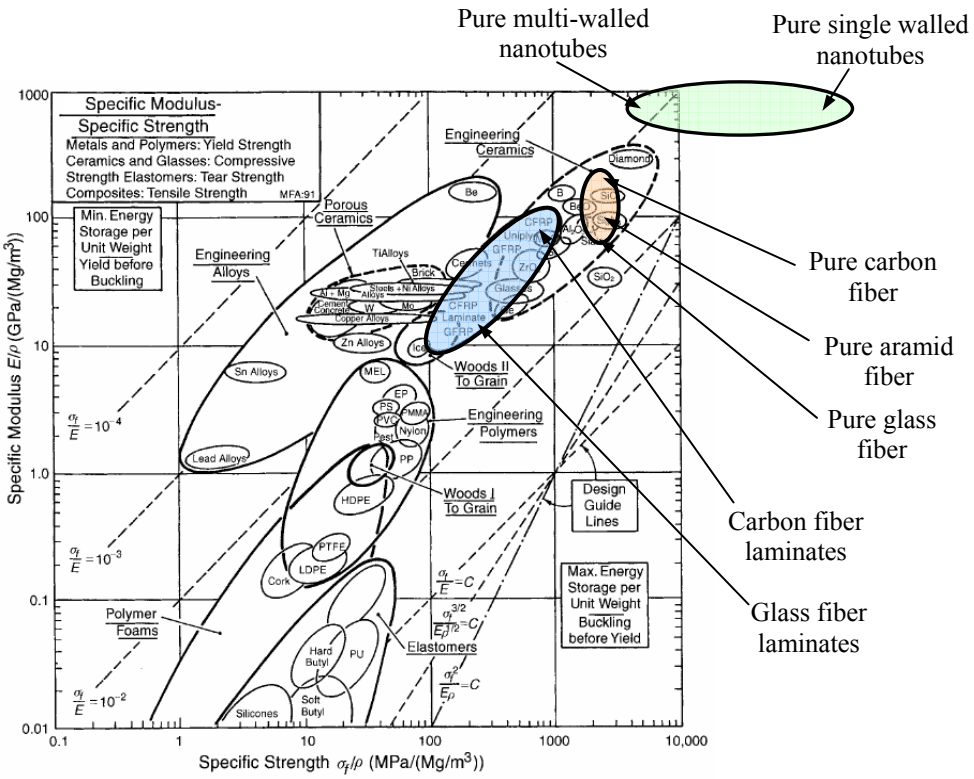

Figure 2.3: Specific strength vs. specific modulus for the most common materials compared to CNTs. Chart modified from Ashby's plots [113].

2.2 CNTs/Polymer Composites: Description, Processing and Characterization

As noted in the introduction, the exceptional mechanical and physical properties of carbon nanotubes, together with their low density, make them good candidates for fiber reinforcement in polymer composites. Though the results found to date in the literature are promising and motivating, the application of CNTs as a reinforcement has been hindered by the many difficulties associated with their processing. Fabricating CNTs into functional macroscale composites has been a major challenge. Achieving a good dispersion of the CNTs in the polymer matrix (CNTs tend to form agglomerates in the form of ropes and clusters), the alignment of these CNTs in the direction of the load, the adhesion between the nanotubes and the matrix, and the quality/quantity of CNTs embedded are the most important technical problems in the fabrication process. Related to these four is the maximum volume fraction of CNTs that the manufacturing process allows. For CNT/polymer composites, beyond certain volume fraction (usually around 3%) no further improvements in the composite mechanical properties are achieved using the fabrication methods (mixing of polymers and CNTs) reported in the literature. Good dispersion, alignment and adhesion are completely necessary in order to take advantage of the mechanical properties of the CNTs, but with higher volume fractions, dispersion and alignment deteriorate, and both voids and CNT agglomerates form, producing a reduction of properties.

Another important difficulty that must be taken into account is the measurement of the volume fraction of CNTs. Most of the studies found in the literature do not measure volume fraction, but rather calculate it from the weight fraction (easier to

measure and to control) and the densities of the CNTs and the polymer matrix before combining. However, this procedure presents two problems: First, it is not clear if the volume inside the tubes is filled with polymer or if it is void. The volume fraction changes considerably from one situation to the other. Second, the density of the CNTs is not clearly defined, because the measurement of the volume is extremely difficult. Usually it is assumed that the density of each wall is the same as the one found for graphite (2.25 g/cm^3). The density of the CNT is then calculated from the diameter of a representative tube, obtained using TEM imaging [3]. The other possible solution to calculate the volume fraction is using TEM to calculate the surface area occupied by the CNTs compared to the surface occupied by the polymer in a cross section of an aligned CNT/polymer composite. However, the most common method used to calculate the density is to assume that the MWCNT is a solid tube (annulus) with inner and outer diameters. In this case, the densities obtained are usually in the order of the density of most of the polymer matrices used in CNT/polymer composites. Due to this fact, usually the volume fraction is equivalent to the weight fraction.

The two main ways investigated to date to introduce CNTs as reinforcement for polymer composites are:

- The creation of long fibers that replace advanced macro-fibers (*e.g.*, graphite). Such substitutive fibers are made of pure CNTs (long CNTs or short spun CNTs) or by using CNT/polymer composite fibers.

- The addition of CNTs to the polymer matrix to reinforce it. These CNT/polymer composites can be divided into 2 categories: CNT reinforced polymers (here referred to as nanocomposites), usually found in the literature in the form of films,

and hybrid composites containing a polymer (or other) matrix, standard advanced fibers and CNTs reinforcing the matrix.

2.2.1 Long Fibers Containing Carbon Nanotubes

Due to the extraordinary flexibility of fibers containing CNTs (up to 30% bending strain using the process developed by Baughman *et al.* [90]), CNT/polymer fibers are seen as a possible substitute for traditional carbon fibers. Significant research has been devoted to creating a long fiber containing CNTs that takes real advantage of their outstanding mechanical properties. However, up to this point, none of the processes developed has been able to improve the reinforcement properties of graphite fibers. As mentioned previously, researches have been trying to develop long fibers using two different approaches: Polymer fibers reinforced with short CNTs, and pure-CNT long fibers, using either short spun CNTs or long CNTs.

Andrews *et al.* [46] dispersed SWCNTs in isotropic petroleum pitch and spun fibers with good mechanical properties. The fibers obtained were extremely flexible and strong compared to plain pitch fibers. However, their elastic modulus (around 15 GPa) was still far from carbon fibers. Poulin and co-workers [47] developed a method to improve the mechanical properties of the fibers. After the spinning of the fibers, the fibers were rewetted, and a tensile load was applied to stretch the fibers. By stretching the fibers they obtained fibers with Young's modulus close to 40 GPa and strengths close to 230 MPa (compared to 15 GPa and 125 MPa for the non-stretched fibers). These fibers are still not competitive with graphite fibers. CNTs have also been applied to obtain polymer-based fibers with diameters in the 100-nanometer range by electrospinning [48].

Preliminary results with SWCNT and PAN suggest that 1 wt% addition of nanotubes doubles the original tensile strength and modulus of the PAN fiber. Baughman *et al.* [90] were able to create long CNT/polymer fibers containing up to 60% of CNTs by weight using a modified coagulation method. The CNT/polyvinyl alcohol fibers obtained had an elastic modulus of 80 GPa and a tensile strength of 1.8 GPa, much closer to the mechanical properties of the traditional graphite fibers. However, these fibers have an outstanding energy-to-break (570 J/g, compared to 33 J/g for Kevlar fibers and 12 J/g for graphite fibers), which qualify them as a good substitute for impact applications. Due to their high strain-to-failure (30%), the fibers can easily be woven and sewed. Kumar *et al.* [96] reinforced poly-p-phenylenebenzobisoxazole (PBO) fibers using 10% in weight of SWCNT increasing the tensile strength about 50%. The resulting fiber had a tensile strength of 4.2 GPa and a Young's modulus of 167 GPa, both comparable to the mechanical properties of graphite fibers.

The other approach to find a substitute for graphite fibers is the creation of pure CNT long fibers. Dzenis and Larsen [91], [92] created extremely thin (~3 nm) continuous nanofibers (with no limitation in length as reported by the authors) using an electrospinning technique. Although these nanofibers are not based on carbon nanotubes, they could become a good reinforcement if some important issues regarding the reduction on the mechanical properties due to impurities are solved. Ajayan and coworkers [93] synthesized long strands (no limitation in length) of short SWCNTs held together using the catalytic pyrolysis of n-hexane with an enhanced vertical floating technique. The arrays of short nanotubes were subjected to a tensile test and their Young's modulus was determined to be around 150 GPa, approximately the same value measured for SWCNT

bundles [52]. Baughman *et al.* [94] adapted the technique traditionally used to create wool and cotton yarns to create pure CNT yarns. From a dense forest of vertically aligned CNTs created using the CVD process (described in section 2.1.2), CNT yarns were fabricated by spinning the CNTs. The resulting yarns had poor tensile strength (450 MPa) when compared to graphite fibers, but a higher strain-to-failure (13% vs. 1% for the graphite fibers) and also a good resistance to fatigue cycles: The failure strength was unaffected by loading-unloading cycles over a stress range of 50% of the failure stress. In a posterior article [95] Baughman showed that it was possible to create strong, transparent CNT sheets (so-called bucky paper) using the same technique used to create the yarns. Windle *et al.* [97] have reported the growth of a continuous MWCNT fiber (no limitation in length) grown by spinning inside the CVD furnace, which qualifies this technique for large-scale production. Unfortunately, no mechanical properties of the CNT fiber were reported.

The best option to take advantage of the CNTs' mechanical properties as reinforcement is to develop a method to grow long continuous CNTs. Zhu *et al.* [85] modified the CVD process conditions to obtain a 4-cm-long virtually defect-free SWCNT. No mechanical properties were reported. The process suggests the possibility of growing SWCNTs continuously without any apparent length limitation. Regardless, CNT-based fibers will not replace graphite fibers until a robust continuous process is developed to fabricate long CNTs. Until then, using CNTs as a reinforcement for the matrix in traditional composite materials, or to create hybrid composite architectures (containing CNTs, fibers and a polymer matrix), which are the two focuses of this research, seems more promising.

2.2.2 CNT/Polymer Composites

As said in the previous section, reinforcement of a polymer matrix using CNTs has proved to be the most effective and immediate way to take advantage of the mechanical properties of the CNTs. CNTs have been applied in numerous studies to reinforce polymer films. The advantages of using CNTs to reinforce polymer films include not only the improvement of the polymer's mechanical properties, but also to increase its thermal stability and its gas barrier properties compared to pure polymer films and to carbon- or fiber-reinforced composites [49]. Several different techniques have been developed to embed CNTs into a polymer film, but the most effective ones are solution-evaporation with sonication and calendering. The first method [65] uses the sonication of nanotubes in a solvent (usually chloroform) and a later addition of the resin material to the solution. Once the dispersion is improved by sonication, the solution is introduced into a mold and cured at room temperature. The second method [73] relies on calendering. In this method the nanotubes are manually mixed into the resin and dispersed using a two- or three-roll calender. The film generated is subsequently cured at room temperature and post-cured at around 60ºC, depending on the polymer matrix used in the experiment.

After the fabrication of the nanocomposites in the form of films, characterization techniques are applied to unravel their macroscopic mechanical performance. According to the results obtained, there are three main factors during the embedding phase that influence the mechanical properties of the final composite: (1) a good dispersion of the nanotubes, (2) a good alignment of the tubes, and (3) a good adhesion between polymer and CNTs. This is no different than for traditional composites.

The first important factor that influences the final mechanical properties of the composite is the dispersion of the CNTs within the polymer matrix. Ensuring a good dispersion of these nanotubes into the polymeric matrix is vital. Because of their reduced size, carbon nanotubes tend to agglomerate when dispersed in a polymeric resin. Aggregates of nanotubes reduce the aspect ratio (length/diameter) of the reinforcement, reducing the final performance of the composite. SWCNT tend to agglomerate into ropes and these ropes tend to form aggregates. CNTs in these aggregates are not in contact with the polymer. The interactions between CNTs are established by very weak bonds that fail at low shear stresses. They can be considered as holes within the polymer, acting as stress concentrators and have been shown to reduce the composite shear strength when compared with the pure polymer [72]. Chemical functionalization can help reduce the formation of aggregates, providing improved dispersion, and therefore to increase the performance of the CNTs as reinforcement [26].

The second factor that maximizes the nanocomposite performance is good alignment of the nanotubes inside the resin matrix. Theoretical and experimental results concur to demonstrate its importance. Odegard *et al.* [66] developed a molecular dynamics model of a CNT/polyimide composite and obtained theoretical longitudinal Young's moduli for CNT-composites that varied from 5 GPa with CNTs randomly orientated to a maximum value of 16 GPa when all CNTs where aligned. Zhou *et al.* [65] demonstrated that the alignment of carbon nanotubes inside a polymer matrix could be effectively improved by mechanical stretching. Thostenson and Chou [59] used a micro-scale twin-screw extruder to create a composite film with dispersed CVD-grown MWCNT in a polystyrene matrix. By using the extruder they not only obtained a

relatively good dispersion but also a good alignment of the nanotubes, compared to the methods previously mentioned. This method also allowed a higher volume fraction (~5% in weight). However, the dispersion and alignment were still not well controlled, and the volume fractions are limited to a maximum of 5% in weight. Using a hot press, they also cast a film with well-dispersed, randomly-oriented CNTs to compare their properties. The increase of the storage modulus in the aligned film was about five times greater than the improvement achieved by the randomly oriented configuration.

Finally, the last and most important factor that must be guaranteed is a good nanotube/matrix adhesion. There are three commonly-identified different mechanisms of load transfer from matrix to fiber: micromechanical interlocking, chemical bonding, and weak Van der Waals bonding [52]. Interfacial adhesion is critical to take full advantage of the exceptional stiffness, strength and resilience of carbon nanotubes [2]. With poor adhesion, the load transfer across the CNT-matrix interface is less effective, reducing the improvements in the mechanical properties of the nanocomposite [70]. Different theoretical and experimental studies give widely varying results on this fundamental point of the characterization.

Wei, Cho and Srivastava [53] used molecular dynamics (MD) simulations to show that chemical bonding between polyethylene and CNTs is energetically favorable. According to their study the adhesion at the interface is due to C-C first-order bonding (the double carbon-carbon bond in the CNT wall is broken, leaving 3 single bonds for this type of polymer-CNT bonding), more effective for load transfers than the previously predicted van der Waals forces. That work also showed that multi-site bonding is

possible, favoring the matrix-CNT load transfer and improving the composite shear strain.

Ajayan [52] used Raman spectroscopy on 5 wt% MWCNT/epoxy composite samples under tension and compression. The results obtained in both tests showed that the adhesion between the outer CNT and the polymer was good. However, there is an important difference between the two tests: Multi-walled carbon nanotubes reinforcement is much more effective under compression. The hypothesis formulated by Ajayan is that under tension, the outer layer of the CNT is loaded, but this load is not transferred to the inner layers because MWCNTs have weak bonds between layers, as described in section 2.1.2. Under compression, instead, all the layers are effectively loaded and contribute to the reinforcement of the polymer.

Wagner *et al.* [54]-[56], using transmission electron microscopy (TEM), observed evidence of good polymer (polyurethane)-nanotube wetting and significant nanotube-polymer interfacial adhesion, and thus of polymer-CNT interfacial affinity. They also noticed the appearance of "telescopic" ruptures in multi-walled carbon nanotubes embedded in polymer matrix when subjected to stress. Based on these observations, they inferred that the CNT/polymer interface shear strength (about 150 MPa for multiwalled CNT) is higher than either the matrix or the CNT-CNT "telescopic" shear strengths (~0.30 MPa [35]). Further studies [136] have estimated the nanotube-matrix interface shear strength to be near 500 MPa, at least one order of magnitude larger than in conventional fiber-based composites. The presence of multiple concentric graphene planes (MWCNTs) is postulated to strongly enhance the reactivity of carbon nanotubes towards covalent bonds containing polymeric chains, upon UV curing of the specimens.

These covalent bonds between the polymer and the CNT carbons could be responsible, according to [55] for the observed interface strength. In a more recent study [57], the interfacial fracture energy was measured using pullout testing. A multi-walled carbon nanotube was attached to an atomic-force microscope (AFM) tip and then introduced very slowly into a polyethylene-butene film heated so that the polymer was fluid. The process was made at a speed that allowed the introduction of the nanotube without bending. After the introduction of the nanotube, the whole system was allowed to air-cool until room temperature. The nanotube tip was retracted and the energy necessary to extract the nanotube measured. The energy obtained for the nanotube/polymer interface (with a maximum of 70 J/m^2) was comparable to that of fiber pullout in other engineering composite systems. "Traditional" composite fibers are chemically modified to improve the bonding between matrix and reinforcement. The fact that the CNT/polymer results are comparable with those of strongly-bonded composite systems supports the idea that the interaction between CNTs and polymer matrix can be a sum of van der Waals bonds AND first order chemical bonds.

Numerous studies have focused on the improvement of the adhesion between CNTs and polymer. As mentioned earlier regarding dispersion, chemical functionalization (formation of covalent bonds) reduces the formation of aggregates and minimizes the reduction in the composite's effective shear strength that the agglomerates produce. Another important advantage of using functionalization is that it enhances the interfacial adhesion, as shown analytically by Frankland *et al.* [67]. Comparing CNT/epoxy with non-functionalized and amino-functionalized composites, there is a one to two order of magnitude increase in the interfacial shear strength.

The trade-off for composites with covalent bonds is that these bonds reduce significantly the mechanical properties of the nanotube itself, according to [68]-[69]. Therefore, it is better to increase the load transfer between the nanotube and polymer by using improved non-covalent bonding methods. PmPV molecules [poly(m-phenylenevinylene)] substituted with octyloxy chains] naturally wrap around CNTs in a helical pattern [69]. This non-covalent interaction improves load transfer at the interface without compromising the outstanding mechanical properties of the nanotubes. PmPV molecules entangle themselves with structural polymer molecules (such as polyimides), too. Therefore, the PmPV can be used as an interface between CNT and structural polymer to increase the load transfer between the two.

Improved adhesion (by any of the methods described above) can contribute to enhance an extremely important mechanism of fiber reinforcement of composites: the so-called crack-bridging mechanism [114]. TEM observations of crack nucleation and propagation in MWCNT/polystyrene (PS) films allowed Dickey *et al.* [58] to image this phenomenon. When the crack initiates, CNTs aligned perpendicular to the crack direction bridge the two crack faces. The bridging mechanism dissipates energy by pullout until a critical dimension of the crack is achieved. At that point, carbon nanotubes begin to break or pull out of one of the faces. The same crack-bridging phenomenon was observed in films by Gojny [73] and in polymer fibers by Gogotsi [48]. In the case of CNT/polymer fibers, CNTs reinforce the polymer fiber by hindering crazing extension, minimizing stress concentration, and also bridging the cracks, dissipating energy by pullout. The four possible fracture mechanisms for the CNTs observed experimentally are: pull-out due to CNT/matrix interfacial debonding (poor adhesion), complete breakage of the CNT

(strong adhesion combined with high local strain rate), telescopic pull-out (the outer layer breaks due to strong interfacial adhesion, and the inner layers are pulled-out), and effective bridging combined with partial interface debonding (partial failure of the non-debonded regions).

Composite pellets have recently been added to the list of possible large-scale processes to manufacture CNT-embedded composites. S. G. Kim *et al.* [74] have developed a process for fabricating nanopellets, consisting of aligned CNTs embedded within a block of polymer. In the process, called transplantation and also nanopelleting, the pellets are fabricated using standard microelectronics processes and tools. First, silicon trenches are etched and a catalyst is positioned in their centers. Second, CNTs are grown using the plasma-enhanced chemical vapor deposition (PE-CVD) method described in section 2.1.2. This process results in a CNT bundle of vertically aligned nanotubes. Third, the trenches are filled with an epoxy resin. Afterwards, the substrate is planarized to create isolated pellets with uniform-length CNTs. Finally, the pellets are released by XeF_2 etching. The pellets can be harvested, and theoretically transplanted in large scale. The transplantation process (the final subprocess) starts with the manual positioning of the pellets on a new substrate. Then, the assembly is heated to assure a good adhesion of the pellets. Lastly, the filler (epoxy) can be removed by exposing the pellets to oxygen plasma (CNTs and the substrate are not affected by this process) if desired.

This process provides control over individual CNT length, alignment and position during assembly, as opposed to the liquid dispersion methods described in the fabrication of composite fibers and films. For example, the alignment achieved by mechanical

stretching of films was on the order of 60% of the nanotubes with an angle of ±23º [65]. Because of the nanopelleting capability to control the distribution of carbon nanotubes and to handle their assembly in a large-scale matrix, this process appears to be a promising technique to allow the introduction of CNTs into structural applications.

In the author's opinion, the most promising method to introduce CNT-reinforced composites in real large-scale applications is thermal CVD, described in section 2.1.2. There are several important facts that support this statement:

- Using this process it is possible to control the dimensions of the CNTs (diameter, length and volume fraction). The growth of the CNTs is stable, generating a dense forest of CNT of the same height [98]. The control over the height of the CNTs may eliminate the need for a planarazation process to create an even film, reducing its overall cost.
- It is possible to easily shape the forest of CNTs by patterning the deposition of the catalyst [110], [112]. The process allows the creation of pellets similar to the ones created by Kim *et al.* [117].
- The CNTs are well-aligned and perpendicular to the surface of the substrate. The substrate does not have to be flat as in other methods, allowing the growth of CNTs on fibers [100], for example. This is particularly interesting for the creation of hybrid composites, as described in section 2.2.3.
- The wetting of the polymer matrix into the forest of CNTs is reported to be effective enough to create nanoporous membrane structures [99] where molecular

transport through the CNT cores (indicating a perfect wetting of the outer layers of the CNTs) was studied and observed.

- The process works at atmospheric pressure [109], reducing the costs of fabrication.
- The fast growth of the CNTs (2.5 μm/s or 150 μm/min) achieved by some studies [110] using this method allows the development of a continuous fabrication process.

Due to the importance of the thermal CVD process in the near future of CNT-based composite materials, this thesis will focus on the characterization of CNT/polymer composites created using this technique. The thermal CVD process developed by Slocum *et al.* [109]-[111] was chosen to create nanocomposites for mechanical tests. This process has the highest reported growth rate of CNTs, is highly reliable, and should be scalable to continuous manufacturing processes [115].

As noted previously, the mechanical characterization of the aligned CNT/polymer composites created using Slocum *et al.*'s thermal CVD process will be one of the contributions of this research. Among the different methods present in the literature to characterize CNTs (macromechanical tests of composite films or fibers, atomic-force microscope using one or two tips, etc), uniaxial compression testing using a nanoindenter will give a direct measurement of the CNT/polymer mechanical properties. A complete description of the uniaxial nanocomposite specimen fabrication method can be found in chapter 3 as part of the experimental procedures used to develop the present work. Such uniaxial tests have been effectively used to measure buckling instabilities in CNTs [75]

and measure elastic modulus of microscale material specimens [103]. Waters *et al.* fabricated a regularly distributed array of aligned carbon nanotubes in a patterned alumina matrix with holes using PECVD process. The samples containing arrays of pure CNTs were then subjected to uniaxial compression using a modified nanoindenter and force-displacement curves were obtained. The present work will take a similar approach using a modified nanoindenter to characterize the nanocomposites created using Slocum *et al.*'s thermal CVD.

2.2.3 Hybrid Composites

CNT/polymer composites can improve considerably the mechanical properties of the matrix and open a whole range of multifunctional applications for nanocomposites thin films. However, in terms of structural applications, these CNT/polymer composites cannot compete with traditional continuous-fiber composite materials. As mentioned in the introduction, traditional composite materials have certain limitations, such us delamination and reduced properties in the thickness direction. A new approach is necessary to create the next generation of composite materials. The combination of carbon nanotubes, polymer matrices and advanced fibers in so-called hybrid composites can provide a good starting point. This section reports the most interesting and promising efforts to create hybrid composites able to overcome the limitations traditionally associated with composite materials.

Some studies have tried to improve the properties of traditional composites by improving the interface between plies. Dzenis *et al.* [91], [92] developed a patent-pending process to create mats of electrospun carbon nanofibers. These mats can be

placed between two plies of traditional composite materials, reinforcing the weak matrix-rich region (interface). According to the patent, the process provides improved interlaminar toughness, strength, and delamination resistance without substantial reduction of in-plane properties and without substantial increase in weight. The effectiveness of this technique is limited by the lower mechanical properties of these nanofibers when compared to CNTs (an order of magnitude lower), and also by the lack of alignment of the nanofibers (nanofibers are entangled, which limits the reinforcement effect). Ajayan *et al.* [98] used aligned carbon nanotubes grown by thermal CVD and cyanocrylate epoxy to reinforce the interface between layers of PZT and silica respectively. The intermediate CNT/epoxy layer was also intended to structurally damp vibrations. The tests indicated a 200% increase in the baseline structural damping and a 30% increase in baseline stiffness due to nanotube reinforcement. No results have been reported to date about the use of well-aligned CNT patterns or forests in between two plies of continuous-fiber composite materials. This research will provide insight on the fabrication and mechanical characterization of hybrid multilayered composites containing CNTs in the plies' interface. This research will also address the viability of a continuous process to fabricate CNT-reinforced prepregs.

Numerous studies support the feasibility of growing CNTs directly on fibers. Bower *et al.* [100] were the first to report growth of CNTs directly on the surface of fibers. They used plasma-enhanced CVD to grow 10-μm long CNTs on optical fibers. Lee and co-workers [108] used a different approach: Activated carbon fibers (ACF) are used as a substrate of a modified process that allows the growth of CNTs using the carbon fiber as the carbon source. Instead of using a hydrocarbon gas, as in the CVD

process, they used microwave irradiation to grow 5- to 10-μm long, entangled CNTs. ACF has considerably poorer mechanical properties than traditional graphite fibers, which inhibits this new composite to effectively substitute traditional composites. However, these CNT-reinforced ACF have interesting multifunctional applications in the electronics field. Bai *et al.* reported CNT growth on ceramic [102] and carbon fibers [101]. Catalyst particles can be easily deposited on the surface of ceramic (alumina) fibers, which translates into well-distributed, dense forests of 4-μm long CNTs perpendicular to the surface. Carbon fibers, on the contrary, are porous, reducing the effectiveness of the catalyst deposition in their surfaces. The catalyst tends to form agglomerates and the growth of the CNTs is not satisfactory. Zhu *et al.* [104] also grew CNTs on the surface of graphite fibers with similar results.

Giorgi *et al.* [105] used electro-deposition (ELD) to better control the creation of a uniform catalyst layer on the surface of the graphite fibers. They used a hot filament CVD process (HFCVD, a variation of the plasma-enhanced CVD process) to grow the 2 to 3-μm long, entangled nanotubes. The improvement of the CNTs distribution is evident with respect to previous studies. They also measured the adhesion of the CNTs to the fiber by the immersion of the fiber bundles into ultrasonic baths in water and acetone, revealing a good anchorage via metallic clusters (the catalyst particles).

Thostenson *et al.* [106] used magnetron sputtering to effectively deposit the catalyst and thermal CVD to grow 500-nm long CNTs on a graphite fiber. This fiber was then embedded into epoxy and subjected to a single-fiber fragmentation test. The results obtained show that CNTs improves the interfacial shear strength of the composite by 15 %, and therefore improves the fiber/matrix interface. This study did not provide any

information about the mechanical properties of the graphite fiber after subjecting it to the PECVD process (possible degradation of the mechanical properties of the fiber). Apart from this study by Thostenson, there are no other results of effective hybrid multiscale composites using CNTs grown on fibers. The current work intends to fill this gap by fabricating and mechanically characterizing hybrid composites containing CNTs grown on the surfaces of alumina fibers and embedded into epoxy resins.

2.3 Summary

Good dispersion, good alignment and good adhesion of the CNT/polymer interface (without degrading the mechanical properties of the CNTs) are mandatory to benefit from the mechanical properties of CNTs as an effective reinforcement. The methods used to fabricate hybrid fibers and films containing carbon nanotubes allow improvements in the mechanical properties when compared with the raw materials. However, the dispersion and alignment obtained with these methods are minimal and certainly suboptimal, with maximum volume fractions below 5%. No high volume fraction, well-aligned CNT/polymer composites have been made or characterized.

One possible drawback for the application of carbon nanotubes as reinforcement is the interface stress transfer, considered poor in some studies. However, according to the most recent studies the adhesion between CNT and polymer matrix is on the same order of covalent bonding and similar to adhesion of advanced fiber polymers. Therefore, the stress transfer from the polymer to the carbon nanotubes is expected to allow effective reinforcement.

The method developed at MIT by Prof. Slocum and colleagues (thermal CVD at atmospheric pressure) overcome the limitations in both volume fraction and alignment encountered by other fabricating methods. This research will characterize experimentally, for the first time, the modulus of carbon nanotube/polymer composites with high volume fraction, good dispersion and excellent alignment of the CNTs. A compression test applied to the uniaxial nanocomposite cylinders by means of a nanoindenter with a flat

tip, as well as traditional nanoindentation of films, are the methods chosen to do the characterization.

Numerous hybrid CNT-composite architectures are envisioned using the thermal CVD process employed herein (described in section 3.2). Once the techniques to incorporate the aligned CNTs into the matrix are more fully developed, these methods will be applicable to the previously mentioned hybrid CNT/polymer fibers, thin films and also to traditional multilayered composite materials, as reinforcement. The present research intends to demonstrate the feasibility of CNTs as reinforcement for full-scale structural composite applications.

Chapter 3. Fabrication and Testing of Composites of CNTs and Polymers

3.1 Introduction

The most direct structural application for CNTs is as reinforcement for "traditional" advanced composite materials, and most of the work in this direction has focused on dispersing and aligning CNTs (both single- and multi-walled CNTs) in polymeric matrices to reinforce the matrix. As identified in chapter 2, the four main processing factors which influence the mechanical properties of the final composite are dispersion and alignment of the CNTs within the matrix, adhesion between the CNTs and matrix, and the CNT length. All have been formidable challenges to the realization of aligned-CNT composites.

Dispersion is important because CNTs tend to agglomerate when dispersed in a polymeric resin. These aggregates are not well adhered to the polymer and also can act as stress concentrators, reducing the final performance of the composite [72]. Alignment of the CNTs is needed to increase the effectiveness of the reinforcement; *e.g.*, a molecular dynamics model developed by Odegard *et al.* [66] showed that the Young's modulus of a

CNT/polyimide composite can be increased by a factor of 3 when the CNTs are oriented parallel to the direction of the load. The formation of aggregates reduces the effective area of contact between the nanotubes and the polymer, hence reducing the adhesion between the two materials. The two most commonly used methods to embed CNTs into a polymer matrix, sonication [65] and calendaring [73], do not prevent the formation of aggregates. Using these methods, moderate improvements in matrix mechanical properties are typically observed due to the low CNT volume fractions and generally poor dispersion and alignment. Beyond a certain volume fraction (usually around 3%) no further improvements in the composite mechanical properties are achieved using the methods previously mentioned. At higher volume fractions with these methods, dispersion and alignment deteriorate significantly. Good dispersion, alignment and adhesion are completely necessary in order to take full advantage of the mechanical properties of the CNTs.

Others have utilized chemical vapor deposition (CVD) processes to grow densely packed carpets or forests of well-aligned carbon nanotubes, which can be wet by polymer solutions [99] to create aligned-CNT composite films. This avoids most of the problems associated with mixing CNTs and polymers. One process used to impregnate the CNTs relies on dissolving the polymer using a low viscosity solvent. Although this process is perfectly valid for microfabrication, it is likely not feasible for large-scale applications, which necessitate large substrate areas and rapid processing. CNT/polymer composites which have been developed so far can improve the mechanical properties of the matrix, and thereby introduce additional multifunctionality into advanced composites.

Prior to the development of different hybrid composite architectures, wetting of CNTs by polymer resins must be assessed. In this chapter, wetting of CNT forests by several commercial polymers (including a highly-viscous epoxy) is demonstrated [117] at rates conducive to creating a fully-dispersed CNT/matrix region around the fibers in a typical composite. After the wetting of the CNT with polymer resin is demonstrated, elastic modulus of the CNT/polymer nanocomposite was obtained by means of a nanoindenter to apply a compression test to pillars made of the previously mentioned CNT/polymer nanocomposite. Elastic modulus and hardness were also investigated using standard nanoindentation testing.

3.2 Growth of Carbon Nanotubes on Silicon Wafers

CNTs were grown by John Hart, from the Department of Mechanical Engineering at MIT, in the form of dense pillars of long aligned CNTs (up to 1 mm) grown on silicon wafers to test the effective wetting of several polymeric resins with different viscosities. The shapes of the pillars varied in order to obtain information about the difficulties of wetting in areas with different densities of CNT features.

CNT pillars are patterned CNT forests grown on silicon substrates [111], like the ones shown in Figure 3.1.a. Catalyst patterns are fabricated by lift-off of a 1 μm layer of image-reversal photoresist (AZ-5214E): the photoresist is patterned by photolithography, catalyst is deposited over the entire wafer surface, and then the areas of catalyst on photoresist are removed by soaking in acetone for 5 minutes, with mild sonication. The catalyst film of 1.2/20 nm Fe/Al_2O_3 is deposited by electron beam evaporation in a single pump-down cycle using a Temescal VES-2550 with a FDC-8000 Film Deposition

Controller. The film thickness is measured during deposition using a quartz crystal monitor, and later confirmed by Rutherford backscattering spectrometry (RBS) [116]. The substrates are plain (100) 6" silicon wafers (p-type, 1-10 Ω-cm, Silicon Quest International), which have been cleaned using a standard "piranha" (3:1 H_2SO_4:H_2O_2) solution.

CNT growth is performed in a single-zone atmospheric pressure quartz tube furnace (Lindberg), having an inside diameter of 22 mm and a 30 cm long heating zone, using flows of Ar (99.999%, Airgas), C_2H_4 (99.5% Airgas), and H_2 (99.999%, BOC). The furnace temperature is ramped to the setpoint temperature in 30 minutes and held for an additional 15 minutes under 400 sccm Ar. The flows of Ar and H_2 used during growth are established typically 1 minute prior to introducing C_2H_4, then the C_2H_4/H_2/Ar mixture is maintained for the growth period. The typical growth rate of the current system is 60 μm per minute, and the growth time is chosen to give the desired CNT forest thickness. Finally, the H2 and C2H4 flows are discontinued, and 400 sccm Ar is maintained for 10 more minutes to displace the reactant gases from the tube, before being reduced to a trickle while the furnace cools to below 100 °C. The pillars show a good alignment of the CNTs, as seen in Figure 3.1.b and Figure 3.1.c.

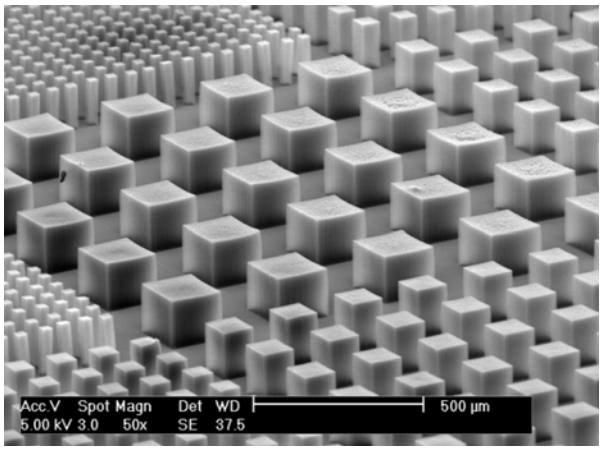

a)

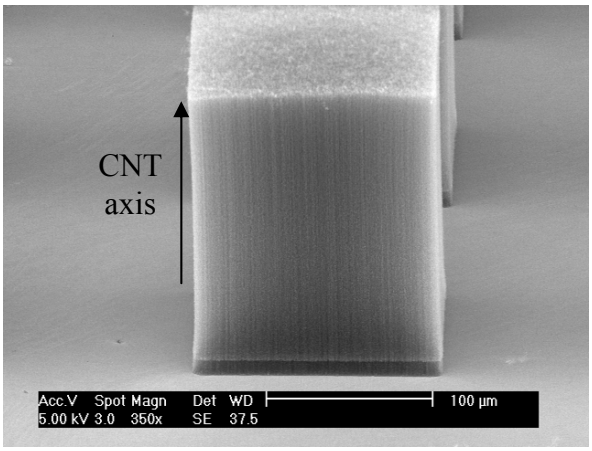

b)

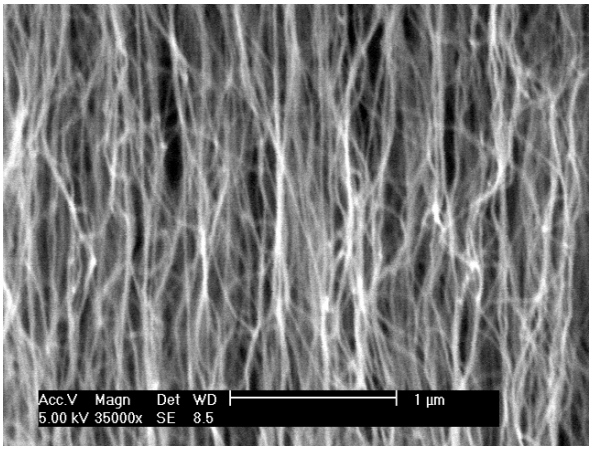

c)

Figure 3.1: SEMs of a) CNT pillars grown on patterned catalyst on silicon substrate (scale bar is 500 µm); b) Close-up of a single pillar; c) Alignment of the CNTs.

On average, the multi-walled nanotubes grown using this method have a diameter of around 10 nm (2-3 concentric CNTs) with spacing between CNTs of around 80 nm. A TEM picture of the MWCNTs is shown in Figure 3.2. Considering the MWCNTs as solid tubes with inner diameter of 5 nm and outer diameter of 10 nm and the spacing previously mentioned, the volume fraction for these nanotubes is 0.9%. Note this is not the typical composite volume fraction. The composite volume fraction of the CNT forests would be 1.2%, calculated by taking the whole cross-sectional area of the MWCNT (circular area using outer tube of the MWCNT).

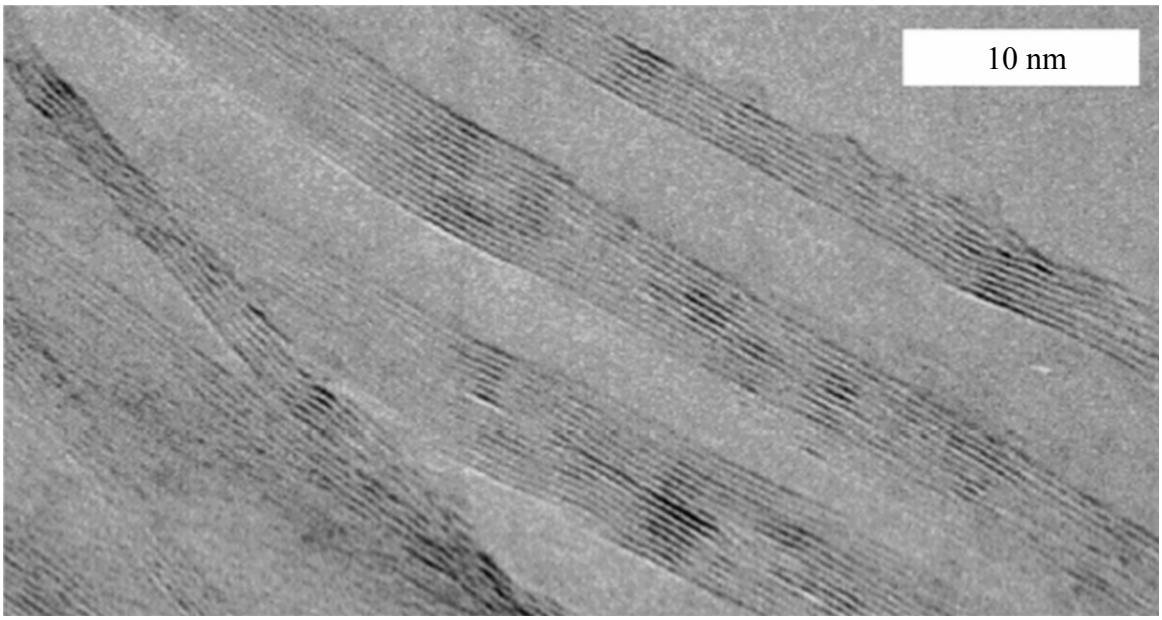

Figure 3.2: TEM image of the MWCNTs (scale bar = 10 nm).

As mentioned previously, different catalyst patterns were used to grow the CNTs. The resulting forests can be seen in the following figures: Pillars with square sections, like the ones shown in Figure 3.1.a; cylindrical pillars, as the ones shown in Figures 3.1.a) to d); and also pillars with varied cross-sections, such as triangles, squares, and hexagons (see Figure 3.4).

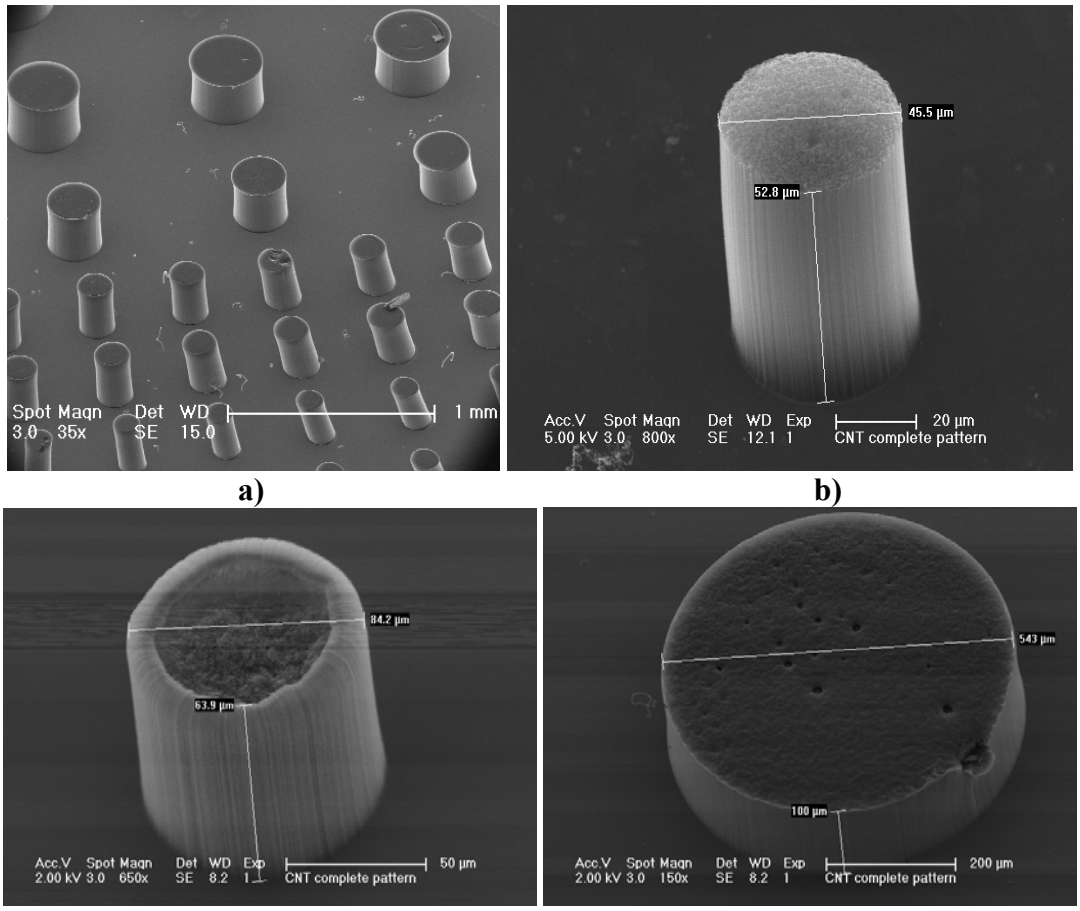

a) **b)**

c) **d)**

Figure 3.3: SEMs of a) CVD-grown CNT pillars on Si wafer surface; b), c), d) Pillars of different sizes made of pure CNTs.

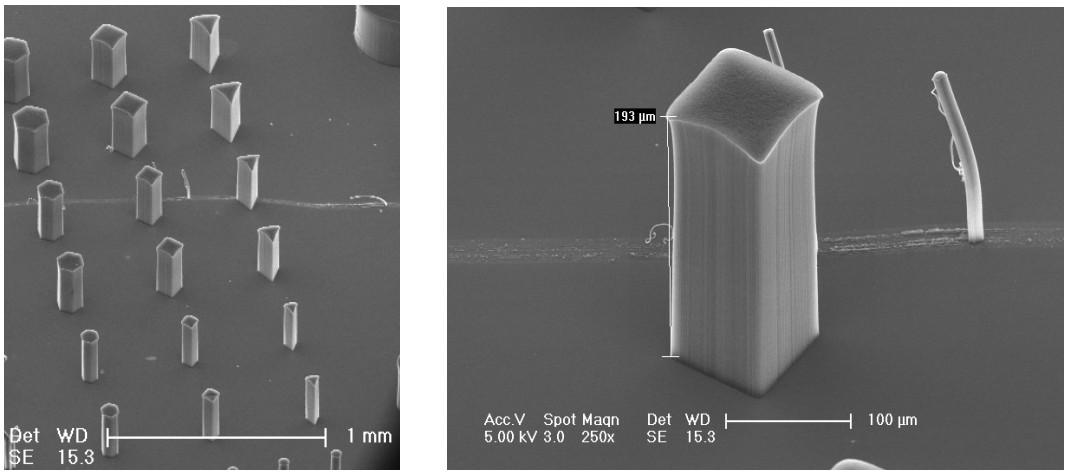

a) **b)**

Figure 3.4: SEMs of a) from left to right, hexagonal, square, and triangular CNT-pillars; b) Detail of a square pillar.

3.3 Wetting of CNTs with Different Commercial Epoxies

After showing that the thermal CVD process is a reliable and fast method to grow forests of CNTs, the next step to demonstrate the feasibility of the fabrication of hybrid composites was to assess the wetting of the CNT forests with commercial polymer resins.

3.3.1 Experimental Methods

The effectiveness of the wetting of the CNTs was explored for different sets of CNTs pillars and forests on Si wafers using three different commercially available epoxies: a high-viscosity 20-minute curing conductive epoxy (Loctite Hysol 1C [144]), a low viscosity epoxy (Buehler EpoThin), and different grades of low viscosity UV-curing epoxy (Microchem SU-8 [145]). Initial tests were performed using methods reported in the literature for the different epoxies without success. Five sets of tests provided insightful results. The high-viscosity epoxy was used for two sets of tests with pillars of different heights using the wetting method described in Figure 3.5. A variation of the dropwise method (described in Figure 3.6) using low viscosity SU-8 2005 (UV curing epoxy) was performed for the third set of successful tests. A spraying gun was used in the fourth set of tests to uniformly disperse different grades (2002 and 2005) of low viscosity SU-8 on CNT pillars. Finally, a new microfabrication method (see Figure 3.8), referred to herein as "submersion method" was developed to wet CNT pillars with low viscosity SU-8 2000.1 and 2002.

Numerous tests using the wetting methods reported in previous works (dropwise, dropwise + spincoating, gravity) were performed without success in trying to find the best combination of resins and process conditions to wet the CNTs, but are not reported

in this work. In the literature, the most common way of applying the polymer matrix to the CVD-grown CNT forest is putting a drop of a solution of the polymer on top of a forest of CNTs [99]. However, due to the hydrophobic nature of our CNTs (~10 nm diam., 80 nm spacing), this method proved to be inadequate to create well-controlled nanocomposites for high- and medium-viscosity polymers, as described briefly in section 3.3.2. The lack of good results using conventional methods required the development of new wetting processes not reported to date that could be of use for future works in the field (5th set of successful tests). A summary of the successful wetting tests performed in this research is presented in Table 3.1. An FEI/Philips XL30 FEG SEM was used to capture images of the wetting results obtained from the five sets of tests.

Table 3.1: Test matrix of successful CNT wetting tests performed.

Set of tests	Process	Epoxy	Feature type	Number of specimens
1	Thin film (~30 µm)	Hysol 1C	Square pillars (1-mm high)	5
2	Thick film (~200 µm)	Hysol 1C	Square pillars (200-µm high)	5
3	Far drop + Spin-coating	SU-8 2005, 2025, 2050	Flower, square pillars (200-µm high)	5
4	Spraying gun	SU-8 2002, 2005	Cylindrical pillars (80-µm high)	10
5	Submersion method	SU-8 2000.1, 2002, Buehler EpoThin	Cylindrical pillars (40 to 80-µm high)	10

In the first set of successful tests, a bi-component, room-temperature 20-minute conductive epoxy (Loctite Hysol 1C, which contains 1-µm silver particles) was used. This epoxy has an extremely high viscosity (200,000 to 500,000 cPs [144]) that increases rapidly from the moment it is applied due to its fast curing path at room temperature. This is probably the most relevant and stringent wetting test reported to date in the open

literature. The process is schematically illustrated in Figure 3.5. The bi-component epoxy was mixed and a thin layer (~30 μm) was applied on quartz glass using a razor blade. 15-mm square dies containing 1-mm long, 200-micron wide square CNT pillars were put on top of the epoxy layer with the CNT side in direct contact with the epoxy and a weight of 100 grams (4,300 Pa) was placed on top of the assembly. The assembly was cured for 24 hours, and the two substrates were separated by mechanical means. The CNT pillars were effectively transplanted from the original wafer to the glass containing the epoxy layer and wetting was characterized by SEM imaging.

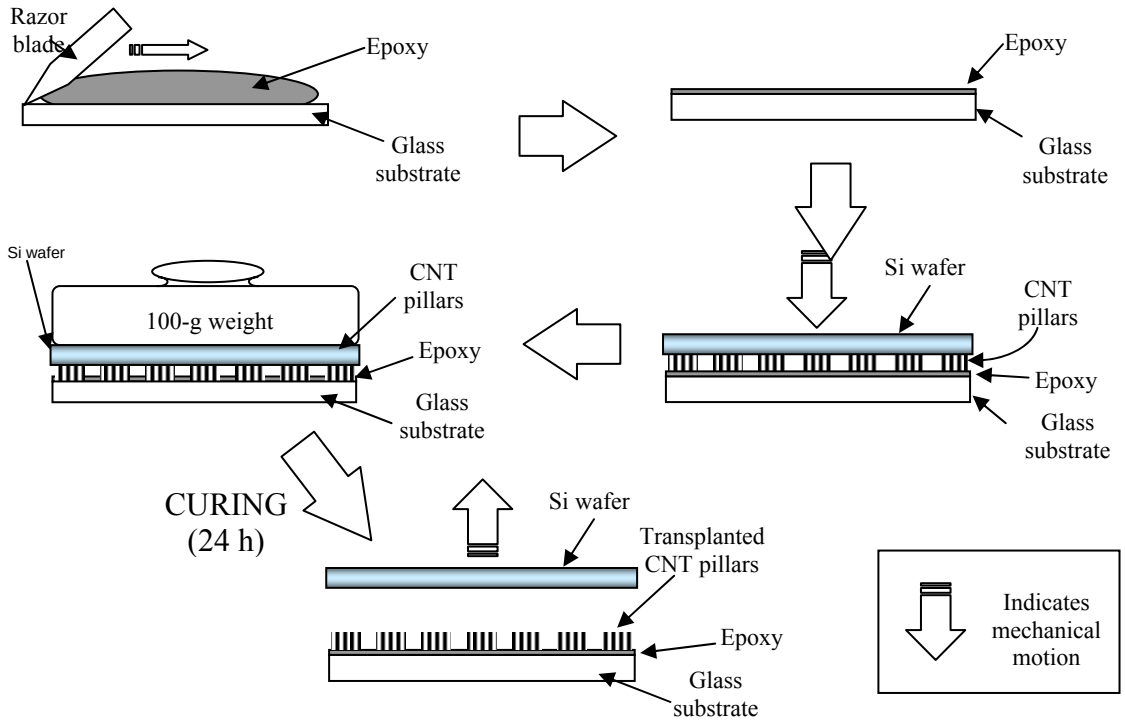

Figure 3.5: Illustration of the process used in the first two sets of tests to wet the CNTs with the highly viscous epoxy.

For the second set of tests, a thick layer (~200 μm) of the conductive epoxy was applied to quartz glass using the technique previously described (see Figure 3.5). The 200- μm wide square CNT pillars for this set of tests were 200-μm long. As in the first set

of tests, the Si die with CNTs was placed on top of the epoxy layer and a 100-g weight (4.3 kPa of pressure) was placed on top of the assembly. After 24 hours the two substrates were separated using mechanical means. A disco abrasive system (DAD-2H/6T "diesaw") was used to section the substrates.

The third set of tests used three grades of UV-curing epoxy solution: Microchem SU-8 2005, 2025, and 2050 (with viscosities of 52, 5,485 and 17,850 cPs respectively [145]). SU-8 is typically used in microfabrication. The process to wet pillars of CNTs grown on a silicon wafer, a variation of the dropwise method, is illustrated in Figure 3.6.

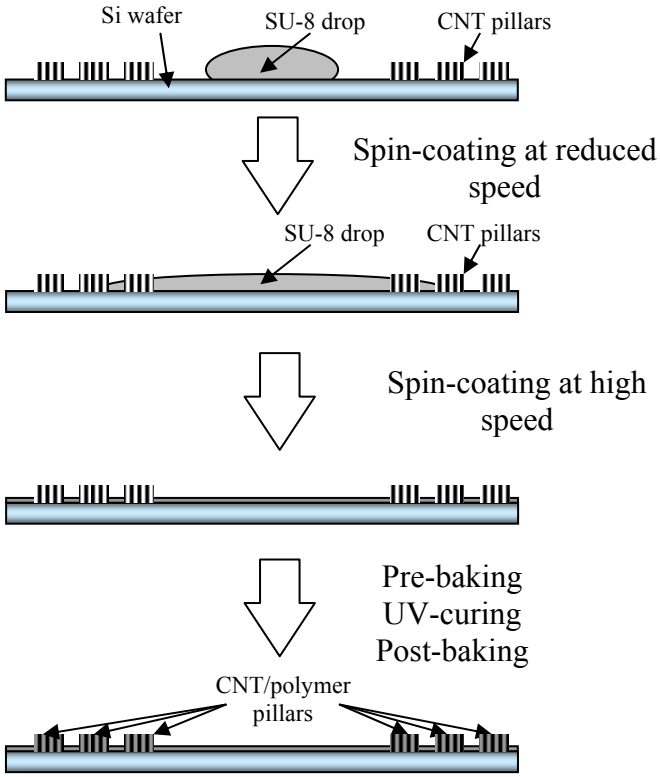

Figure 3.6: Illustration of the process used in the third set of tests to wet CNT pillars with the SU-8 resin.

Due to its low viscosity, the SU-8 is usually applied in microfabrication by spin-coating. A Headway spinner was used in this experimental work. A 2 ml drop of SU-8 was put on the wafer containing the 100-micron high CNT pattern shown in Figure

3.12.a). The SU-8 was spin-coated (Headway spinner) at low speed (250 r.p.m.) to allow the mild penetration of the polymer into the pillars (higher speeds generated higher centrifugal forces in the polymer and due to the weak adhesion of the pillars to the substrate the pillars can be spun off the wafer). Once the SU-8 is uniformly distributed on the substrate, the spinner is set at 3000 rpm for 45 seconds, creating a very thin layer (2 μm for the SU-8 2005) of SU-8. SU-8 was allowed to wet the CNT features for 3 min. at room temperature before the assembly was prebaked at 65 ºC for 1 min., and at 95 ºC for 3 min., using standard hot plates (following the SU-8 standard process). A Karl Suss MJB3 mask aligner was then used to expose the wafer to UV light (wavelength = 320nm) for 1 minute and cure the epoxy resin. The wafer was post-baked at 65 ºC for 1 min. and at 95 ºC for 2 min. to minimize residual stresses due to the curing process. The process described here is for the SU-8 2005. The other two polymer grades (SU-8 2025 and 2050) follow the same process changing the times necessary for pre- and post-baking (1+3 minutes for both pre- and post-baking for SU-8 2025; 3+6 minutes for pre-baking and 1+5 minutes for post-baking for SU-8 2050). Also for this set of tests, the CNT patterns were cross-sectioned using diesaw and SEM pictures were taken.

Trying to minimize the impact of the centrifugal forces, a spraying gun (Badger 250-2) was used in the fourth set of tests to evenly distribute SU-8 2005 (viscosity of 52 cPs) and SU-8 2002 (8.4 cPs) on the pillars. To maximize the regular distribution of the polymer, the wafer containing the grown CNTs was placed on the Headway spinner. The turning speed was set at 500 r.p.m. The SU-8 was sprayed directly on the spinning wafer at low pressure (2 bar) for 5 seconds, as seen in Figure 3.7. After contacting the CNT

pillars, the standard process recommended by the manufacturer, and described above, was followed (pre-baking, UV curing, and post-baking).

Figure 3.7: Equipment used to spray SU-8 on the CNT pillars while spin-coating in the fourth set of tests.

Epoxy and SU-8 in the four wetting tests just described effectively wet the CNTs, but contraction due to capillarity effects [121] was generally considered too high and largely uncontrollable, as shown in section 3.3.2. The pillars appeared distorted, and therefore they could not be used for mechanical characterization. Further investigation on possible fabrication methods led to the creation of a new method (described as submersion method in Table 3.1) for microfabrication of CNT/polymer composites, never reported in the literature. The method is illustrated in Figure 3.8.

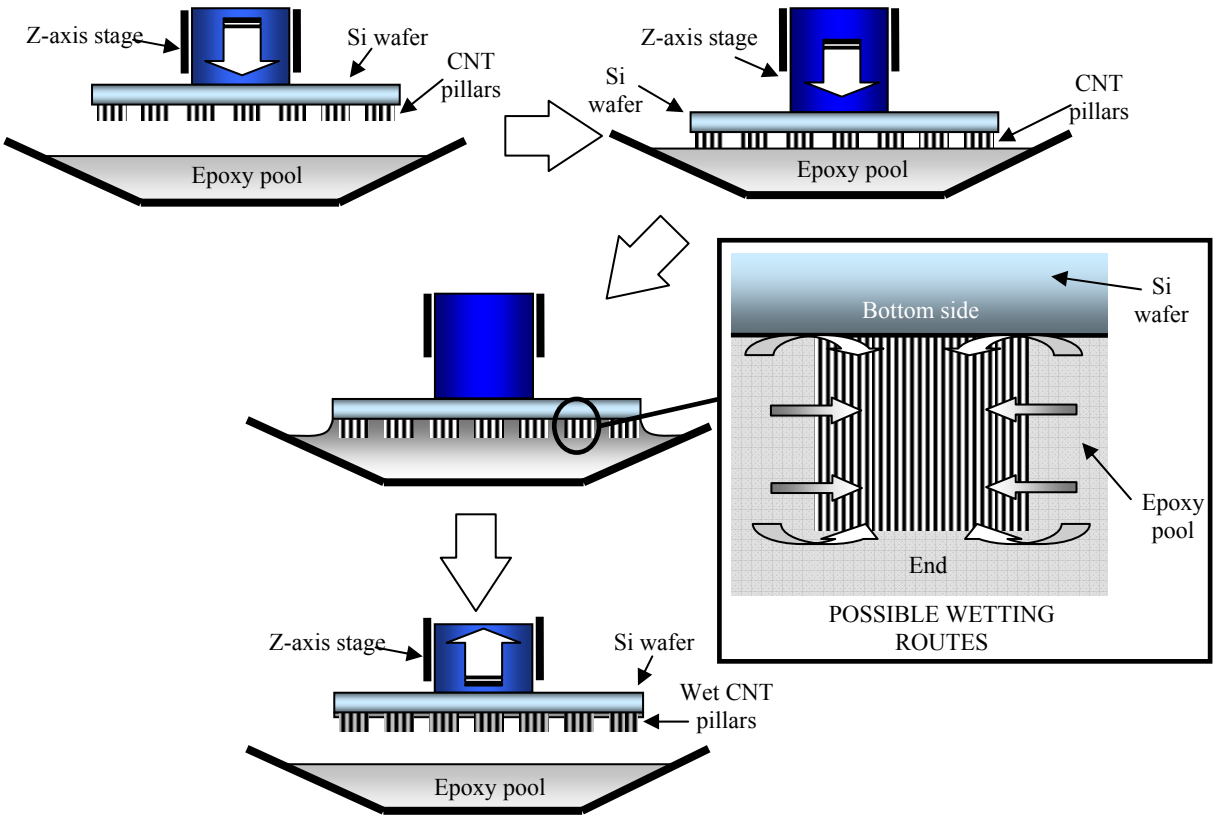

Figure 3.8: Scheme of the new submersion method used in the fifth set of tests to wet the CNT pillars with the SU-8 and EpoThin resins. Possible wetting routes are illustrated in the inset at right.

Two grades of SU-8 (SU-8 2000.1 and 2002) with even lower viscosity than SU-8 2005 (1.2 and 8.42 cPs respectively) were selected for this method. The new submersion process was also used with a commercial low viscosity (200 cPs) epoxy, Buehler EpoThin, and the results were compared with the ones obtained for SU-8.

In this process, a Si wafer containing the CNT pillars is first placed upside-down on a stage that allowed displacement in the z-axis using a micrometer with resolution of 5 μm. A small "pool" or reservoir containing the low viscosity SU-8 was placed below the stage. The stage was lowered at a reduced rate until the CNTs' tips were in contact with the SU-8 pool. At that moment, the suction forces created by the capillarity effect seem to

force the SU-8 into contact with the whole wafer, submerging the CNT pillars completely. A possible mechanism for the wetting was developed from observation of the resulting wet pillars and is illustrated in the inset in Figure 3.8. The SU-8 seems to penetrate through the pillar tips, the sidewalls and also the base, similar to a hydrostatic pressure. After 3 minutes, the stage was separated from the pool of SU-8 and the curing process continued as described previously, following the instructions of the SU-8 manufacturer (1 min. at 65 ºC and 2 min. at 95 ºC for pre-baking and 1 min. at 65 ºC and 1 min. at 95 ºC for post-baking for both epoxies). The contraction with this method was reduced and, more importantly, better controlled, leading to more regular shapes that could be used in mechanical characterization. To assess the wetting in the interior of the pillars, axial and transverse cross-sections were obtained, using a nanoindenter (Micro Materials NanoTest 600) and a Diatome Histo diamond knife mounted on a microtome (RMC Ultramicrotome MTX), respectively.

3.3.2 Results and Discussion

As mentioned in section 3.3.1, different sets of tests explored wetting of the long patterned CNT forests grown on a silicon substrate.

The dropwise method previously reported in the literature was not effective with the CNTs grown using our thermal CVD process. Likely due to the hydrophobic nature of our CNTs, the resins that we used were not penetrating the dense forest of CNTs and were creating a thin film on top of the forests instead of wetting the CNTs, as shown in Figure 3.9.

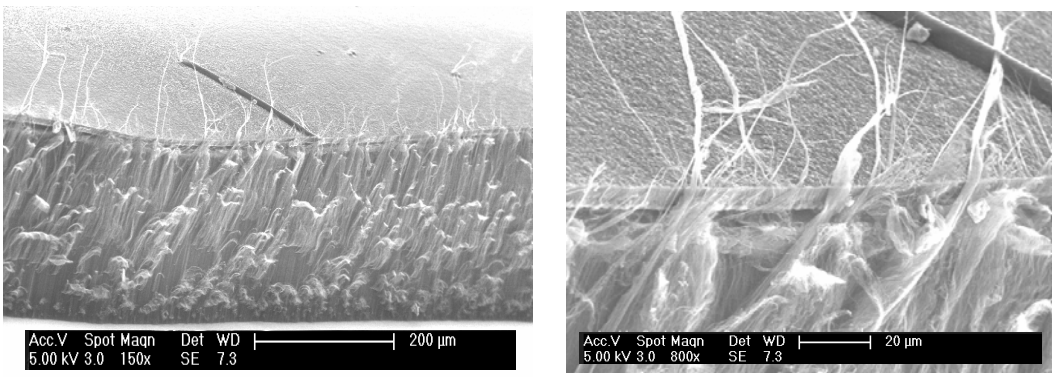

a) **b)**

Figure 3.9: SEM of a) layer of SU-8 2025 on top of a CNT forest; b) Closer image of the polymer layer not penetrating the forest.

The first successful wetting test used 1-mm long CNTs with a high-viscosity conductive epoxy resin. The epoxy resin cures in 20 minutes at room temperature, which means that its viscosity increases rapidly until it solidifies. Even with those adverse conditions, the capillarity effect [121] of the CNTs is strong enough to pull the high-viscosity epoxy resin into the CNT pillars before solidifying. An angled view of the glass substrate (where the epoxy layer was originally placed) with a pattern of transplanted CNT pillars is shown in Figure 3.10.a. The pillars were integrally separated from their original silicon substrate and firmly attached to this glass substrate by adhesion to the epoxy. The epoxy penetrated 80 microns into the pillars, as shown in Figure 3.10.b. The contrast change in the SEM images indicates the depth of penetration, where the darker areas are filled with epoxy. The deformation of the pillars at their bases is attributed to the contraction of the epoxy resin during curing (5-6%) and/or contraction due to the capillary forces pulling the epoxy into the porous CNT pillar. A close up view of two of the corners of one pillar is shown in Figure 3.10.c and d. The CNTs show good alignment even after the contraction. The 1 µm silver particles in the conductive epoxy likely

restrict the epoxy flow into the pillars, further increasing the difficulty of wetting the CNTs by this viscous epoxy.

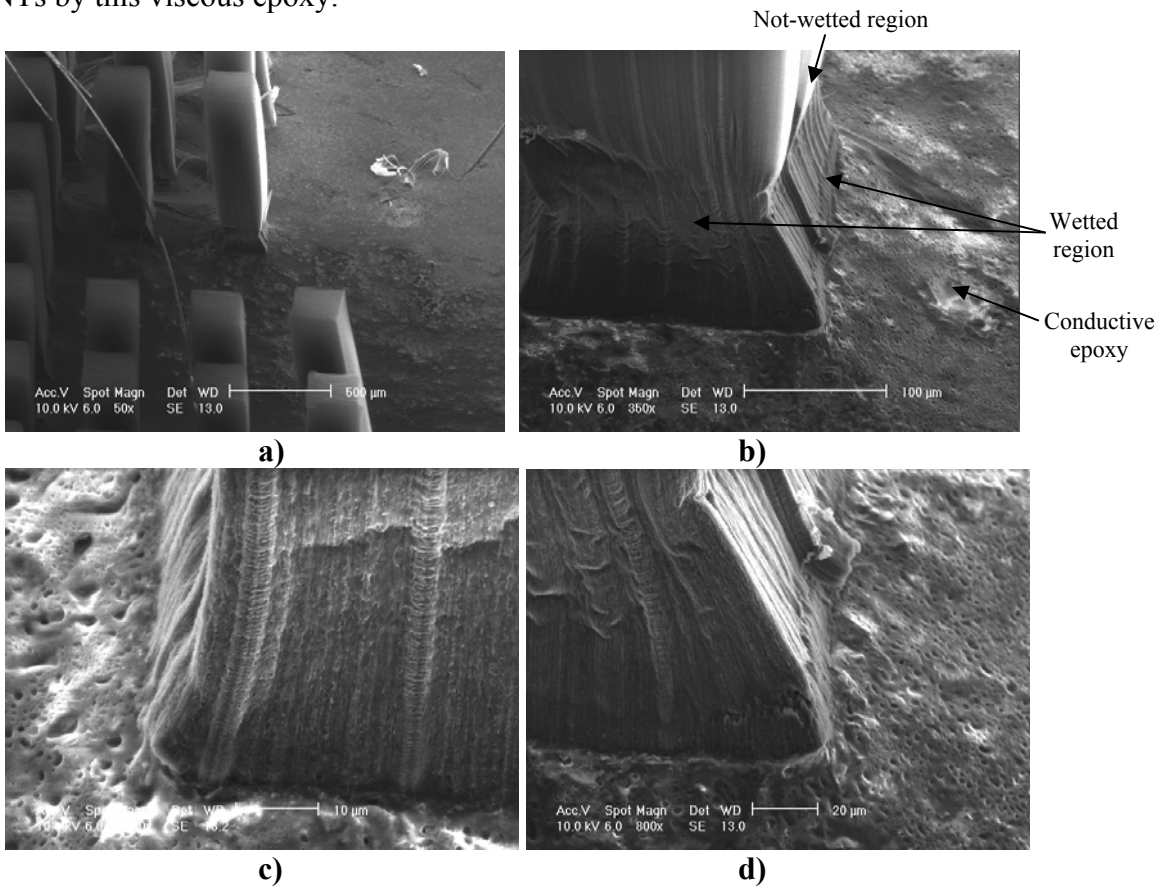

Figure 3.10: SEMs of a) 1-mm high CNT-pillars wet by conductive epoxy; b) Close up of the wet region at the base of the pillar; c) and d) closer views of the wet region at the pillar base.

The second wetting test was performed on a pattern of 200-µm long CNT pillars (shown in Figure 3.11.a) using the high-viscosity conductive epoxy used in the first test. The epoxy layer was as thick as the CNT pillar height. When the two substrates were separated by mechanical means, all the pillars were transplanted onto the glass substrate, as in the previous test. Due to the thickness of the epoxy layer, a nanocomposite film of an epoxy layer containing a pattern of highly contracted wet CNT-pillars was formed, as shown in Figure 3.11.b. The picture is of the surface of the film that was originally adhered to the silicon substrate were the CNTs were grown. The effect of the contraction

of the epoxy during curing is clearer in this test. In Figure 3.11.c, the free surface of a CNT pillar is shown (the side where the CNTs were attached to their original silicon wafer). For this viscous epoxy, significant contraction is noted. The voids, or cells, that can be seen in the center of the pillar in Figure 3.11.c and in the cross-section shown in Figure 3.11.d support this interpretation. Similar cells have been reported previously by others [121]. The 200-µm long CNT pillars shown in Figure 3.11.d were completely wet by the epoxy, from top to bottom, although not in the interior.

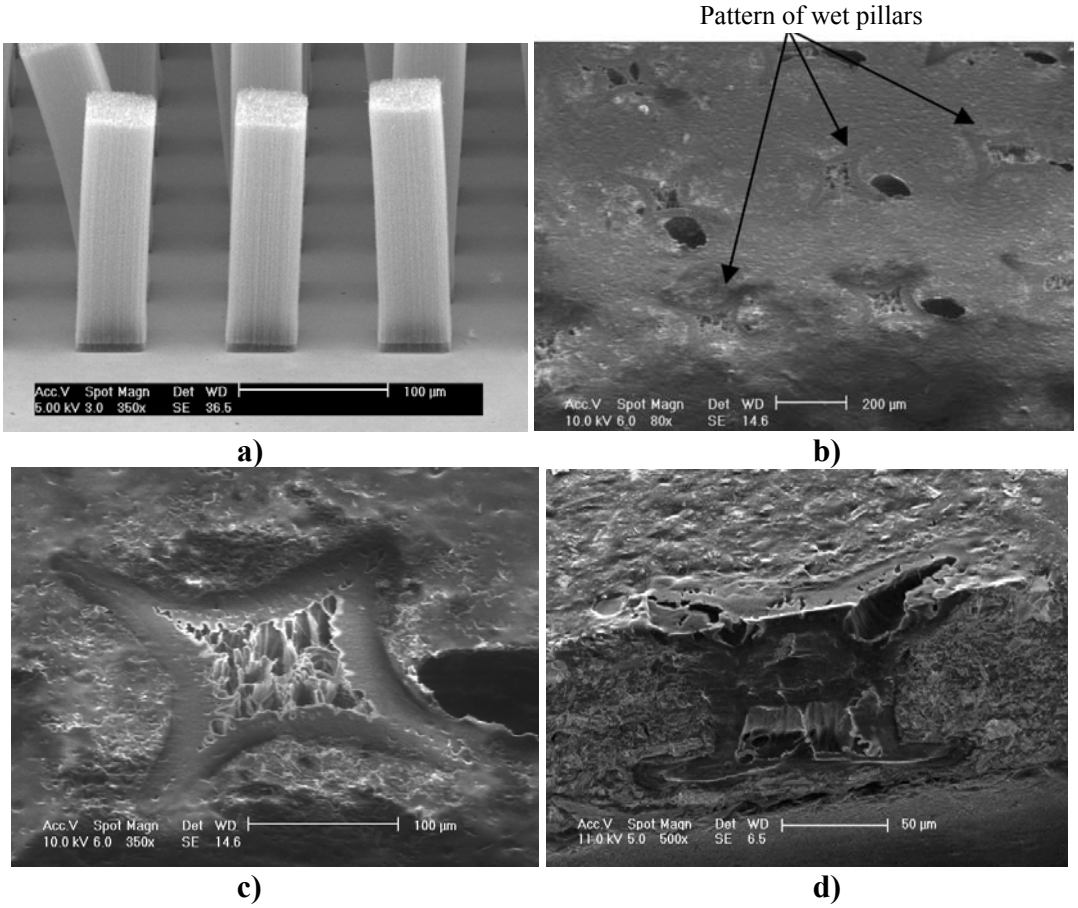

Figure 3.11: SEMs of a) Dry 100-µm high CNT-pillars; and top-down views of CNT pillars transplanted to the glass/epoxy substrate: b) Nanocomposite film made of CNT pillars wet by conductive epoxy; c) Close up of a wet pillar; d) Cross-section of a wet pillar.

Given the height of the epoxy layer, (similar to the CNT pillar height), epoxy may penetrate through the end of the pillar (as in the first set of tests), but also through the

pillar sides. While the pillar is wet from top-to-bottom, it does not appear to be wet near the center region at the top. This is consistent with the 80 μm high wetting obtained in the first tests.

For the third set of tests, a commercial low viscosity (8.4 cPs) epoxy (Microchem SU-8 2002) was used on a pattern of 100-μm high CNTs (the flower pattern shown in Figure 3.12.a). As described in section 3.3.1, the SU-8 was applied directly to the wafer containing the CNTs and spin-coated. After curing, the wafer was die-sawed to assess the wetting. A cross section of one of the flower features is shown in Figure 3.12.b.

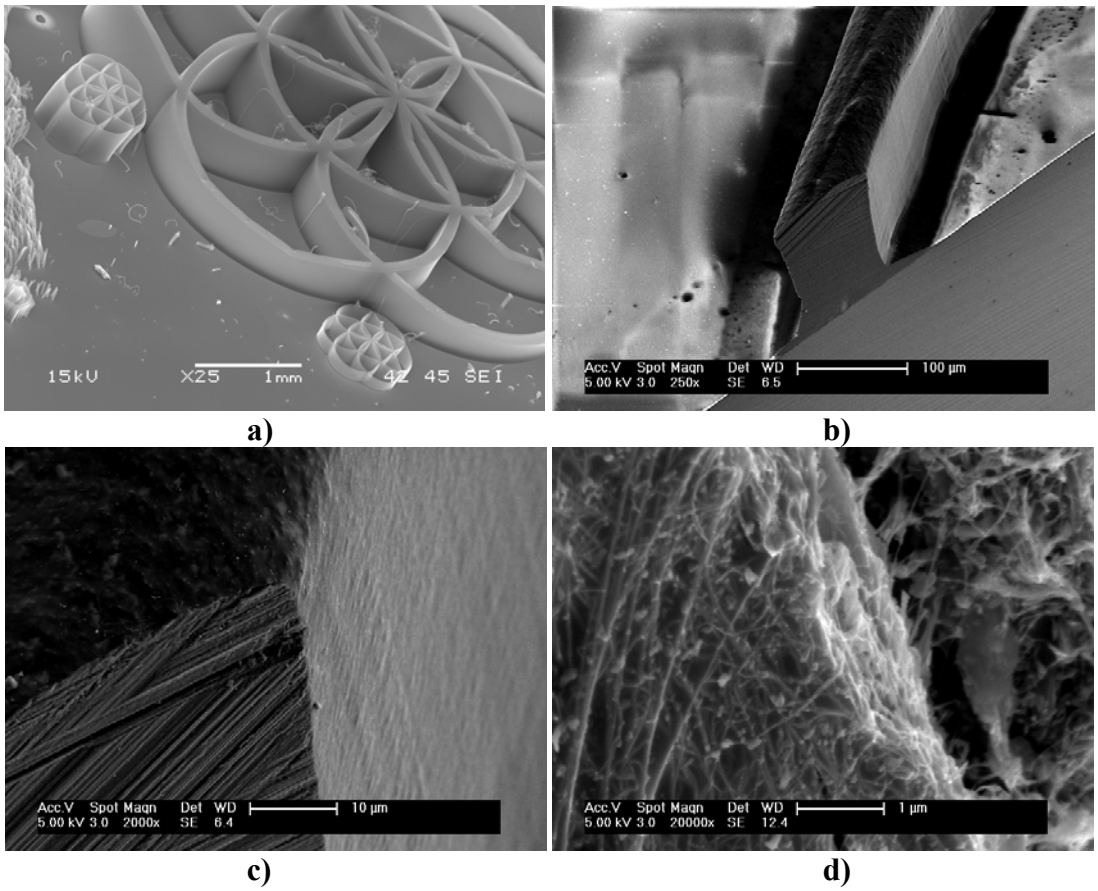

Figure 3.12: SEMs of a) Dry CNT pattern; b) Cross-section of the CNT/SU-8 feature showing good wetting; c) Close up of the top region of the cross section; d) Wetting of the CNTs.

The wetting is complete in the pillars, forming a nanocomposite feature with no voids, as seen in the closer view in Figure 3.12.c. The alignment of the CNTs is maintained, as shown in the uncut sidewall of the feature in Figure 3.12.c. The ridges of the foreground of Figure 3.12.c are due to the abrasive sectioning method. An even closer view of the wetting of the CNTs is shown in Figure 3.12.d. The wetting results shown in Figure 3.12.d are very similar to SEMs of similar magnification for fully wet aligned nanocomposite thin films [99].

In the fourth set of tests a spraying gun was used to distribute low viscosity SU-8 directly on the wafer containing the CNT pillars. The results were extremely inconsistent, ranging from no wetting at all, with SU-8 drops attached to the walls of the pillars, as shown in Figure 3.13.a), to irregular extreme contractions, as presented in Figure 3.13.c). For the spraying method, effective wetting of the pillar is associated with the presence of SU-8 at the base of the pillars. If the drops of SU-8 do not touch the base of the pillar, they may penetrate the sides, as shown Figure 3.13.d), or stay on the surface due to hydrophobic effect, as in Figure 3.13.a), depending on the size of the drop. As an example, in Figure 3.13.b) the only pillar that is fully wet is the one in the center of the picture, the only one with SU-8 at the base of the pillar (see detail in Figure 3.13.c).

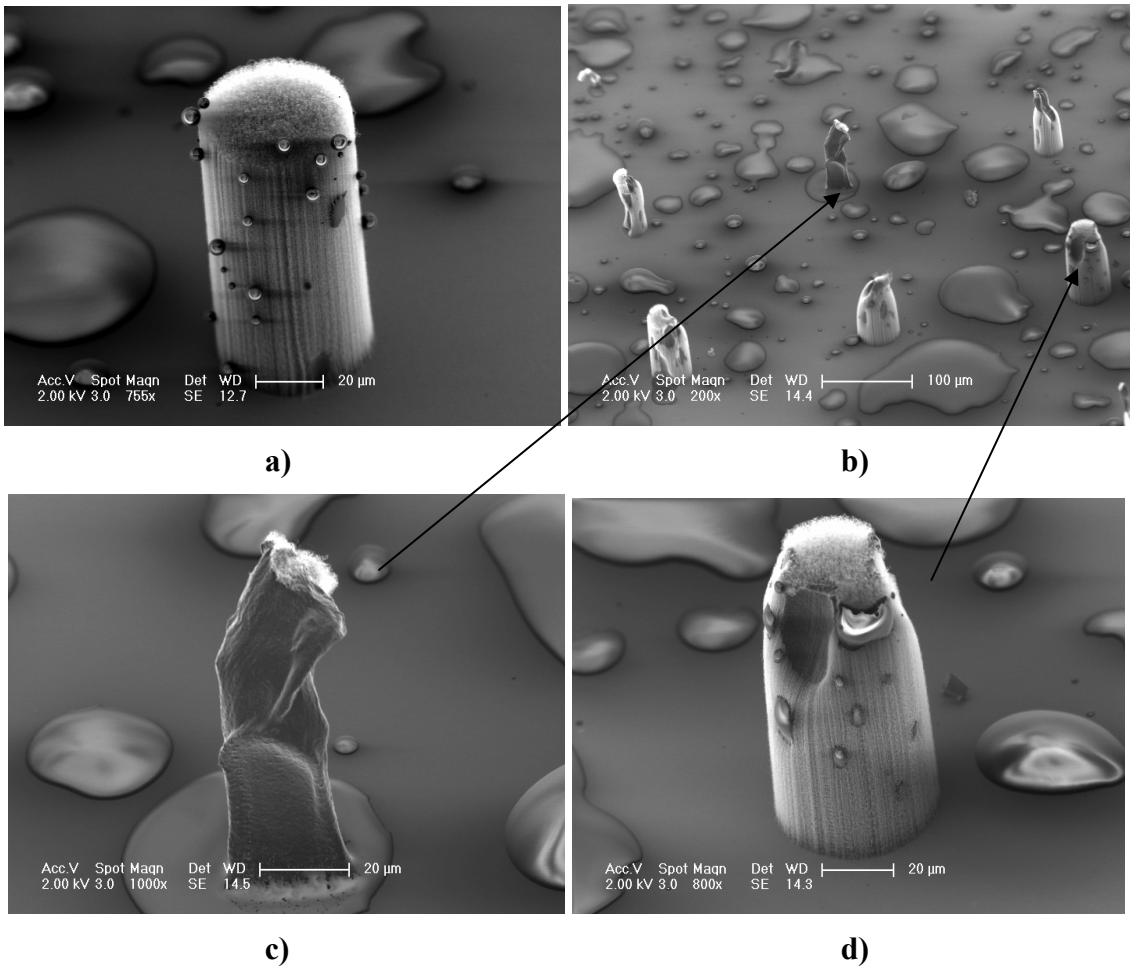

Figure 3.13: SEMs of a) Pillar with SU-8 2005 drops on the surface showing the somewhat hydrophobic nature of the CNT forest sidewalls; b) CNT-pillars pattern wet using the spraying method and a lower viscosity SU-8 (SU-8 2002); c) Pillar fully wet by the SU-8 drop at its base (extremely irregular contraction); d) Drops of SU-8 effectively penetrating the CNT pillar sidewall, but the quantity of SU-8 penetrating the structure was not enough to fully wet the pillar.

Lastly, the new submersion method used (fifth set of tests) to wet the CNTs, described in the previous section (see Figure 3.8) proved to be the most effective method to create regular nanocomposite features. As mentioned in section 3.3.1, pillars and forests of CNTs were wet by submerging the wafer into low viscosity grades of SU-8 (SU-8 2000.1 and 2002, with viscosities of 1.27 and 8.4 cPs, respectively), and a commercial low viscosity epoxy (Buehler EpoThin, 200 cPs at 25º C). It is believed that

the nearly hydrostatic pressure generated by the capillarity effect produced a higher rate of regularly contracted pillars compared to the other methods.

The low viscosity commercial epoxy was not suitable for creating nanocomposites with small, short pillars, because it creates a 50-75 μm layer around the pillars, covering them almost completely. Using the process with the low viscosity SU-8 grades, the small pillars generally maintained their original shapes and remained perpendicular to the wafer, as shown in Figure 3.14 (pillar wet using SU-8 2000.1) and Figure 3.15 (pillars wet using SU-8 2002). Note the clearly visible deficit of epoxy near the base of the wet pillars in Figure 3.15, indicating wetting proceeds up through the pillar base (as illustrated in Figure 3.8).

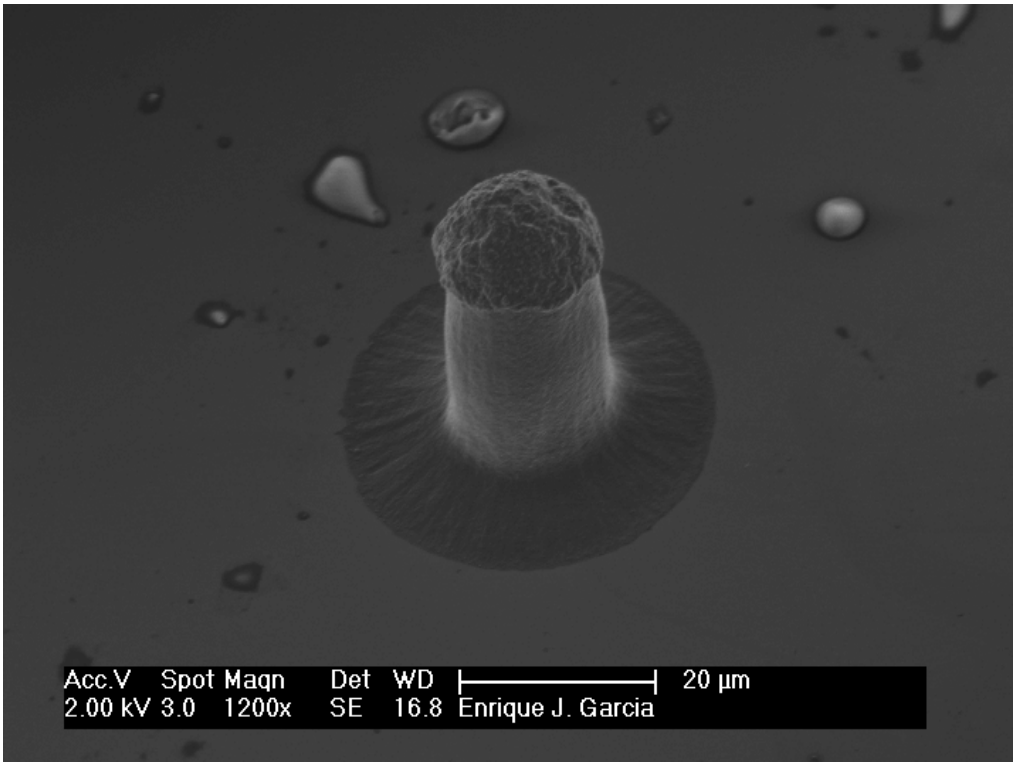

Figure 3.14: SEM of pillar fully-wet using SU-8 2000.1. The pillar is highly contracted (the original diameter of the pillar is shown by the dark circle around the base of the pillar), however the regularity of the contraction produced during wetting maintained the cylindrical shape.

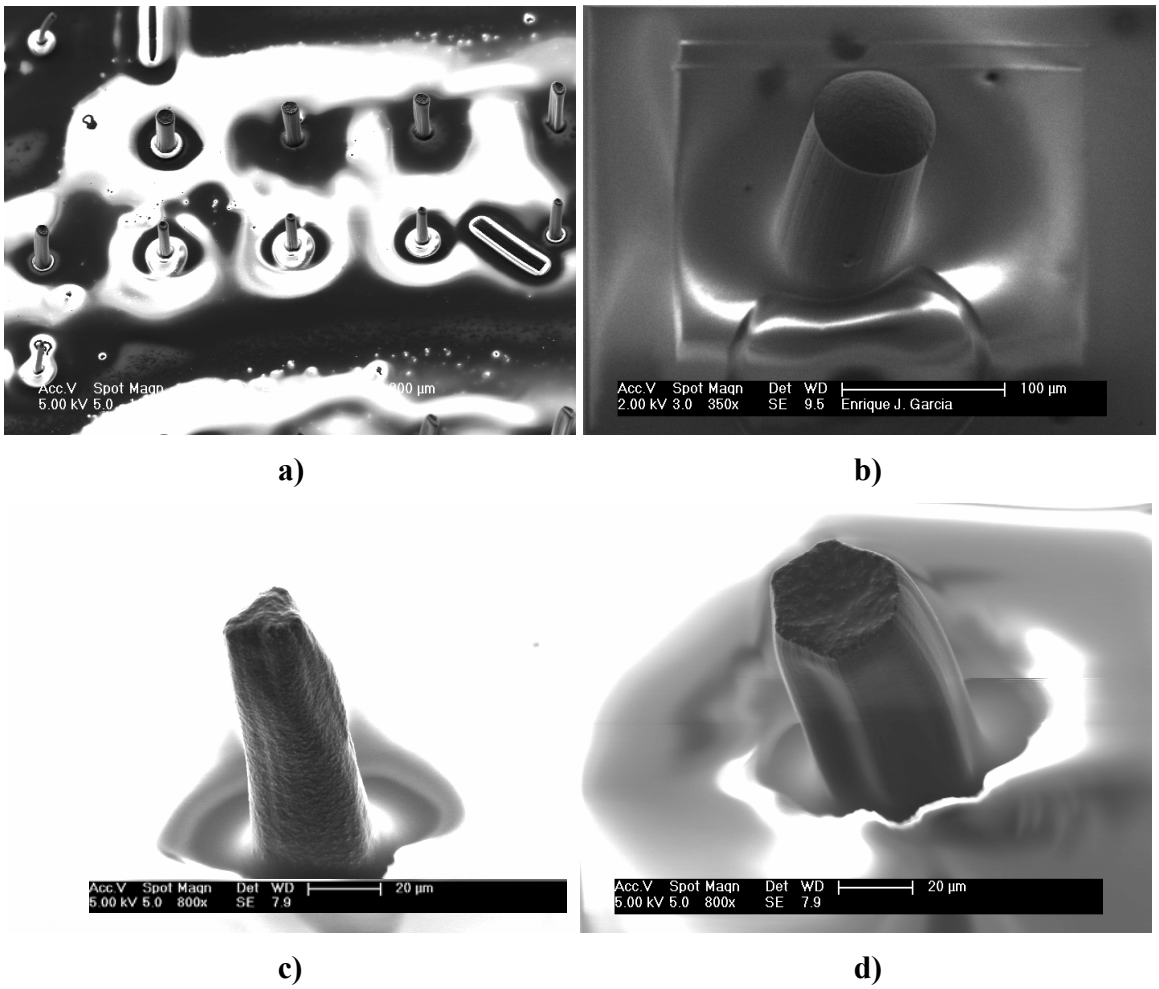

Figure 3.15: SEMs of pillars wet using SU-8 2002: a) Pattern of fully-wet cylindrical nanocomposite pillars; b) 80-µm diameter cylindrical pillar of; c) Triangular nanocomposite pillar; d) Hexagonal nanocomposite pillar with preserved shape.

In order to assess the wetting inside the small pillars, mechanical methods were used to create cross-sections. Due to the small diameter of the pillars and their relatively high aspect ratio, it was not possible to use the diesaw or the microtome used previously. However, a transverse cross-section of one pillar wet using SU-8 2000.1 was obtained by means of a nanoindenter (Micro Materials NanoTest 600) as a result of a misaligned preliminary nanocompression test, as shown in Figure 3.16. The total absence of voids

indicates full wetting. It is important to note in Figure 3.16.b) that wetting does not destroy the alignment of the CNTs inside the pillars using low viscosity SU-8 2000.1.

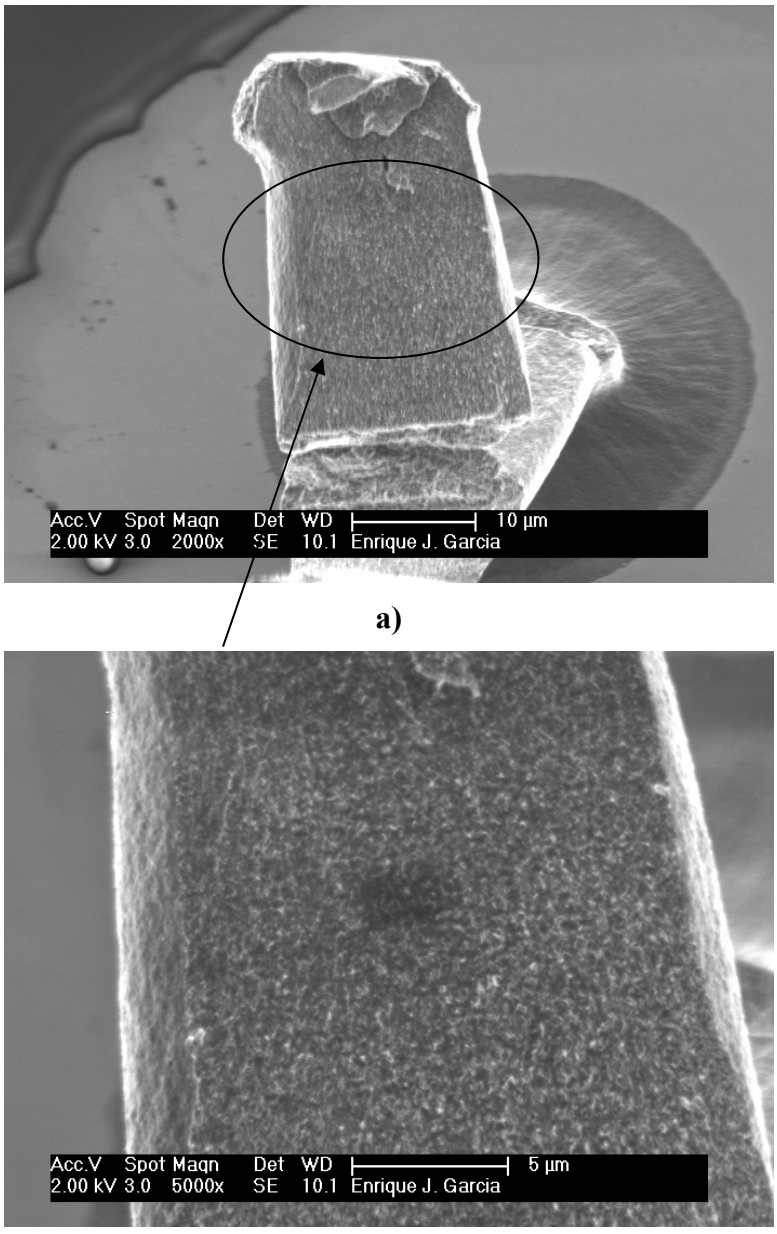

Figure 3.16: SEMs of a) Vertically cross-sectioned nanocomposite pillar; b) Zoom-in of the cross-section surface of the pillar showing the effective wetting of the CNTs. Note that the alignment of the CNTs is maintained during wetting which is visible particularly at the sidewalls.

The use of one SU-8 grade or the other has advantages and disadvantages for small pillars. The contraction in small cylindrical pillars produced by the SU-8 2000.1 grade (see Figure 3.14) is much higher than using SU-8 2002 (pillar in Figure 3.15.b). However, the alignment and verticality of the pillars is generally better using SU-8 2000.1. Another important advantage of the SU-8 2000.1 over SU-8 2002 is that due to its lower viscosity, the 2000.1 grade produces only a thin layer (2-3 μm) of polymer around the pillars. SU-8 2002, on the contrary, generated a layer of polymer around the pillars that varies from 5 to 10 μm. This layer can modify the experimental results obtained with the nanoindenter for small pillars, making SU-8 2000.1 a better polymer matrix to create nanocomposite pillars to test in compression using the nanoindenter.

For large cross-section pillars and forests, the capillarity forces using low viscosity SU-8 (grades 2002 and especially 2000.1) lead oftentimes to extreme contractions, as seen in Figures 3.17.a) to d). Some features, as in Figure 3.17 b) and Figure 3.17.d), show significant contraction combined with folding. Even if contraction is very strong, its regularity is still evident and especially noticeable in Figure 3.17.d). The alignment of the CNTs is maintained even in these extreme conditions. The results for the low viscosity commercial epoxy (EpoThin) are much better in terms of maintaining the original pillar shape, as shown in Figure 3.17 e) and Figure 3.17.f).

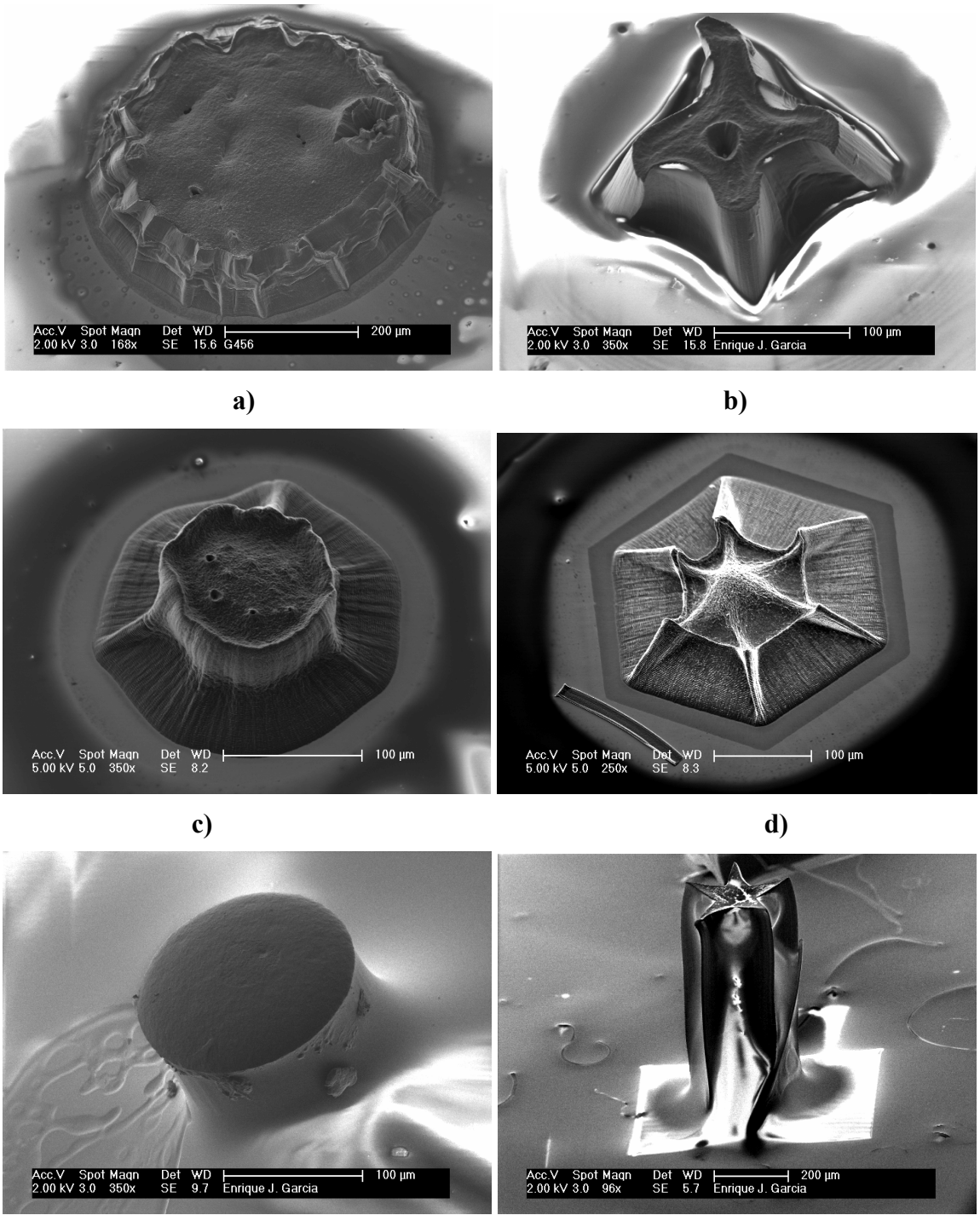

Figure 3.17: SEMs of a) Cylindrical pillar wet by SU-8 2002; b) Square pillar wet using SU-8 2002; c) Highly contracted cylindrical pillar wet by SU-8 2000.1; d) Hexagonal pillar wet by SU-8 2000.1 (note the regularity of the contraction and the alignment of the CNTs even after the extreme contraction and folding); e) Cylindrical pillar wet by EpoThin low viscosity epoxy; f) Star-shaped long pillar wet using EpoThin.

Contraction using SU-8 2000.1 always generates results such as the ones shown in Figures 3.17.a) to d). However, around 10% of the tests using SU-8 2002 provided extremely regular large pillars and forests, such as the ones shown in Figure 3.18 and Figure 3.20. The wetting in the interior of the pillars created was assessed using a microtome (RMC Ultramicrotome MTX). For the pillar shown in Figure 3.18, no voids appeared after microtoming the pillar transversally, indicating complete wetting in the interior. The white spots in Figures 3.18.b) and c) are due to the accumulation of epoxy during microtoming.

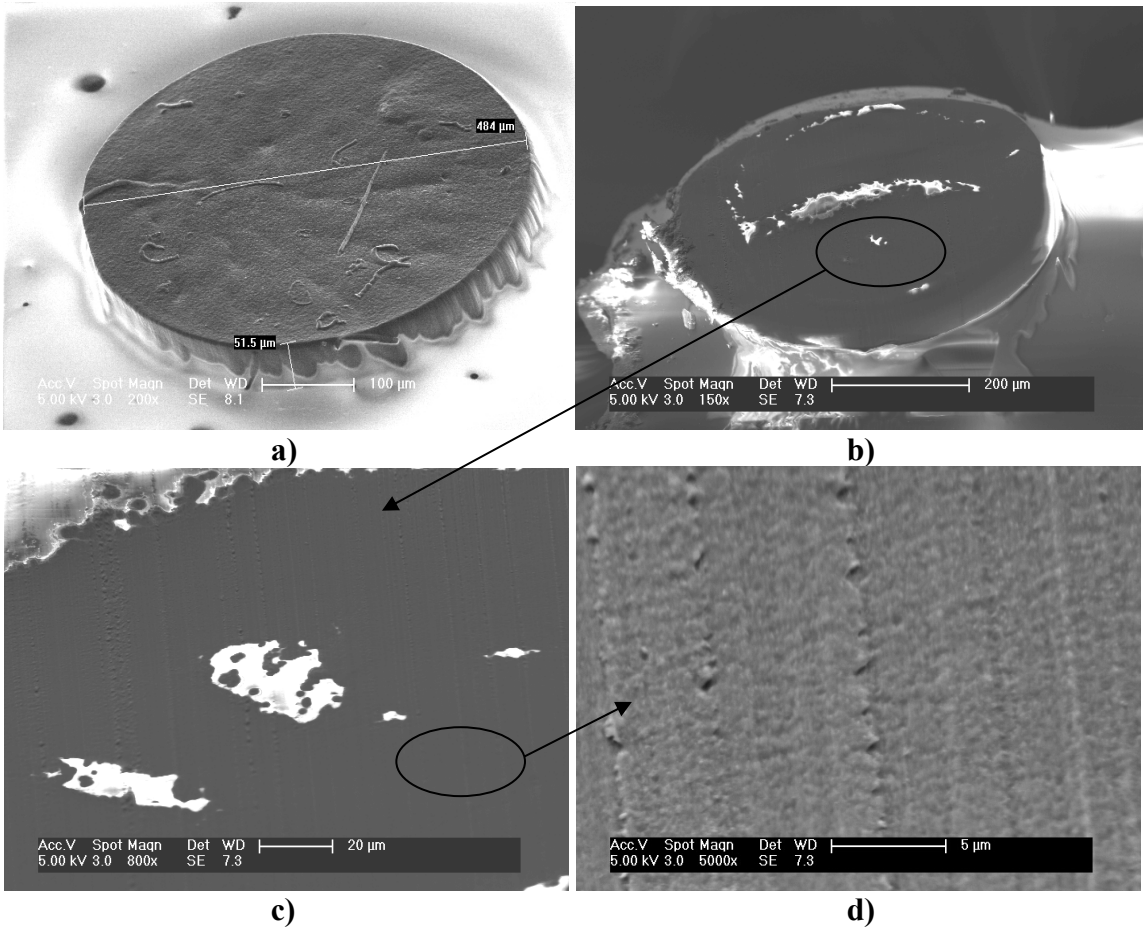

Figure 3.18: SEMs of a) Pillar of CNTs after being wet by SU-8 2002 epoxy resin; b) Same pillar after microtoming its top surface; c) Zoom-in of the microtomed surface of the pillar; d) Closer view of the microtomed surface, showing complete wetting.

Most of the pillars (90%) wet with SU-8 2002 presented, however, void (cells) after microtoming the surface, as shown in the two examples in Figure 3.19.

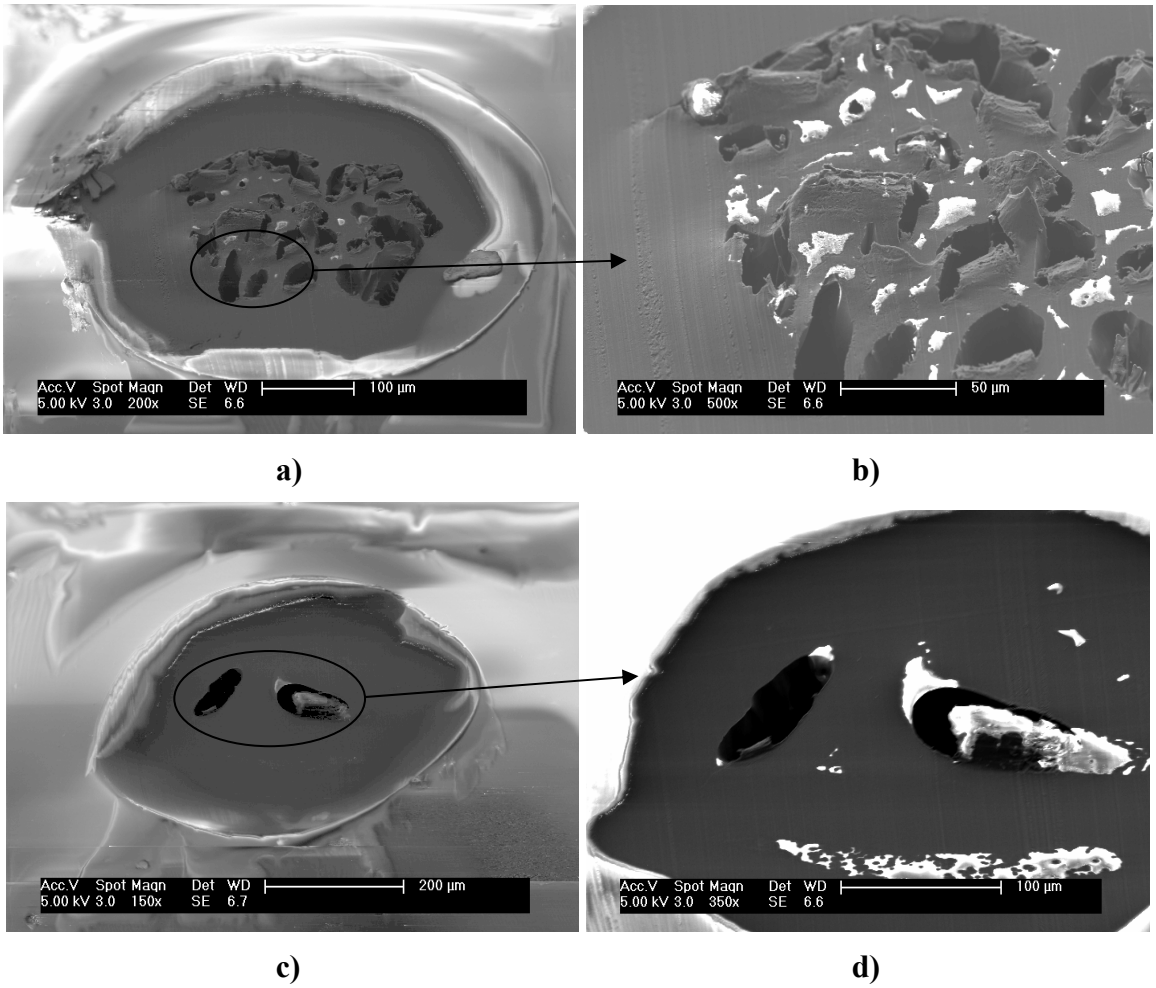

Figure 3.19: SEMs of a) Microtomed pillar with cell structure; b) Closer view of the multiple cells formed during wetting; c) Another microtomed pillar with 2 large voids created during wetting with SU-8 2002; d) Closer view of the voids. Note the effective wetting (no micro-voids) around the voids.

As mentioned previously, the new method was also effective in wetting dense forests of aligned nanotubes. None of the methods previously used had been able to generate good wetting results for forests of CNTs. Submerging the CNT forest in SU-8 2002 proved to be the most effective way to create nanocomposite forests that maintained the original height and alignment, while producing good wetting results, as shown in

Figure 3.20. A cross-section of the forest, shown in Figure 3.20.b), was obtained using a DAD-2H/6T diesaw. The lack of voids, the alignment of the nanotubes, and the maintained height provide good evidence of effective wetting.

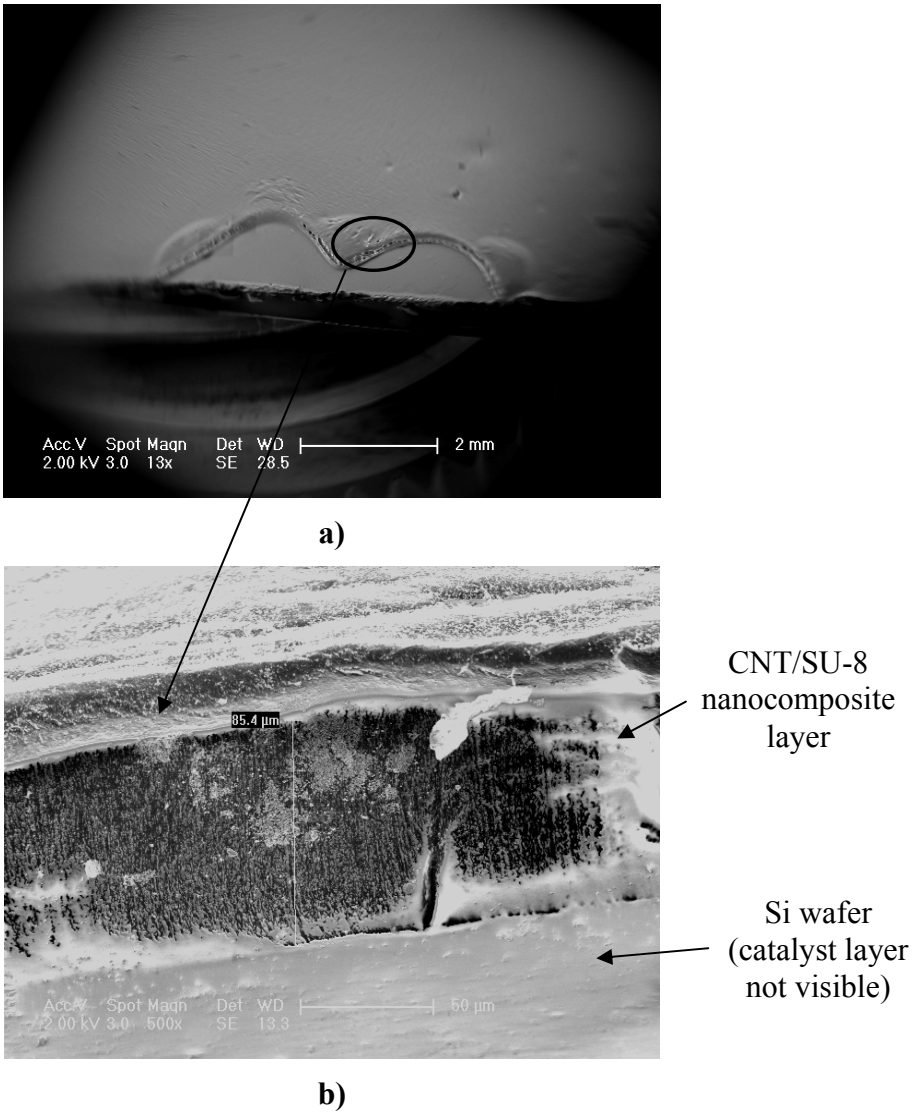

Figure 3.20: SEMs of a) dense forest of CNT completely wet after submerging the wafer in SU-8; b) diesawed cross-section of the wet forest (note the alignment of the CNTs).

3.3.3 Summary of Wetting Results

Wetting of CNTs with different commercially available epoxy resins is possible, even using high-viscosity, rapid curing epoxies filled with large conductive particles. These are the most stringent wetting conditions reported to date in the literature. The different tests performed allowed identification of the primary factors controlling wetting of the CNTs:

- The first factor in terms of importance is the viscosity of the epoxy. Higher viscosities produce extreme contractions and tend to create voids like the ones shown in Figure 3.11. Lower viscosities allow a better control of the contraction, which translates into regularly-shaped pillars, as the ones presented in Figure 3.14 and Figure 3.15.

- The route followed by the epoxy to wet the pillars has also been investigated. As shown by the spray tests (see Figure 3.13), the most effective wetting is produced through the base of the pillars, while the wetting through the side walls is less effective, which is attributed to the amount of epoxy in contact with the CNTs. This limitation due to lack of polymer in the side and top walls was reduced by the new microfabrication method (submersion method) developed in this research (see Figure 3.8). Good evidence for all three routes shown in the inset of Figure 3.8.

- The volume fraction of CNTs is another important factor in the wetting. The volume fraction of as-grown CNTs in this work was maintained at ~0.9%, but some interesting conclusions can be extracted from the results obtained: Higher

volume fractions would increase the difficulties of individually wetting the CNTs without forming aggregates, especially with high-viscosity epoxies. The regularity of the contraction could also be compromised by high volume fractions. Reduced CNT height, such as would be desired for interlaminar or intralaminar reinforcement, would mitigate the contraction based on the results from the wetting studies herein.

- The height of the pillars also plays a role in the wetting process. Rapid curing epoxies (usually with high viscosities), like the ones used for the first test (Figure 3.10), do not fully wet long pillars. However, for lower viscosity epoxies, the CNT height is not a factor in the effectiveness of the wetting (for the heights obtained using this method, 3 mm maximum). Pillars as high as 1.5 mm have been effectively wet with SU-8 2002 and EpoThin (with viscosities of 8 and 200 cPs, respectively). The pillar height is an important factor in the regularity of the contraction and the maintenance of the original shape of the CNT pillars. In general, shorter pillars (~ 50-80 μm) produce more regular shapes for all epoxies tested.

- The cross-sectional shape of the pillars is also important in terms of contraction. Wetting with both low and high viscosity epoxies are very sensitive to the presence of sharp corners. When the epoxy penetrates into the pillars, the corners rapidly contract (increasing the volume fraction of CNTs), generating patterns of contraction as shown in Figure 3.11.c (high viscosity epoxy), Figure 3.17.b (SU-8 2002), and Figure 3.17.d (SU-8 2000.1).

- Finally, the width of the pillar is of special importance during wetting. With the volume fraction used in this work (around 0.9%, as discussed in section 3.2), larger diameters increase the probability of formation of voids or cell structures, such as the ones presented in Figure 3.19. Smaller diameters are more effective in keeping the regularity in the shape, as seen in Figure 3.14 and Figure 3.15, and avoid cell/void formation.

After demonstrating that wetting of CVD grown aligned CNTs is possible, this work will next focus on the mechanical properties of the CNT/epoxy nanocomposite materials created using the new submersion method developed during the research.

3.4 Mechanical Characterization Using Nanoindentation

The goal of this part of the research was to characterize the mechanical properties of the well-aligned CNT/epoxy nanocomposites and to assess the effectiveness of the CNT reinforcement by comparing the results with the ones obtained for the unreinforced polymers.

The mechanical properties (Young's modulus, hardness) of thin films containing randomly oriented CNTs inside a polymer matrix have been reported using nanoindentation techniques [124]. However, no mechanical characterization based on direct measurements has been reported to date for CVD-grown well-aligned CNT/polymer nanocomposites. Fang *et al.* [129] used Berkovich nanoindentation to determine the hardness of their PE-CVD MWCNT/parylene nanocomposites. However, they used indirect methods, the resonance frequency method on microbridges (~20-µm square cross-section) and microcantilevers (~20-µm x 50-µm rectangular square cross-

section) to determine the elastic modulus of this material. The modulus was derived from the vibration measurements using a simplified model based on Euler-Bernouilli homogeneous beam theory. In Fang's paper, the results obtained from microbridges and microcantilevers were different, partly because of the modeling assumptions, but also, as the authors noted, due to deviations in film thickness and in the measurements. Curiously, modulus from nanoindentation was not reported.

A characterization using direct measurement methods, not dependent on structural models, is believed to provide more reliable results. Berkovich and spherical nanoindentation, and more importantly compression tests using a diamond flat punch mounted on a nanoindenter, were used in this research to obtain more direct measurements of the mechanical properties of the CNT/epoxy nanocomposites created using the techniques described in section 3.3. Two different epoxies were selected from the ones tested in section 3.3: low viscosity Buehler EpoThin epoxy, and two grades of Microchem SU-8 (2000.1 and 2025). A summary of the sets of tests performed to mechanically characterize the CNT-reinforced nanocomposites is presented in Table 3.2.

Table 3.2: Test matrix of mechanical nanocomposite tests.

Set of tests	Type of test	Material	Specimen	Number of tests
1	Berkovich indentation	EpoThin	Film (500-µm high)	12
2	Spherical indentation	EpoThin	Film (500-µm high)	12
3	Spherical indentation	CNT/EpoThin	Cylindrical pillars embedded into EpoThin film (500-µm high)	12
4	Compression	CNT/EpoThin	Cylindrical pillars (500-µm high)	10
5	Berkovich indentation*	SU-8	Film (40-µm high)	30
6	Compression	SU-8	Pillars (40-µm high)	30
7	Compression	CNT/SU-8	Pillars (40-100-µm high)	25**

* Berkovich nanoindentation of CNT/SU-8 nanocomposites gave highly variable and inconsistent results and are not reported (see discussion in section 3.4.2).

** Nineteen of these tests failed to create a state of uniaxial compression and the CNT/polymer nanocomposite pillars fractured in a bending mode as discussed in section 3.4.2.2.

3.4.1 Experimental Methods

Due to the scale of the aligned CNTs, it was impossible to use conventional universal testing machines to determine the mechanical properties of the CNT/epoxy nanocomposites along the CNT axis. The mechanical characterization of the nanocomposites containing CNTs grown with the thermal CVD process used in this research employed different nanoindentation techniques. Initially, Berkovich and spherical nanoindentation tests were performed on pure epoxy films and microtomed surfaces of nanocomposites using two different epoxy matrices. Using the same nanoindentation principle with a flattened diamond punch, compression tests were also

performed on nanocomposite pillars. As discussed in section 2.2.2, a compression test using a flattened punch mounted on a nanoindenter has been successfully used to mechanically characterize micro-scale metal pillars [134] and also the buckling of pure CNTs [75]. However, this technique had never been used on nanocomposites before this research. The compression test applied to nanocomposite pillars is shown schematically in Figure 3.21. In order to quantify the effective reinforcement of the CNTs in the polymer matrix, compression tests were also applied to pure polymer pillars of the SU-8 epoxy. The SU-8, in contrast to the EpoThin, more easily allows pillar fabrication due to the UV-curing and patterning standard microfabrication procedures for this material.

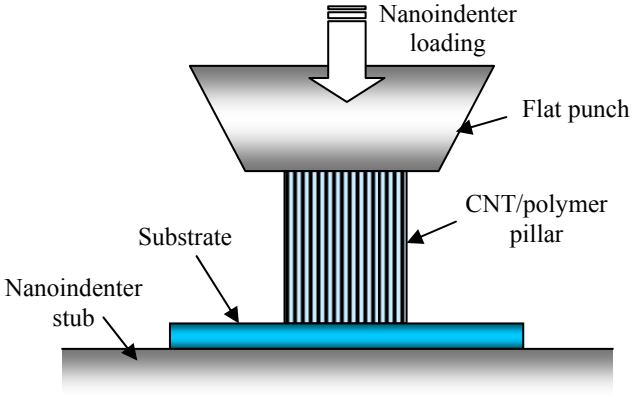

Figure 3.21: Illustration of compression test of an aligned CNT nanocomposite using a nanoindenter.

The experimental work for the mechanical characterization can be divided into three categories: Microfabrication of pillars and films made out of pure polymer and CNT/polymer nanocomposites, traditional Berkovich and spherical nanoindentation of polymer and nanocomposite films, and compression tests applied to pure polymer and CNT/polymer nanocomposites pillars.

3.4.1.1 Microfabrication of CNT Films and Pillars

Taking into account the results of wetting of the CNTs using different polymers reported in section 3.3, the two polymers that were selected as matrices for the nanocomposites were EpoThin epoxy from Buehler and Microchem's SU-8 (2000.1 and 2025, with nominally the same mechanical properties). For both epoxy resins, films and pillars of pure polymer and nanocomposites were created using microfabrication techniques.

Buehler's EpoThin is a commercially available low viscosity (200 cPs at room temperature) epoxy that, as seen in section 3.3.2, provided good wetting results for large pillars (above 300 μm in diameter and 500 μm in height). Pure EpoThin films and CNT/EpoThin nanocomposite films and pillars were created using the different techniques described in section 3.3.1.

500-μm thick films of pure EpoThin epoxy were created by applying a 2-ml drop of the resin on top of a glass substrate and spin-coating (Headway spinner) at 500 rpm for 30 seconds. The epoxy was cured at room temperature for 24 hours. After curing, the surface was microtomed (RMC Ultramicrotome MTX with a Diatome Histo diamond knife) in the Microsystems Technology Laboratory at MIT of to provide a regular and flat surface for the nanoindentation tests. SEM microscopy was used to verify the regularity of the surface and the thickness of the layer.

To create films and pillars of CNT/EpoThin nanocomposite, the novel technique described in Figure 3.8 and used for the most successful wetting tests was used. 225-μm diameter cylindrical CNT pillars were grown on a silicon substrate to a height of 1 mm. The substrate containing the CNTs was placed upside-down on a z-stage above a small

reservoir containing a thick layer of EpoThin. The stage was lowered until the CNT pillars touched the epoxy surface and the wetting process was allowed for 5 minutes. After 5 minutes, the wafer was separated from the epoxy and the wet pillars were allowed to cure for 24 hours at room temperature. After curing, the surface of the pillars was microtomed to planarize the surface for the compression tests. SEM was used to select pillars for compression tests and also to determine the dimensions of each one of these pillars (height and surface area of the top of the pillar). A representative pillar is shown in Figure 3.22. As seen in the SEM image, the EpoThin creates a honeycomb structure in the interior of the pillars, while keeping a thick layer of fully wet CNTs at the sidewall. This contraction effect is similar to the wetting results shown in Figure 3.11 for the high-viscosity conductive epoxy. Due to the lower viscosity of the EpoThin, the cell structure is more regular.

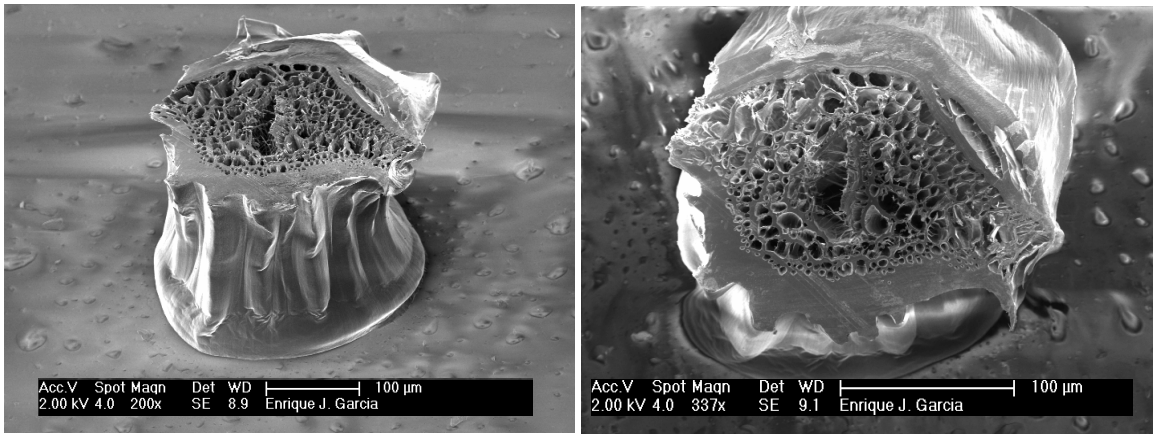

a) **b)**

Figure 3.22: SEMs of a) side view of a representative CNT/EpoThin pillar before applying the compression test; b) Top view of the same pillar, showing the cell structure created by the EpoThin during wetting.

The films containing CNT pillars were created using a variation of this method: Instead of making the CNT pillars contact the epoxy surface, the pattern of CNT pillars

was fully submerged into the epoxy layer for 5 minutes and after separating the wafer from the epoxy, the film generated was cured for 24 hours at room temperature. Also for this type of specimen, the surface was microtomed before the nanoindentation tests were performed.

The other polymer selected to create the nanocomposite films and pillars was Microchem's SU-8 epoxy. The three main reasons why this polymer was selected for these tests are:

- Due to its UV curing activation, it is possible to selectively cure 2D patterns to create 3D structures. SU-8 has been used in the fabrication of microfeatures, such as microchannels, micromolds, and also pure epoxy pillars like the ones used in this research. It was not possible to create pillars of pure EpoThin epoxy to compare the results obtained from compression tests for the CNT/EpoThin nanocomposites.
- There was no need to microtome the surface of the pure SU-8 films or pillars, as described for EpoThin epoxy.
- As shown in section 3.3, this polymer is the most effective matrix in the creation of regularly contracted, fully wet, vertically aligned nanocomposite pillars.

The process used to create the pure SU-8 films and pillars for compression and nanoindentation tests is very similar to the one described in section 3.3 for the third set of wetting tests: A 2 ml drop of SU-8 2025 was placed on a previously cleaned Si wafer. After spin-coating (Headway spinner) the wafer at 1000 rpm for 45 seconds, a 40-μm layer of SU-8 was created. Then the wafer was prebaked at 65 ºC for 2 min., and at 95 ºC

for 5 min., using standard hot plates (following the SU-8 standard process). A Karl Suss MJB3 mask aligner with a previously fabricated mask was then used to selectively expose the wafer to UV light (wavelength = 320nm) for 1.5 minutes and cure the SU-8 pillars of different sizes (big cylinders for the Berkovich indentation and a regular pattern of cylindrical pillars with a diameter of 40 μm). The wafer was post-baked at 65 ºC for 1 min. and at 95 ºC for 3 min. to minimize residual stresses due to the curing process. The uncured SU-8 around the cured SU-8 pillars was removed using poly-methyl acetate. The resulting patterns of large pillars (ranging from 200 to 600 μm in diameter) and the pattern of 40-μm pillars are shown in Figure 3.23. The resulting pillars have a flat surface after the curing process is complete, not needing to be microtomed for nanoindentation and compression tests.

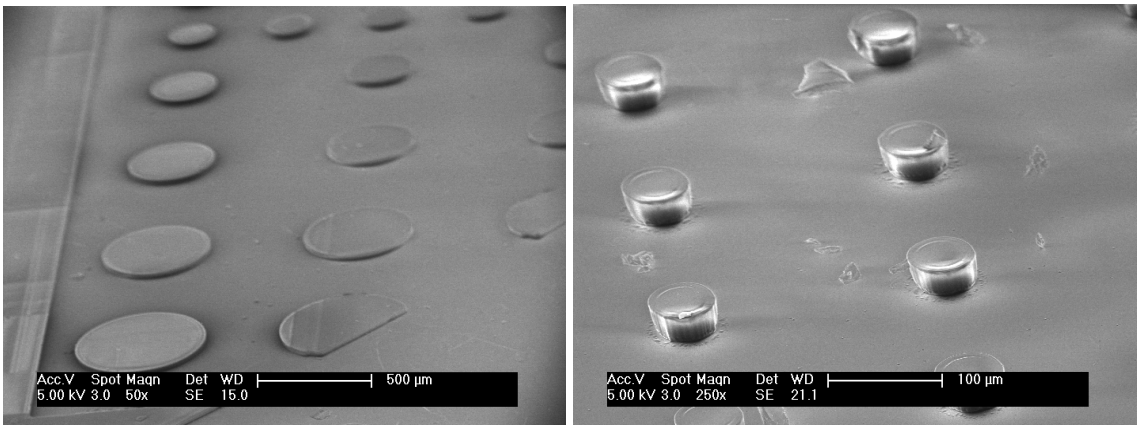

a) **b)**

Figure 3.23: SEMs of a) pattern of large pillars for Berkovich nanoindentation; b) 40-μm diameter SU-8 pillars used in the compression tests.

CNT/SU-8 nanocomposite pillars were created using the method used for the EpoThin pillars (and previously described in section 3.3.1, Figure 3.8). First, cylindrical CNT pillars with different diameters were grown on a Si wafer using the thermal CVD process. As mentioned previously, it is possible to control the height of the CNT pillars

by changing the time the wafer is exposed to acetylene during the CVD process. After growing the CNT pillars to the desired length, the wafer containing them was placed upside-down on a stage above a reservoir containing the SU-8 resin (Microchem SU-8 2000.1). The stage was lowered until the CNT pillars contacted the SU-8. The SU-8 soaked the CNT pillars for 2 minutes, followed by the regular SU-8 curing process. The regularity of the contraction and the verticality obtained using this process are shown in Figure 3.24. As seen in Figure 3.24.c), a crown (~5-7 μm tall) is formed at the top of the pillar due to the contraction of the CNTs during wetting.

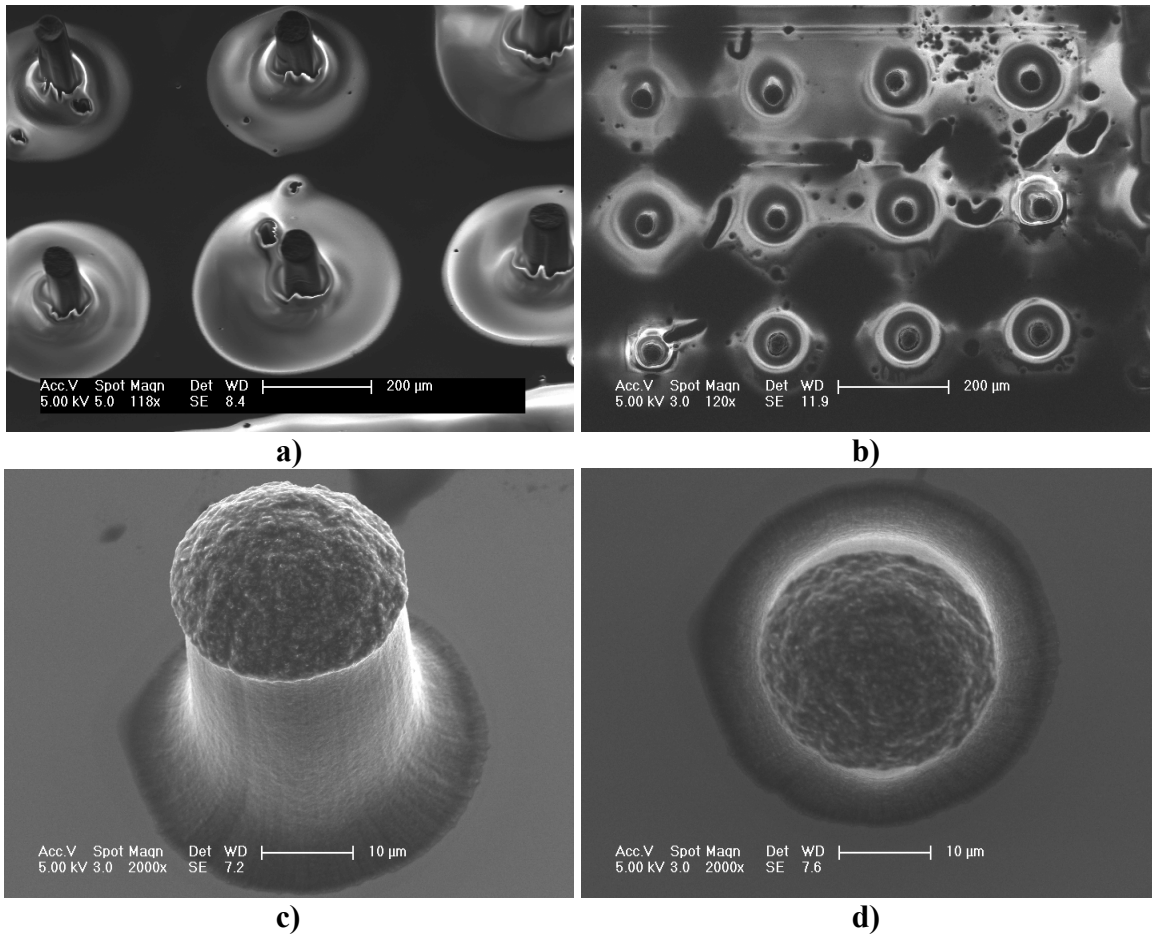

Figure 3.24: SEMs of a) CNT/SU-8 nanocomposite pillars with relatively well controlled contraction; b) top view of the same pillars; c) regularly contracted CNT/SU-8 pillar (note the crown formed during contraction); d) top view of the same pillar, showing the regular contraction and the verticality of the pillar after wetting.

As seen in Figure 3.24.a) and Figure 3.24.b), not all the cylindrical pillars are regularly contracted and perfectly vertical, both conditions being extremely important for compression testing. Therefore a careful selection of the pillars was necessary for compression testing. Scanning Electron Microscopy was used to identify the best pillars in terms of verticality and regular contraction, and also to measure the dimensions of each individual pillar (height and surface area at the top of the pillar). Only those selected pillars were subjected to the compression test.

3.4.1.2 Berkovich and Spherical Indentation of Films

Berkovich (pyramidal) and spherical indentations were applied to films made of two different pure epoxies and CNT/polymer nanocomposites to obtain the first reported mechanical characterization of nanocomposites based on such measurements. Two different epoxies (Buehler EpoThin and Microchem SU-8) and the two nanocomposites based on these epoxies were tested. The two main goals of these tests were to have a reference of the mechanical properties of the polymer and the nanocomposites and also to assess the accuracy of the compression test in capturing the mechanical properties of the pillars. Nanoindentation tests were performed using a Nanotest 600 nanomechanical testing system (Micro Materials, UK) [131], shown in Figure 3.25, in the Nanomechanical Technology Laboratory at MIT's Department of Material Science and Engineering.

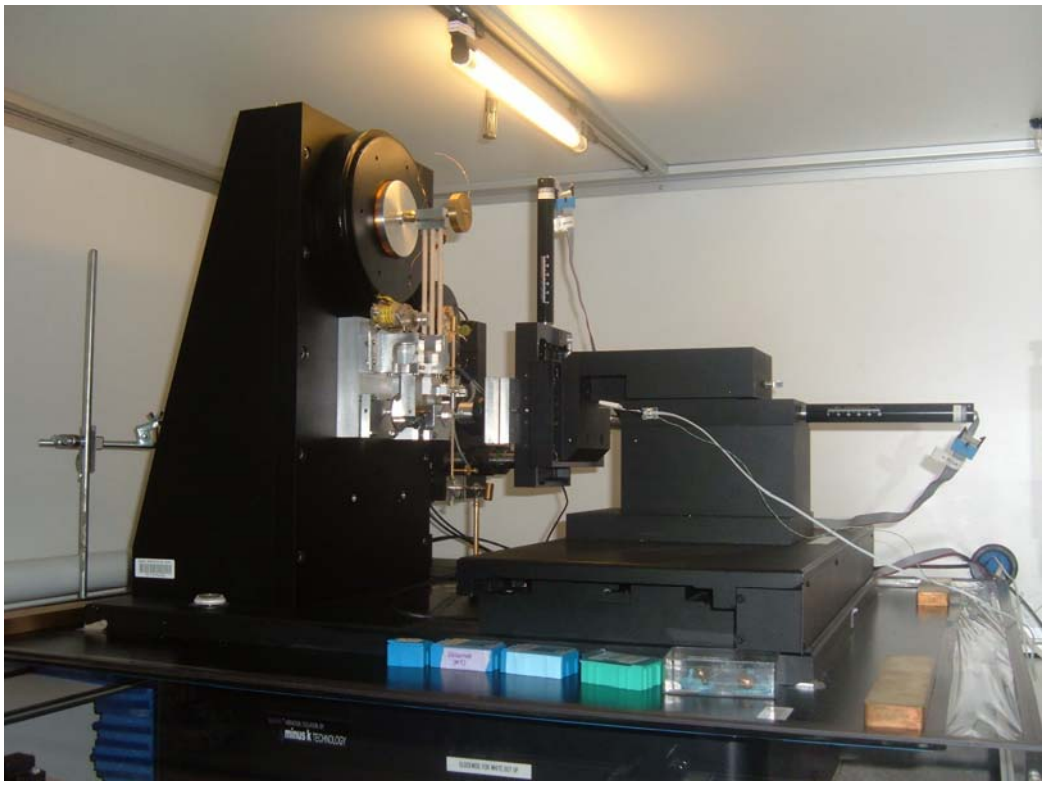

Figure 3.25: Micro Materials Nanotest micro- and nanoindenter.

The Micro Materials nanoindenter's design is based on the functioning of a pendulum, as shown in Figure 3.26 (adapted from [130]). Load is applied by means of a coil and magnet located at the top of the pendulum, which is supported on a frictionless spring flexure. The resultant displacement (the depth of the probe penetrating into the sample's surface) is monitored with a capacitive transducer. A load-displacement curve is recorded in real time during the test. The nanoindenter monitors and records the load and displacement of the indenter with a force resolution of ~100 nN and displacement resolution of about 0.1 nm [132]. The Nanotest 600 contains two different pendulums, named Nanoindenter and Microindenter, designed to increase the load range of the equipment. Due to its design based on a pendulum, the load-range of this machine varies from 10 μN to 500 mN (using the Nanoindenter pendulum) and from 500 mN to 20 N

(using the Microindenter pendulum). The nanoindenter's wide range of forces allowed testing of pillars with different sizes, which is the primary reason why the equipment was selected for this research.

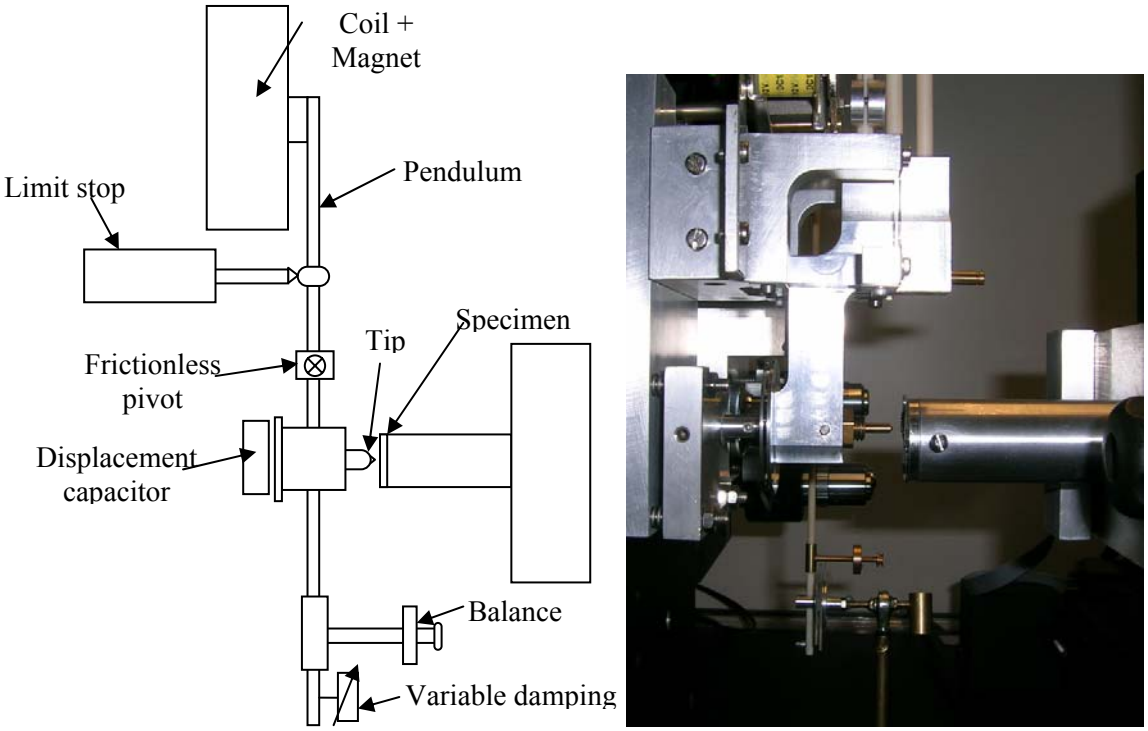

a) **b)**

Figure 3.26: a) Schematic of the Micro Materials Nanotest design; b) Close-up view of the indenter, where it is possible to identify the most important parts of the of the pendulum system.

Nanoindentation static mechanical analysis tests using two different indentation probes (Berkovich and spherical) were performed inside the nanoindenter's thermally insulated environmental chamber at a room temperature of 25 ± 0.5 ºC and relative humidity of 45 ± 2%. The tests on films made of both pure EpoThin and SU-8, and also on nanocomposites containing these two epoxies as matrix were completed to study the four materials' static properties at the nanoscale and to quantify the effective

reinforcement of the CNT forest. The epoxy resin mechanical properties are highly dependent on the rate of the tests[133]. Therefore, in order to be able to compare the results obtained for the unreinforced matrix epoxies and the nanocomposites, the test's parameters were held constant for each type of indentation test. Initial tests were used to determine acceptable test parameters: maximum load and depth, and more importantly the load rate, and the time hold at the maximum load to avoid creep effects in the results.

The different specimens' hardness and elastic modulus were calculated from the recorded load–displacement curves. A typical indentation experiment consists of four subsequent steps: approaching the surface; loading to peak load; holding the indenter at peak load for 60 to 120 s depending on the material of the specimen; finally unloading completely. The hold step is necessary to avoid the influence of the polymer's creep on the unloading characteristics since the unloading curve was used to obtain the elastic modulus of the different materials tested. A more detailed explanation of the procedure and the calculations made is provided in the paragraph describing the theoretical model used to determine the elastic modulus. A complete description of the nanoindentation experimental techniques is shown in the works by Bhushan and Li [125]-[126]. The indentation impressions were imaged using a scanning electron microscope (FEI/Philips XL30 FEG SEM).

Nanoindentation hardness is defined as the indentation load divided by the projected contact area of the indentation. It is the mean pressure that a material will support under load. From the load–displacement curve, hardness can be obtained at the peak load as:

$$H = \frac{P_{\max}}{A} \tag{3.1}$$

where A is the projected contact area. For the two different indenter probes used in this study, the geometry is known and the projected contact area is a function of contact depth, which is measured by the nanoindenter in-situ during indentation. Therefore, the projected area, A, can be calculated directly from the indentation displacement.

The Berkovich indenter is a 3-side pyramidal diamond probe with a face angle of 65.3º, as shown in Figure 3.27.

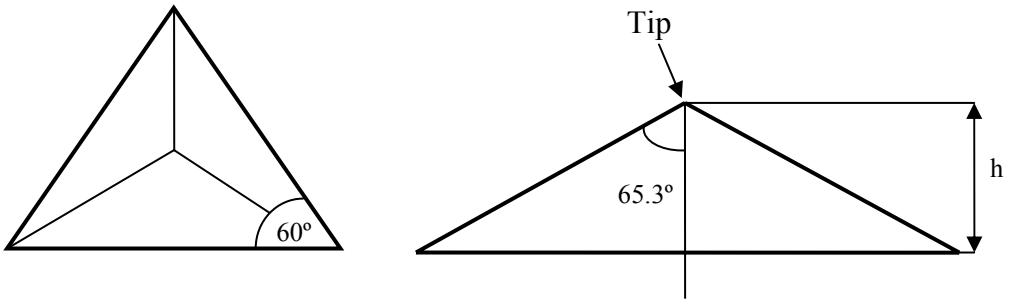

Figure 3.27: a) Top and b) side views of the geometry of the Berkovich indenter.

The projected area for an ideal Berkovich indenter is presented in equation (3.2).

$$A = 3\sqrt{3}h_p^2 \tan^2\theta \tag{3.2}$$

where h_p is the depth of penetration measured from the tip of the indenter, and θ is the face angle (65.3º, as mentioned previously). Introducing this value into equation (3.2), the projected area for a Berkovich indenter is:

$$A = 24.5 \cdot h_p^2 \tag{3.3}$$

Therefore, for the Berkovich indenter the projected area is a quadratic function of the depth of penetration.

The projected area for the spherical indenter is simplified to a circle of radius a, as shown in Figure 3.28.

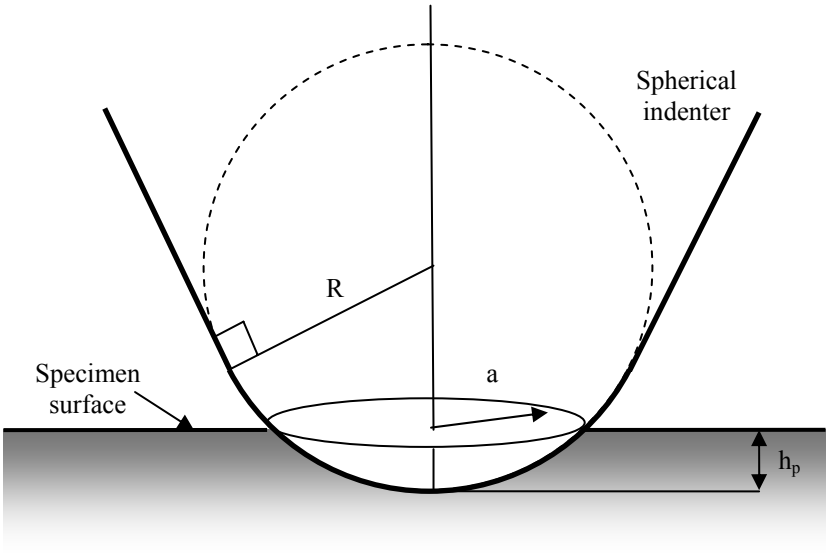

Figure 3.28: Schematic of the geometry of spherical indentation.

The radius of the circle that defines the contact area, a, can be calculated as:

$$a = \sqrt{2Rh_p - h_p^2} \tag{3.4}$$

where R is the radius of the spherical tip (750 μm for the steel tip used in the tests for this research), and h_p is the depth of indentation. The projected area for a spherical indenter, therefore, follows the equation:

$$A = 2\pi Rh_p - \pi h_p^2 \tag{3.5}$$

For both types of indenters there is a geometry correction factor, ε, which corrects the depth measured by the nanoindenter. For both nanoindenters this geometry correction factor is equal to 0.75 (ε = 0.75) [127].

The elastic modulus was calculated using the Oliver–Pharr data analysis procedure [127] beginning by fitting the unloading curve to a power-law relation. The unloading stiffness can be obtained from the slope of the initial portion of the unloading curve, $S=dP/dh_p$, as shown in Figure 3.29.

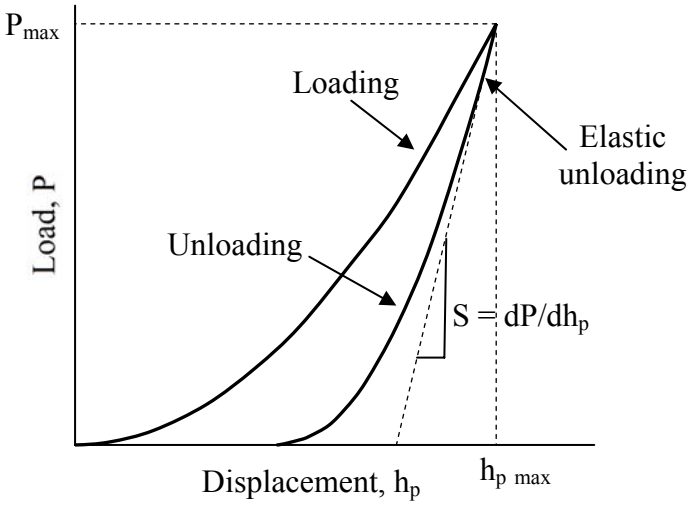

Figure 3.29: Illustration showing the analysis for unloading. Adapted from [126].

Based on relationships developed by Sneddon [128] for the indentation of an elastic half space by any punch that can be described as a solid of revolution of a smooth function, a geometry independent relation involving contact stiffness, S, contact area, A, and reduced elastic modulus of the indenter and the test specimen, E_r, has been derived:

$$S = \frac{dP}{dh_p} = \frac{2\beta}{\sqrt{\pi}} E_r \sqrt{A} \tag{3.6}$$

where β is a constant which depends on the geometry of the indenter (β = 1.034 for an ideal Berkovich indenter) [127], A is the projected area, (which is a function of the depth of contact for both Berkovich and spherical indenters), and E_r is the reduced elastic modulus which accounts for the fact that elastic deformation occurs in both the sample and the indenter, and is given by the expression:

$$\frac{1}{E_r} = \frac{1-\nu^2}{E} + \frac{1-\nu_i^2}{E_i} \tag{3.7}$$

where E and ν are the elastic modulus and Poisson's ratio for the specimen/film, and E_i and ν_i are the same quantities for the indenter. For diamond, E_i=1141 GPa and ν_i=0.07 [125]. For the steel used in the spherical indenter, E_i=210 GPa and ν_i=0.25 [139]. As the nanoindenter measures the contact force and the depth, the only unknown in the original equation is the material's elastic modulus, E, which can be derived from experimental results giving S and A by solving the expression:

$$E = \frac{1-\nu^2}{\frac{1}{E_r} - \frac{1-\nu_i^2}{E_i}} = \frac{1-\nu^2}{\frac{2\beta}{S\sqrt{\pi}}\sqrt{A} - \frac{1-\nu_i^2}{E_i}} \tag{3.8}$$

The software provided with the Micro Materials Nanotest 600 includes an analysis module that implements the curve-fitting calculations using the load-depth curves obtained from the nanoindentation tests.

Berkovich and spherical tests were performed on the SU-8 and CNT/SU-8 films using the Nanoindenter pendulum. As discussed previously, initial tests were used to determine acceptable test conditions. Once the parameters were determined for the two indenters, a series of 4 indents were performed on 3 different specimens for each material and tip (Berkovich and spherical). A compliance calibration of the machine was performed before starting the nanoindentation tests. This compliance calibration is necessary to account for the effect of the stiffness of the equipment on the results. Results for these tests are presented in section 3.4.2.2.

The Nanoindenter pendulum was also used initially for the EpoThin and CNT/EpoThin films, but after several extremely scattered results it was evident that

deeper indents were needed to determine accurately the mechanical properties of these materials and therefore the Microindenter pendulum (with a higher load and displacement range) was used instead. For this type of epoxy, again, acceptable parameters were determined with initial indentations. An array of 4 indents was performed on 3 different specimens for each material (pure EpoThin and CNT/EpoThin nanocomposite) and tip, preceded by a compliance calibration. Results for these tests are presented in section 3.4.2.1.

3.4.1.3 Compression Tests of Pure Polymer and CNT/Polymer Pillars

Compression tests were applied to pillars of CNT/EpoThin nanocomposite, pure SU-8, and CNT/SU-8 nanocomposite (as mentioned in section 3.4.1.1, it was not possible to fabricate pure EpoThin pillars), using the same equipment previously used for Berkovich and spherical nanoindentation. The compression test consisted of the same four steps previously described for Berkovich and spherical nanoindentation: approaching the surface; loading to peak load; holding the indenter at peak load for 60 to 120 s depending on the material of the specimen (to minimize the effect of creep); and finally unloading completely.

As mentioned in section 3.4.1.1, SEM had been used to determine the dimensions for each pillar tested (surface area and height), so that the load-displacement curves obtained during the nanocompression tests could be transformed into stress-strain curves to determine the Young's modulus. The Young's modulus obtained using this method was compared with the results obtained by modifying Oliver-Pharr's flat punch theory for the unloading part of the test to determine consistency between testing types

(nanoindentation vs. nanocompression) for the nanocomposites tested. The compression test using the Micro Materials nanoindenter is taken to be equivalent to a flat punch nanoindentation. The unloading load-displacement curves were analyzed using the Oliver-Pharr theory with a new value for the projected area: For a compression test, the area in contact with the pillar, called projected area in nanoindentation, is the total surface area of the pillar, as shown in Figure 3.30.

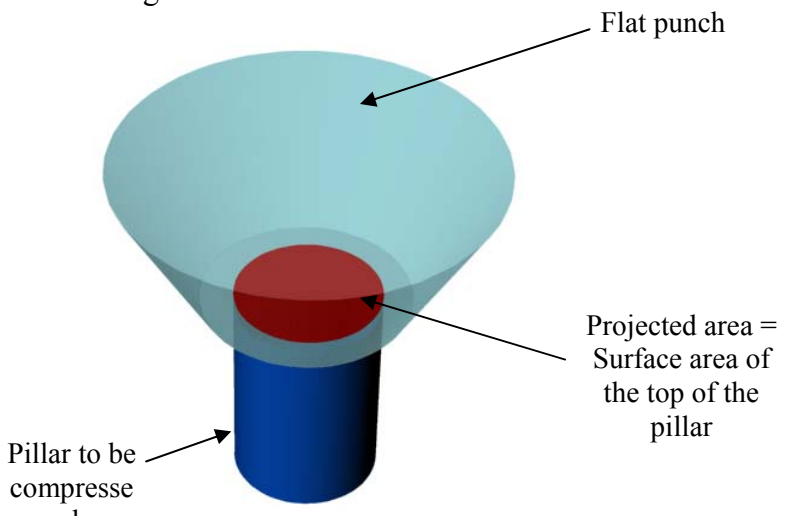

Figure 3.30: Schematic of the geometry of compression test using a flat punch nanoindenter. The contact area between the flat punch and the pillar is the surface area of the pillar's top surface.

For the compression tests on CNT/EpoThin pillars (around 250 μm in diameter, 1-mm long), a 2.5 mm-diameter steel spherical punch mounted on the Microindenter pendulum was used. The sphere was large enough, compared to the diameter of the pillars, to approximate the contact area to that of a flat punch. Compression tests were applied to 10 different pillars using the Micro Materials nanoindenter. Results for these tests are presented in section 3.4.2.1.

For the SU-8 and CNT/SU-8 nanocomposite pillars, a flat punch was fabricated to perform compression tests to improve accuracy in testing the small (from 30 to 40 μm in

diameter, around 80 μm in height) specimens. A conical diamond tip was flattened using a Focused Ion Beam (FIB) creating a flat punch with a diameter of 80 μm. This flat punch was mounted on the Microindenter pendulum to complete the compression tests. Thirty compression tests were applied on pure SU-8 pillars, and 25 compression tests were performed on CNT/SU-8 nanocomposite pillars. Results for these tests are presented in section 3.4.2.2.

3.4.2 Results and Discussion

The results from the nanoindentation and compression tests have been divided into two sections, corresponding to the two different epoxy matrices used for this study, Buehler's EpoThin and Microchem's SU-8.

3.4.2.1 Results Using EpoThin as Matrix

As mentioned in section 3.4.1.2, films of pure EpoThin and also films containing large CNT/EpoThin pillars were subjected to nanoindentation tests with two different tips, Berkovich and spherical. The initial indentations were used to determine the acceptable test parameters for each type of test and indenter.

The parameters for the films containing EpoThin using the Berkovich indenter mounted on the Microindenter pendulum were determined to be:

- Maximum force = 5000 mN
- Maximum displacement (depth) = 7 μm
- Force loading rate = 1 mN/s

- Force unloading rate = 1 mN/s
- Holding time = 120 s

Three series of 4 indents were performed on films of both pure EpoThin and CNT/EpoThin nanocomposites. A typical Berkovich indent on the microtomed surface of CNT-reinforced EpoThin film is shown in Figure 3.31.

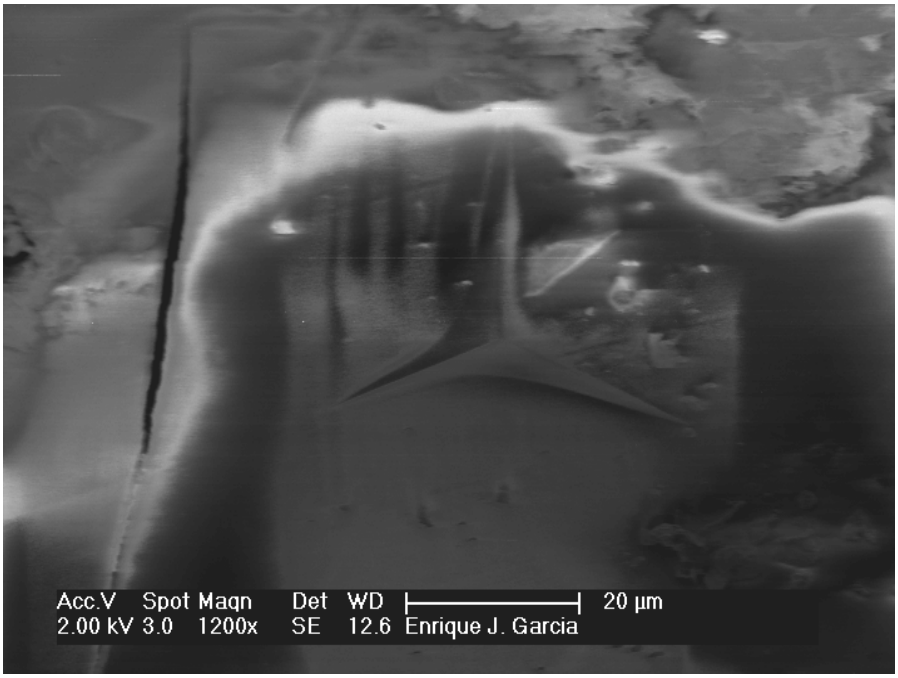

Figure 3.31: Berkovich indent on the surface of a CNT/EpoThin film.

The results were studied using the analysis module integrated in the Micro Materials' software. The first step of the analysis is to establish the projected area. For a Berkovich tip the expression for the projected area is a quadratic function of the penetration depth, as seen in equation (3.3). A graphical representation of this relationship is shown in Figure 3.32.

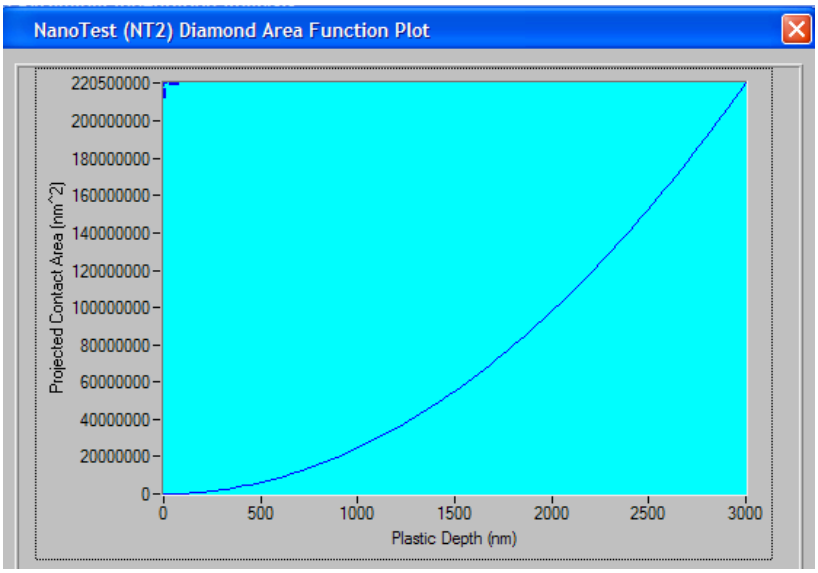

Figure 3.32: Projected contact area as a function of the penetration depth for a Berkovich indenter used by Micro Materials' analysis software.

For the analysis of the results, the geometry correction factor, ε, was set to 0.75 [127], and the compliance of the machine was calibrated before starting the tests and introduced as a parameter in the analysis module. The power-law fitting was calculated for the section of the unloading curve going from 95% to 40% of the maximum load, parameters usually used in previously reported experimental work on nanoindentation[132]. All these settings are highlighted in Figure 3.33, and were maintained for all the Berkovich and spherical indentation tests.

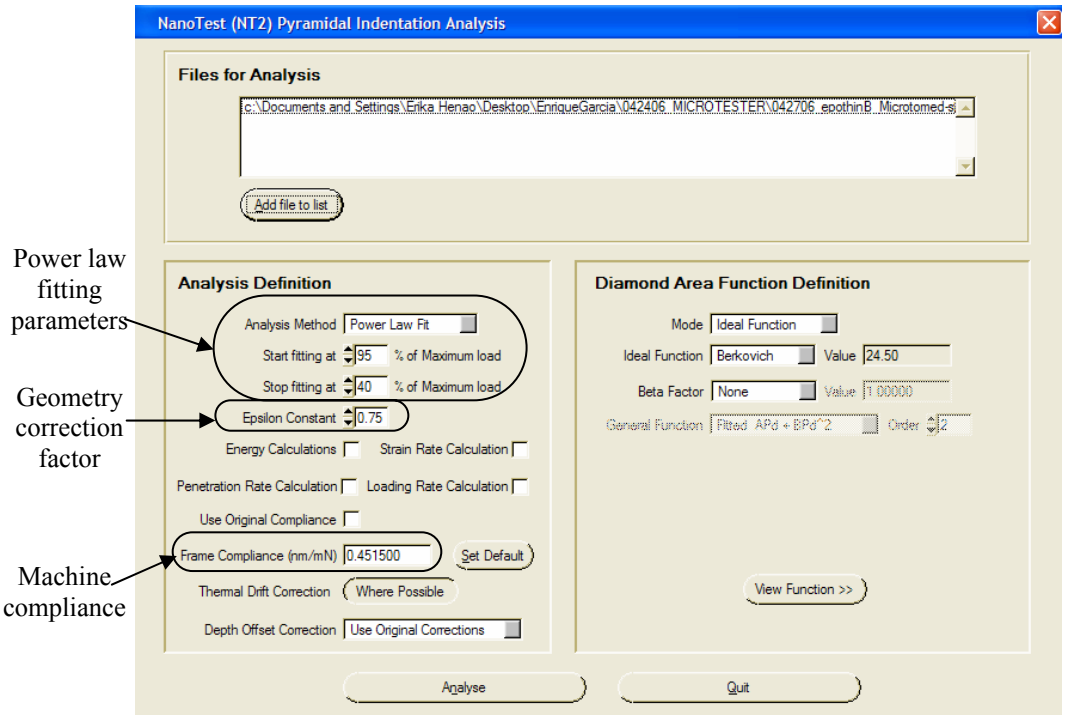

Figure 3.33: Indentation analysis parameters for the Micro Materials' analysis software.

A typical power-law fitting analysis for a Berkovich indentation performed by the Micro Materials software for a test on a film of pure EpoThin is shown in Figure 3.34. Note creep in the response at the load hold point.

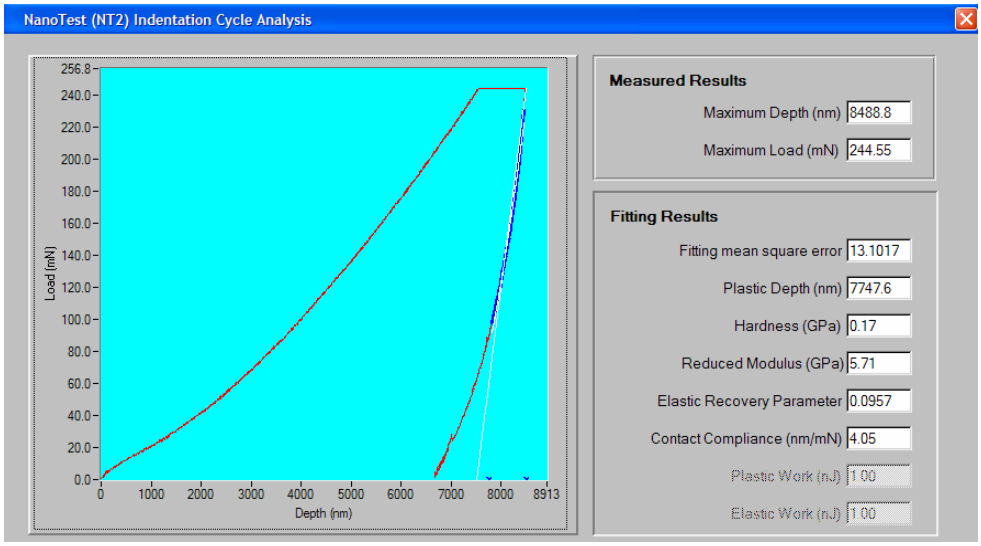

Figure 3.34: Typical power-law fitting analysis parameters for the Micro Materials' analysis software. In this case, fitting for a Berkovich indentation on the surface of a pure EpoThin film.

Two representative load-depth curves for both unreinforced EpoThin and CNT/EpoThin nanocomposite are shown in Figure 3.35. Two plateaus appear in the curves for both materials. The plateau at the maximum load (marked as "Creep plateau") is due to the dwell period (or holding time) of 120 seconds used to avoid the creep component during unloading. The second plateau (marked as "Drift plateau" in the figure) is due to a dwell period of 30 seconds at 20% of the maximum load during unloading. This second dwell period is used to correct possible drifts due to thermal variations during the test. The results for Berkovich nanoindentation tests on pure EpoThin and CNT/EpoThin nanocomposite films are summarized in Table 3.3.

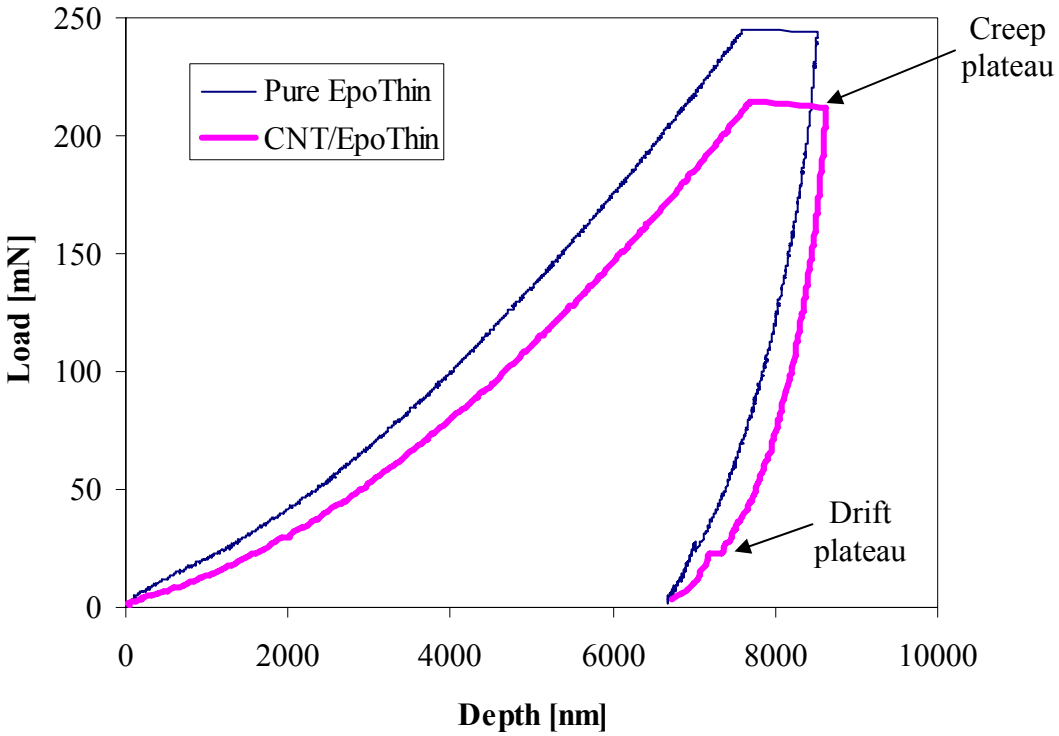

Figure 3.35: Representative Load-Depth curves for Berkovich nanoindentation of unreinforced (thin blue line) and CNT-reinforced EpoThin (thick magenta line) films.

Table 3.3: Comparison of mechanical properties (Young's modulus and hardness) for unreinforced EpoThin and CNT/EpoThin nanocomposite films obtained from Berkovich nanoindentation tests (12 tests).

	Unreinforced EpoThin	CNT/EpoThin Nanocomposite	Change
Young's modulus [GPa]	5.471 ± 0.073	6.741 ± 0.266	22.5%
Hardness [GPa]	0.169 ± 0.002	0.132 ± 0.007	-21.0%

From the results it is possible to note that the hardness of the composite material is 21% lower than the hardness of the unreinforced material. This reduction in hardness can plausibly be explained by the combination of two factors: First, as seen in equation (3.1), the hardness is calculated from the maximum load. Therefore, this property is determined using the loading region of the load-depth curve, which is rate-dependent and presents hysteresis. Second, the inhomogeneity of the nanocomposite may also contribute to the reduction of the nanocomposite hardness.

The Young's modulus of the unreinforced polymer, on the contrary, is calculated from the unloading region of the load-depth curve. The results show that the Young modulus is increased by 22.5% with the addition of 0.9% of volume fraction of well-aligned CVD-grown CNTs. The volume fraction calculated considering a spacing between the MWCNT of 80 nm, and the CNTs as solid tubes with inner diameter of 5 nm and outer diameter of 10 nm, as shown in Figure 3.2. Also it was assumed that the space inside the inner tube of the MWCNTs was filled by the polymer matrix (no voids). It is interesting to contrast these results with a simplified model of the nanocomposite. Assuming perfect alignment of the CNTs, perfect wetting of the CNTs by the epoxy, perfect bonding in the interface between the CNTs and the epoxy, and perfect bonding between the tubes of a MWCNT, a simplified rule of mixtures can be expressed as:

$$E_{nanocomp} = E_{CNT}V_{CNT} + E_{matrix}(1 - V_{CNT}) \quad (3.7)$$

where $E_{nanocomp}$, E_{CNT}, and E_{matrix} are, respectively, the Young's modulus of the nanocomposite, the modulus of pure CNTs (assumed to be 1 TPa for this simplified calculations), and the modulus of the unreinforced EpoThin (5.471 GPa as shown in Table 3.3), and V_{CNT} is the volume fraction of CNTs (~0.9%) . With all the assumptions made, the Young's modulus of the nanocomposite is calculated as 14.62 GPa (163% improvement from the unreinforced polymer, 2.2 times higher than the CNT-reinforcement results obtained experimentally using the Berkovich indentation technique). A calculation for modulus considering that the void inside the MWCNT is not filled by the polymer differs 0.01% from the result calculated without considering the voids.

The spherical nanoindentation tests on unreinforced and CNT-reinforced films began by finding acceptable test parameters. The parameters for spherical nanoindentation test for these two materials were:

- Maximum force = 5000 mN
- Maximum displacement (depth) = 20 μm
- Force loading rate = 10 mN/s
- Force unloading rate = 10 mN/s
- Holding time = 120 s

As in the previous set of tests, a series of 4 indents were performed on 3 different films for both pure EpoThin and CNT/EpoThin nanocomposites and the results were studied using the analysis module integrated in the Micro Materials' software.

The spherical indentation tests were performed using the same procedure described previously for the Berkovich nanoindentation. First, the quadratic expression that related the contact area and the penetration depth, derived in equation (3.5), was implemented in the analysis module. Due to the size of the spherical indenter used for these tests (1.5 mm in diameter) the linear term dominates the quadratic one, as shown in Figure 3.36.

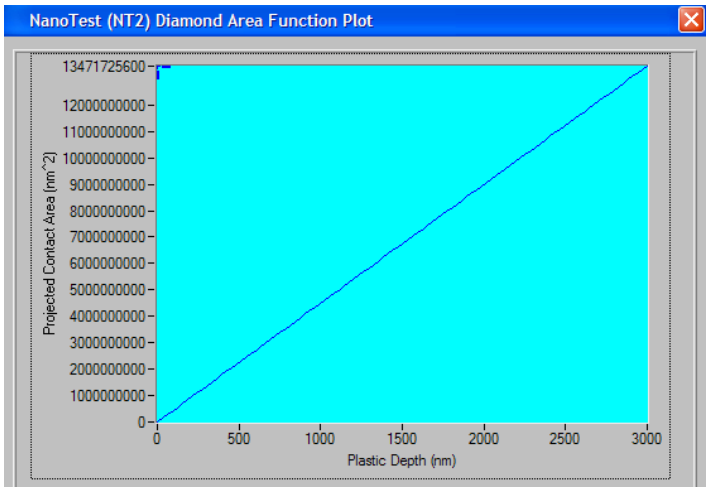

Figure 3.36: Projected contact area as a function of the penetration depth for a spherical indenter used by Micro Materials' analysis software. The linear term found in equation (3.5) dominates the quadratic term.

From that point on, the analysis was equivalent to the one described previously for the Berkovich indenter. Two representative load-depth curves for pure EpoThin and CNT/EpoThin curves are shown in Figure 3.37. The results obtained for this set of tests are summarized in Table 3.4.

Table 3.4: Comparison of mechanical properties (Young's modulus and hardness) for unreinforced EpoThin and CNT/EpoThin nanocomposite films obtained from spherical nanoindentation tests (12 tests).

	Unreinforced EpoThin	CNT/EpoThin Nanocomposite	Improvement
Young's modulus [GPa]	3.544 ± 0.165	4.446 ± 0.992	25.4%
Hardness [GPa]	0.127 ± 0.006	0.107 ± 0.022	-15.5%

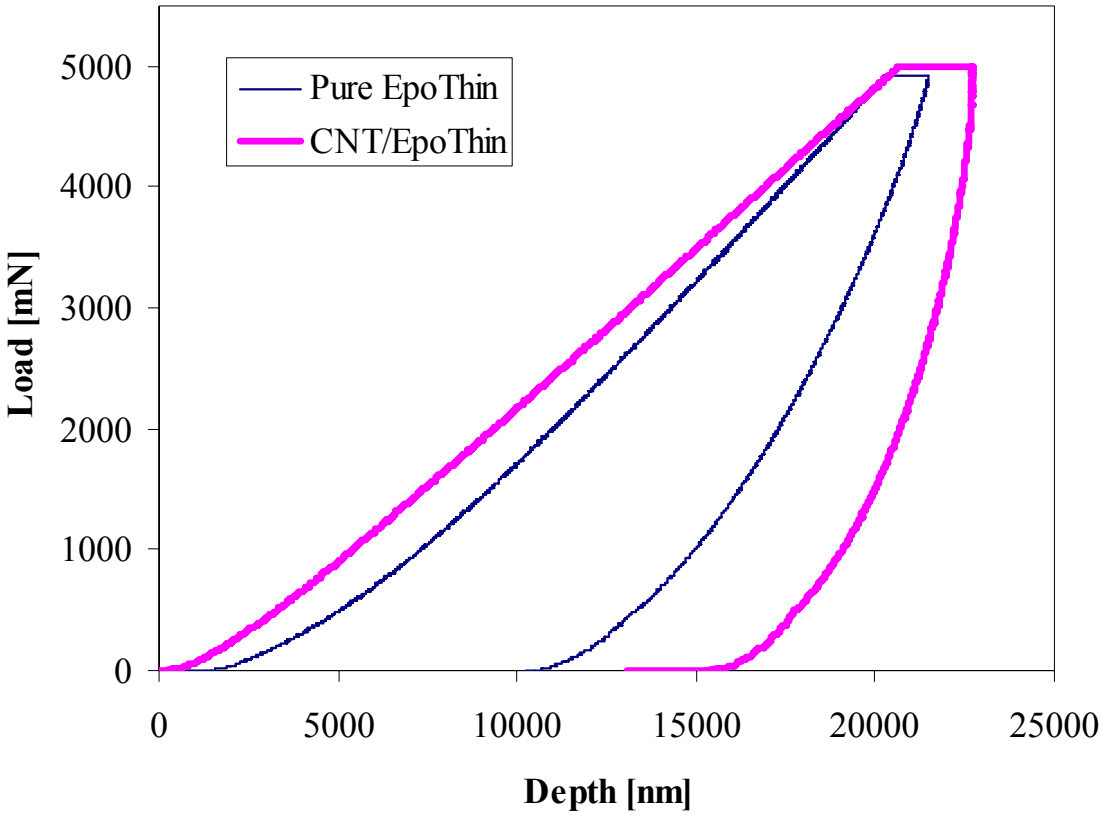

Figure 3.37: Representative Load-Depth curves for spherical nanoindentation of unreinforced (thin blue line) and CNT-reinforced EpoThin (thick magenta line) films.

The first thing to note after comparing the results obtained using the spherical indenter with the ones obtained from the Berkovich indentations on pure EpoThin is that the Young's modulus and hardness obtained using the spherical indentation are notably

smaller (54% smaller for the Young's modulus and 33% smaller for the hardness) than those obtained previously. As mentioned in section 3.4.1.2, the mechanical properties of the epoxy are highly dependent on the rate of the tests [133]. The rate used in the Berkovich nanoindentation tests (1 mN/s) is different from the rate used in the spherical nanoindentation tests (10 mN/s) which may explain the difference. The comparison between the mechanical properties of the unreinforced and CNT-reinforced matrix from the spherical indentation, however, is consistent with the trends observed for the Berkovich indentations: the hardness of the material is decreased by 15.5%, whereas the elastic modulus is increased by 25%. The idealized model of the reinforcement with the spherical result for $E_{EpoThin}$ (3.544 GPa) gives a 258% improvement in the Young's modulus for the nanocomposite (going from the epoxy's initial 3.544 GPa to 12.7 GPa), almost 3 times higher than the actual modulus increase. It is also important to note that the results using the spherical indentation are more scattered than the ones obtained using the Berkovich indentation, especially for CNT/EpoThin nanocomposites (the standard deviation for the elastic modulus increases from 0.266 GPa to 0.992 GPa, and that for the hardness increases from 0.007 GPa to 0.022).

Finally, compression tests were applied on 10 CNT-reinforced EpoThin pillars (~250 μm in diameter and ~700-μm long after microtoming the top surface). The surface area and the height of the pillars were measured individually using a FEI/Philips XL30 FEG SEM. A 2.5-mm spherical steel punch mounted on the Microindenter pendulum was used to perform the compression tests. The punch was assumed to be flat considering the dimensions of the pillars (250 μm) and the small indentation depth (20 μm). The test

parameters are similar to the ones used for the Berkovich indentation tests (apart the maximum depth increasing from 7 to 20 μm):

- Maximum force = 5000 mN
- Maximum displacement (depth) = 20 μm
- Force loading rate = 10 mN/s
- Force unloading rate = 10 mN/s
- Holding time = 120 s

The Young's modulus of the nanocomposite pillars was calculated using two different techniques: First, it was derived from the Oliver-Pharr power-law fitting of the unloading; secondly, the elastic modulus was also calculated from the slope of the stress-strain curve (as seen in the work by Nix and Greer for Au pillars [134]).

As described in the experimental section, the pillars were created using the method shown in Figure 3.8. A representative pillar before and after the compression test is shown in Figure 3.38. As seen in Figure 3.38.d), the honeycomb, or cellular structure is flattened during the compression test.

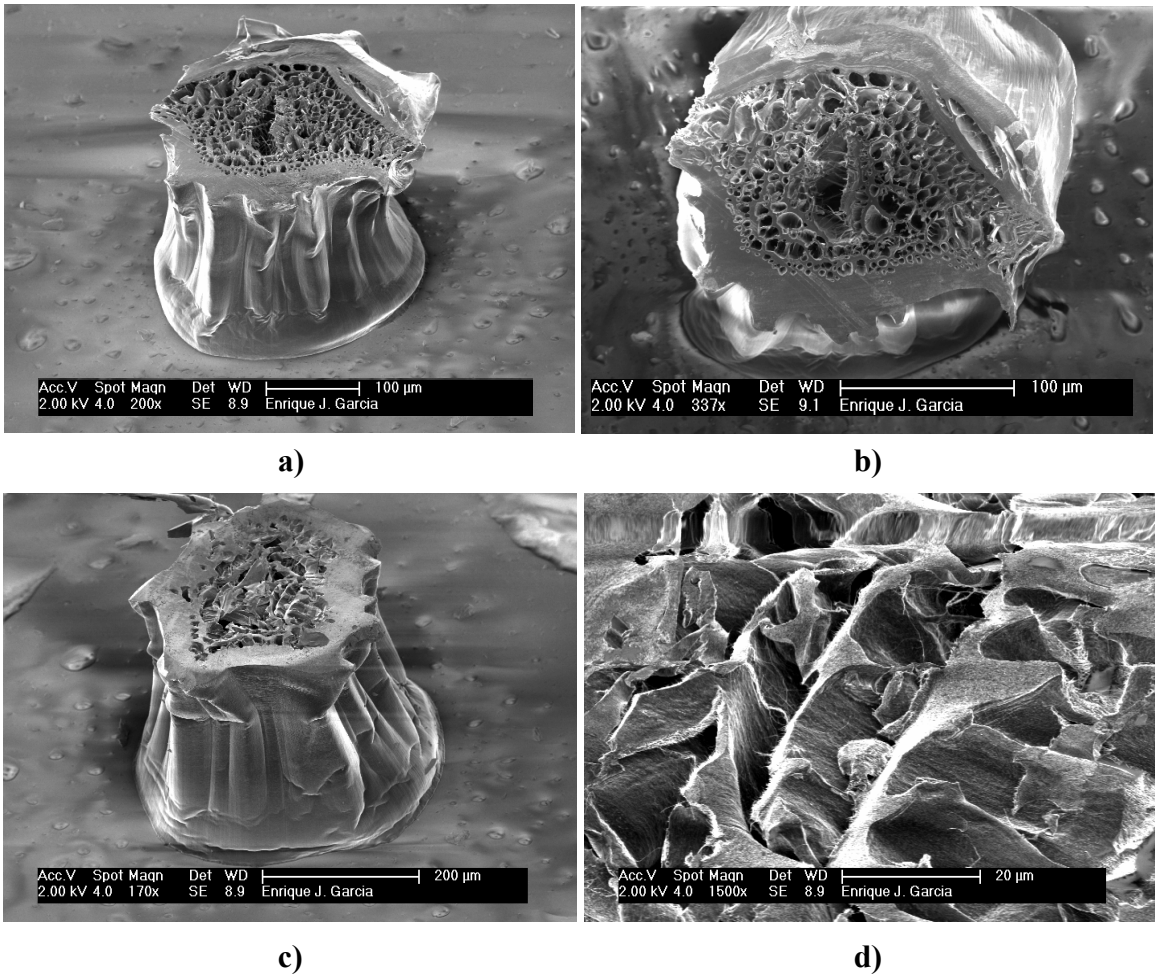

Figure 3.38: SEM images of a) microtomed CNT/EpoThin nanocomposite pillar; b) top view of the pillar, showing the cellular structure formed in the interior of the pillar during wetting; c) pillar after compression test (note that the cellular structure has been flattened out during the test); d) closer view of the flattened honeycomb structure.

The projected area (constant for a flat punch indentation) was calculated using SEM top view images of the pillars and Rhinoceros^{TM} commercial CAD/CAM software. Initially, the pillars were considered to be solid, and the surface area used in the calculations is shown in Figure 3.39.

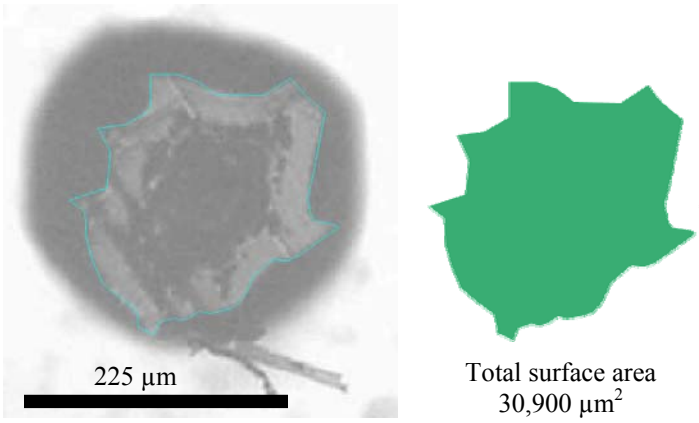

Figure 3.39: Illustration of process used to calculate the effective area of the nanocomposite pillars subjected to compression tests: a) SEM top view image of the microtomed pillar with the perimeter highlighted; b) total surface area of the pillar.

Preliminary calculations from the stress-strain curves showed that the Young's modulus of the CNT/EpoThin pillars was around 3.5 GPa (approximately 50% lower than from the Berkovich results). As shown in Figure 3.38, a closer analysis of the SEM pictures showed that the wetting of the CNTs by the EpoThin had concentrated the CNTs around the perimeter, and created a thin honeycomb structure (walls ~10 µm thick) in the interior (for most pillars), thus reducing the effective surface area for the compression test (see Figure 3.22). The new surface was calculated using the same procedure, as shown in Figure 3.40 for a pillar that had all the CNTs contracted around the perimeter (no honeycomb structure in the interior.

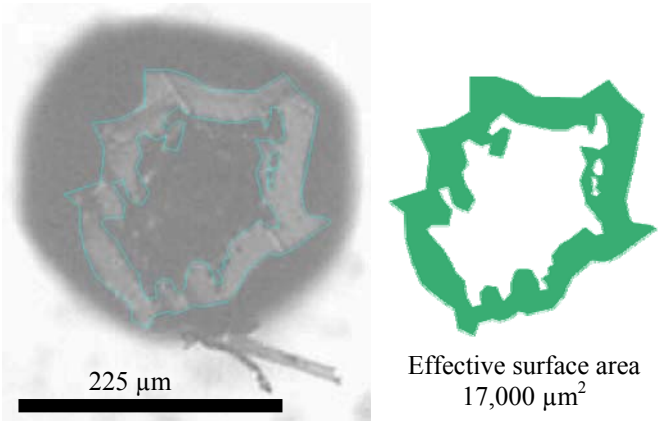

Figure 3.40: Illustration of process used to calculate the effective area of the nanocomposite pillars subjected to compression tests: a) SEM top view image of the microtomed pillar with the effective perimeter highlighted; b) effective surface area of the pillar.

The contraction of the CNTs around the outer wall of the pillar increases the volume fraction of the nanocomposite. The original surface (before wetting) of the 225-µm circular pillar was 39760 μm^2, whereas the new effective surface area calculated is 17,000 μm^2. Therefore, the volume fraction changes from the original 0.9% to 2.1%.

A comparison between the stress-strain curves for one of the pillars derived from the original load-depth curve obtained from the nanoindenter using the two different areas is shown in Figure 3.41. The elastic region used to calculate the Young's modulus of the nanocomposite pillar is highlighted.

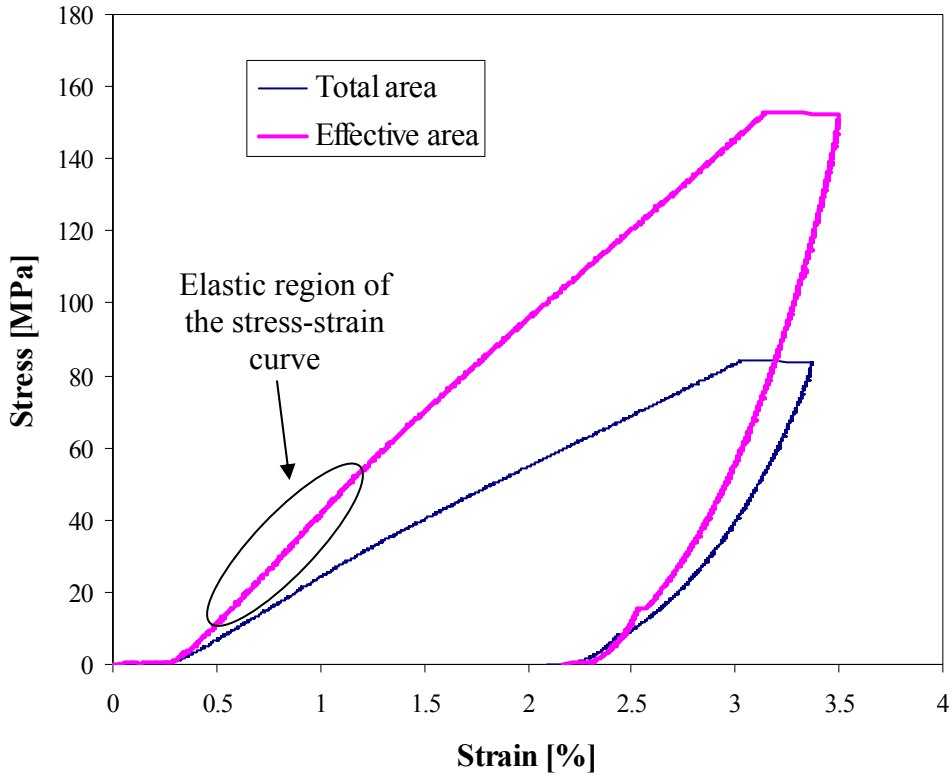

Figure 3.41: Representative stress-strain curve for the CNT-reinforced EpoThin pillars under compression using the total surface inside the perimeter (thin blue line) and the effective surface area (thick magenta line). The elastic region used to calculate the elastic modulus is highlighted.

The results obtained for the Young's modulus analyzing the loading and unloading curves are presented in Table 3.5 using the effective area.

Table 3.5: Comparison of the Young's modulus of CNT-reinforced EpoThin pillars obtained from Oliver-Pharr's curve fitting for the unloading and from the analysis of the stress-strain curve during loading (10 tests).

	Unloading (Oliver-Pharr's theory)	Loading (from the stress-strain curve)	Underestimation of the unloading analysis
Young's modulus [GPa]	6.026 ± 0.258	6.4 ± 0.260	5.4%

The analysis of the unloading curve using Oliver-Pharr's theory underestimates the Young's modulus 5.4% with respect to the results from loading, which indicates overall good agreement. The load and unload rates for this set of tests was the same used for the spherical indentation tests previously presented. Comparing the results obtained from compression of CNT/EpoThin pillars (6.024 GPa from the unloading curve) and from spherical indentation of unreinforced EpoThin films (3.544 GPa), the effective reinforcement for the pillars is 70%, much higher than the previously obtained 25%. The change in volume fraction is responsible for this increase in the reinforcement: As discussed previously, the formation of the cells shown in Figure 3.40, the volume fraction of CNTs changes from the original 0.9% to 2.1%. It is possible to compare these results with the idealized model based on the rule of mixtures presented in equation (3.7). When the Young's modulus of the CNTs is considered to be 1 TPa, the modulus for the EpoThin is taken from the spherical indentation (3.544 GPa) and the volume fraction is set to 2.1%, the idealized Young's modulus of the CNT/EpoThin nanocomposite is 23.47 GPa (562% improvement with respect to unreinforced EpoThin). This result is 3.67 times the reinforcement obtained from the compression test. The results obtained from the Berkovich indentation showed an experimental/ideal ratio of 2.2 for the CNT-reinforced films (better agreement with the rule-of-mixtures model). Possible explanations for the disagreement from the ideal model in the case of the pillar are formation of CNT aggregates, loss of alignment due to the irregular contraction, non-ideal wetting, buckling or non-ideal compression of the CNT/EpoThin nanocomposites, and/or lack of interaction between the tubes of the MWCNTs.

As demonstrated with the tests described in this section, EpoThin films can be reinforced up to 25% using less than 1% volume fraction and 70% with 2.1% of well-aligned CNTs. This is far from the theoretical improvement derived from the idealized rule of mixtures, which means that the assumptions made by this simplified model (Young's modulus of 1 TPa for the CVD grown CNTs, perfect alignment, perfect wetting, and perfect bonding, etc.) are likely not valid for the actual nanocomposite. However, it is interesting to note that from results reported in studies based on the dispersion of randomly oriented CNTs in the matrix, 3% and 5% of CNTs in volume fraction are respectively required to obtain the same level of reinforcement [124].

3.4.2.2 Results Using SU-8 as Matrix

Microchem SU-8 2025 and low viscosity 2000.1 (1.25 cPs) were used to fabricate the second set of unreinforced (SU-8 2025) and CNT-reinforced (SU-8 2000.1) films and pillars using the microfabrication techniques described in section 3.4.1.1. The surface of the unreinforced SU-8 films and pillars after curing is relatively even, and therefore these specimens do not require microtoming before indentation. The CNT/SU-8 pillars are fully wet, regular in shape, and do not present the voids appeared in the pillars wet with EpoThin. The Microindenter pendulum of the Micro Materials Nanotest was used for nanoindentation tests using a Berkovich indenter. The nanoindentation tests were performed on 40-μm thick films made of unreinforced SU-8 and CNT/SU-8 nanocomposite. After calibrating the machine compliance, the initial indentations were used to determine acceptable test parameters for each type of test and indenter. Twenty different preliminary tests were performed on CNT-reinforced films changing the test

parameters and in every one of these tests, there was a creep component in the initial part of the unloading phase, as shown in Figure 3.42. The Oliver-Pharr's analysis is not possible when creep is present (the power-law fitting is distorted by the creep recovery), and therefore, the results for the CNT-reinforced SU-8 films were discarded. A likely explanation for the presence of creep in these tests is that the SU-8 matrix of the nanocomposite was not fully cured when the tests were applied. The SU-8 is a UV curing epoxy. It is plausible that the (black) CNTs embedded into the SU-8 blocked the UV light, preventing the initiation of the curing process.

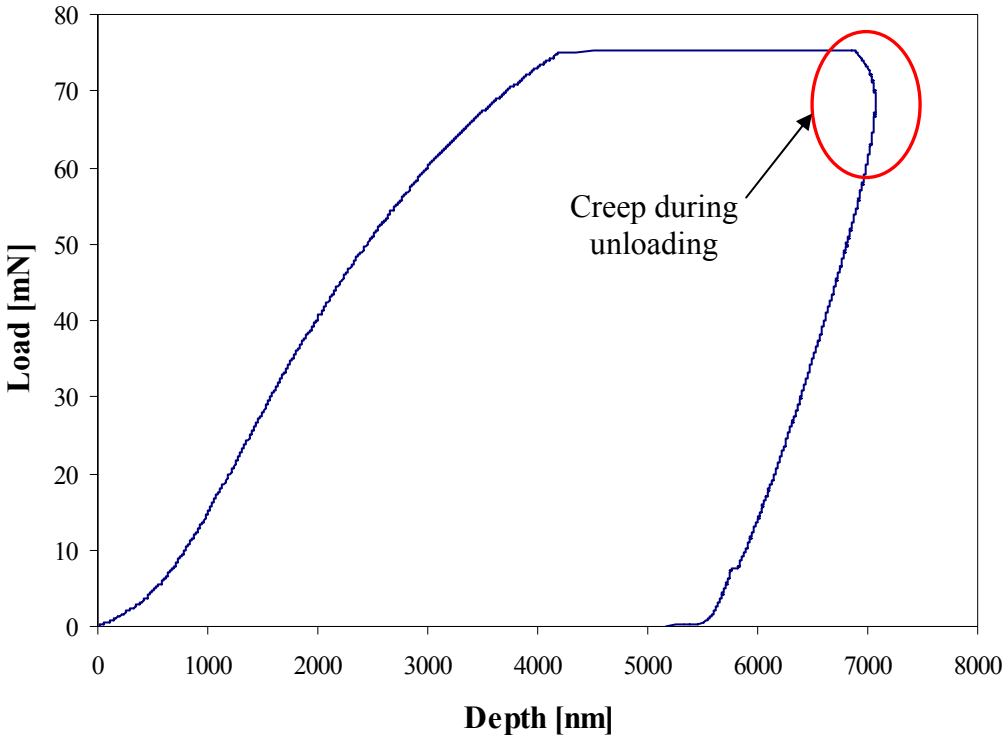

Figure 3.42: Representative load-depth curve of Berkovich nanoindentation test performed on a CNT-reinforced SU-8 film. Creep appeared during the initial part of the unloading phase, as highlighted, making the Oliver-Pharr analysis of the results invalid.

It was possible, however, to find an acceptable set of parameters for Berkovich nanoindentation test on unreinforced SU-8 films:

- Maximum force = 450 mN
- Maximum displacement (depth) = 5 μm
- Force loading rate = 2 mN/s
- Force unloading rate = 2 mN/s
- Holding time = 60 s

Twenty Berkovich nanoindentations tests were performed on pure SU-8 films with this set of test parameters. An additional set of 10 tests was performed changing the force loading and unloading rates from 2 to 7 mN/s, to determine the influence of the unloading rate in the results. Figure 3.43 shows a typical Berkovich indentation on the surface of pure SU-8 films.

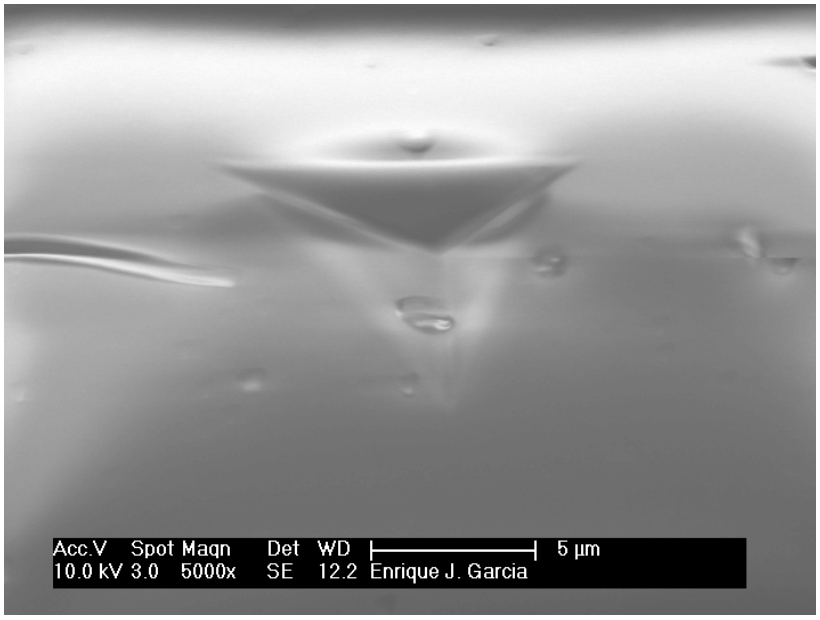

Figure 3.43: Berkovich indent on the surface of an unreinforced SU-8 film.

Two of the tests using the second set of parameters (loading and unloading rates of 7 mN/s) presented creep in the initial unloading phase and were discarded. The process to analyze the remaining 28 test results is the same previously used for the EpoThin films (described in section 3.4.2.1). A representative load-depth curve obtained from the Berkovich nanoindentation test is shown in Figure 3.44. As discussed previously, the two plateaus present in this figure correspond to dwell periods used for the nanoindenter to correct for creep (plateau at the maximum load) and thermal drift (plateau during unloading at 20% of the maximum load). The results obtained from the 28 valid Berkovich indentation tests are summarized in Table 3.6.

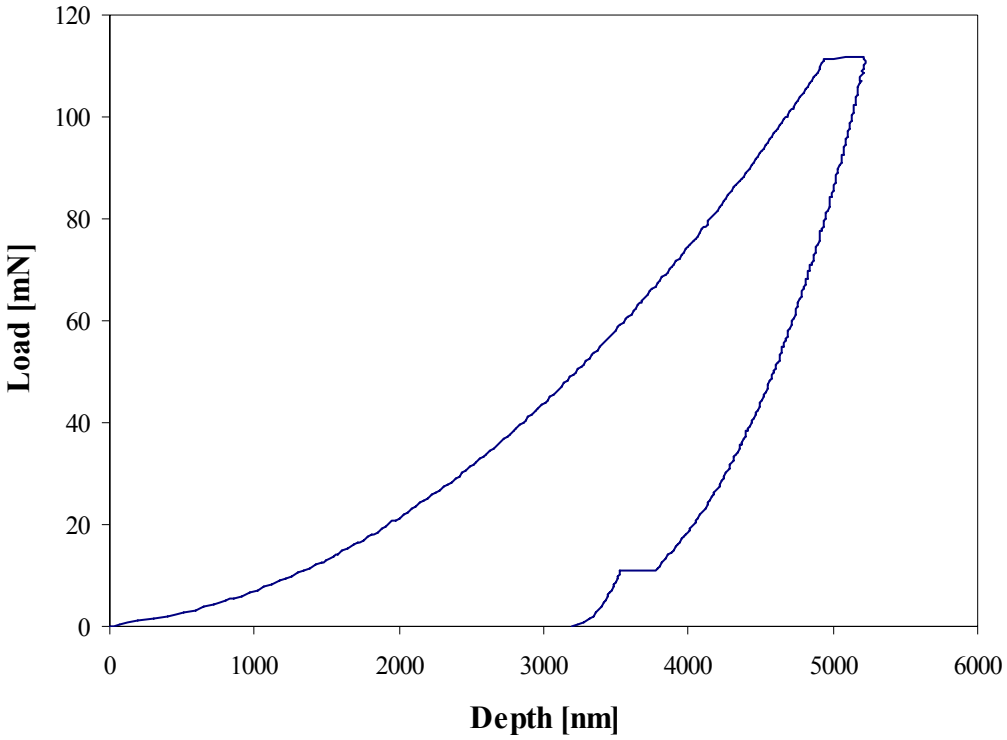

Figure 3.44: Representative load-depth curve for a Berkovich nanoindentation test on unreinforced SU-8 film.

Table 3.6: Young's modulus and hardness obtained from Oliver-Pharr's curve fitting for the unloading phase of Berkovich nanoindentation tests on pure SU-8 films for the two different loading rates (20 tests at 2 mN/s, 8 tests at 7 mN/s).

Unreinforced SU-8	Load rate = 2 mN/s	Load rate = 7 mN/s	Average of the 28 tests
Young's modulus [GPa]	4.612 ± 0.099	4.886 ± 0.103	4.690 ± 0.159
Hardness [GPa]	0.227 ± 0.009	0.223 ± 0.004	0.226 ± 0.006

The increase in the loading and unloading rates increases the Young's modulus of the SU-8 film by 5.7% and decreases the hardness around 1.8%. The average value of the 28 tests was used to compare the Berkovich results with those obtained from compression tests. The final Young's modulus obtained from the Berkovich tests (4.69 GPa) is close to the 4.5 GPa reported by the manufacturer.

As mentioned previously, due to creep during unloading no valid results were obtained from nanoindentation tests on CNT/SU-8 nanocomposites.

Compression tests were performed on pure SU-8 and CNT/SU-8 pillars (see Figure 3.23.b and Figure 3.24, respectively) using an 80-µm diamond flat punch. As mentioned in section 3.4.1.1, SU-8 was selected among other reason because it is a UV-curing epoxy, which allows the fabrication of pillars by selectively curing patterns. Using both materials to fabricate pillars it is possible to compare results from the same type of test (compression), and therefore, to better measure the reinforcing effect of the CNTs on the pillars than in the case of the temperature-curing EpoThin epoxy.

The acceptable test parameters for the unreinforced SU-8 compression tests were determined with 5 initial compression tests:

- Maximum force = 450 mN

- Maximum displacement (depth) = 2.5 μm
- Force loading rate = 1 mN/s
- Force unloading rate = 1 mN/s
- Holding time = 60 s

Thirty compression tests were performed on individual cylindrical SU-8 pillars of diameter 40 μm and height 40 μm. A representative load-depth curve for these compression tests is shown in Figure 3.45. The Young's modulus for each pillar was obtained from the analysis of the experimental load-depth curves. As performed previously for the CNT/EpoThin pillars, the load-depth curves were analyzed in unloading (using Oliver-Pharr's nanoindentation theory) and in loading (elastic modulus obtained from the slope of the stress-strain curve). The results obtained for both analyses, and also from Berkovich indentation, are presented in Table 3.7.

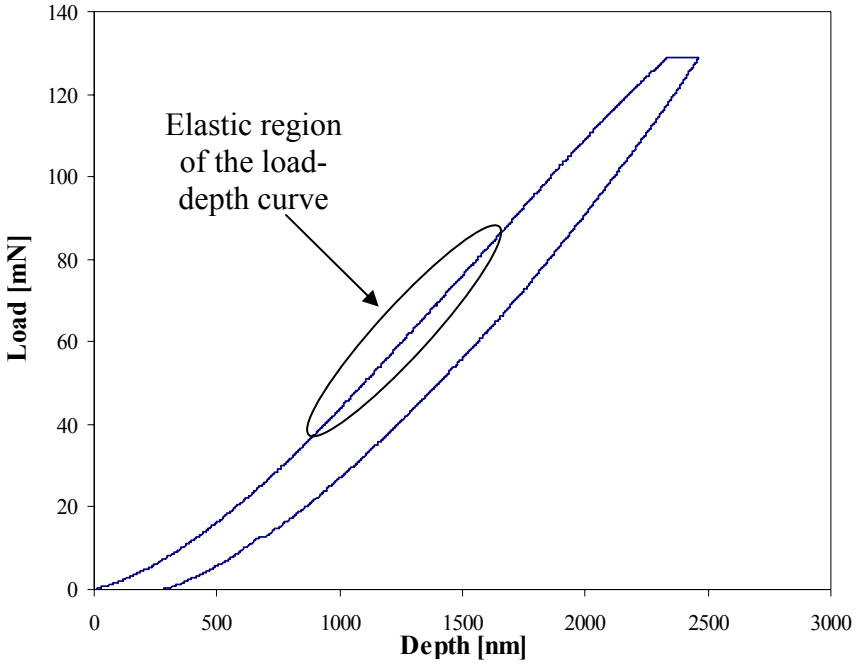

Figure 3.45: Representative load-depth curve for a compression test on an unreinforced SU-8 pillar.

Table 3.7: Comparison of the Young's modulus of unreinforced SU-8 obtained from Berkovich indentation of pillars, and from compression tests of pillars using two different techniques: modified Oliver-Pharr's curve fitting for the unloading and the analysis of the stress-strain curve during loading.

	Berkovich indentation	Compression tests: Loading (from the stress-strain curves)	Compression tests: Unloading (Oliver-Pharr's theory)
Young's modulus [GPa]	4.612 ± 0.099	3.887 ± 0.099	3.693 ± 0.309

As seen in the table, the elastic modulus estimated by the compression tests is between 15%-20% below the results obtained from Berkovich indentation. The loading and unloading rate for the compression tests (1 mN/s) is lower than the rate used in the Berkovich indentation (2 mN/s) which could explain the difference. However, the results obtained from Berkovich indentations indicated only a weak dependence on the loading rate for the SU-8. The results obtained from the loading region provide a slightly (5%) higher Young's modulus and also a narrower distribution than the unloading analysis. Both compression test results (loading and unloading using modified Oliver-Pharr) are in excellent agreement (5.5% higher in loading), as noted for the CNT/EpoThin pillars as well (see Table 3.5).

Compression tests were also applied to 25 CNT/SU-8 nanocomposite pillars. A careful selection of the pillars in terms of verticality and regular contraction had been made prior to the tests. The position in the patterned specimen and the dimensions (diameter and height) of each selected pillar was measured using SEM imaging. From initial tests the acceptable testing parameters were selected:

- Maximum force = 450 mN
- Maximum displacement (depth) = 7.5 μm

- Force loading rate = 1 mN/s
- Force unloading rate = 1 mN/s
- Holding time = 60 s

The initial tests also showed that the slightest misalignment between the z-axis of the indenter and the pillar, or irregularities in the contraction of the pillar, produced an irregular distribution of the pressure in the pillar which generated a bending moment on the specimen that partially broke imperfect pillars at their base, as shown in the three examples in Figure 3.46. Note that the fracture surfaces indicate complete wetting (no cells or voids formed during wetting), as discussed in section 3.3.2.

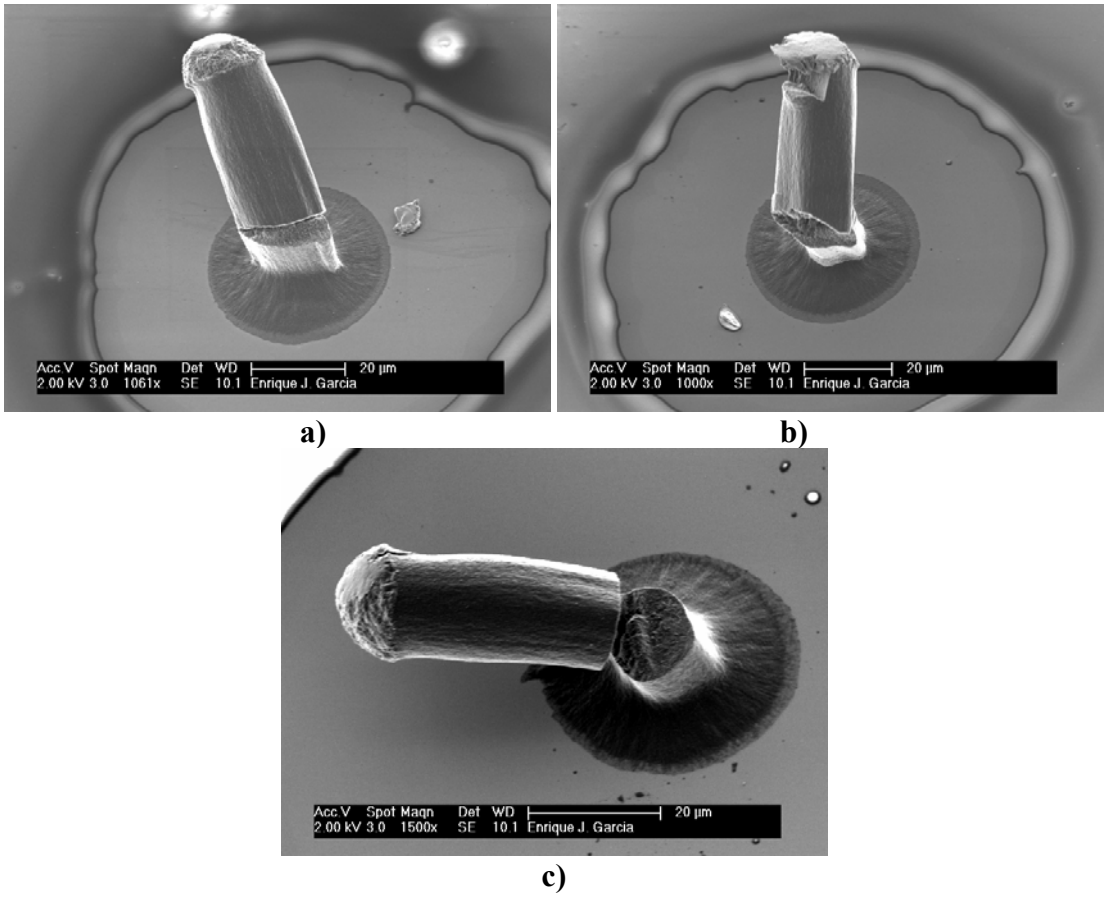

a) **b)**

c)

Figure 3.46: Pillars broken at the base due to slight variations in their verticality and/or irregular contraction.

The load-depth curves for these imperfect pillars clearly reveals the point at which the pillars fracture, as shown in Figure 3.47. From that point, the fracture grows, increasing the misalignment until the test parameter of maximum depth (7.5 μm) is reached. The maximum load is maintained for 60 seconds, which explains the further increase in depth (from 7.5 μm to 10 μm in Figure 3.47).

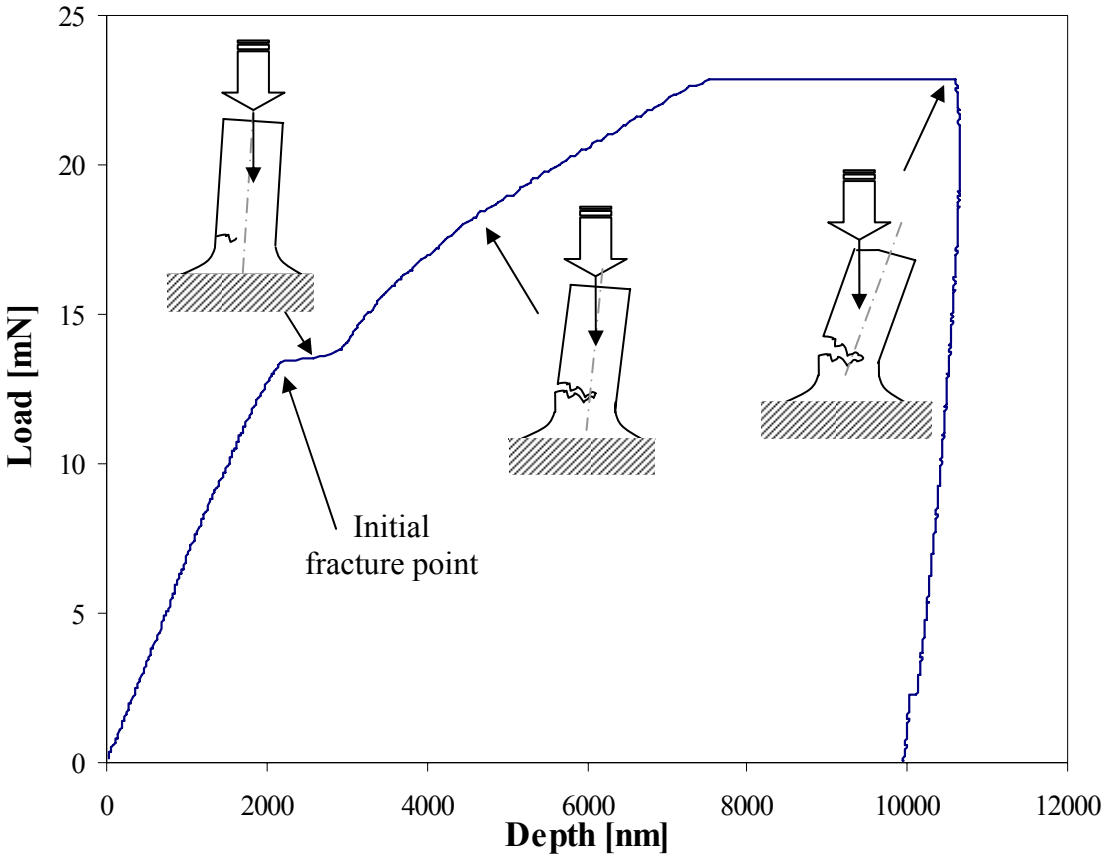

Figure 3.47: Representative load-depth curve for imperfect pillars. The illustration shows an initial rupture point and additional displacement of the indenter while the maximum load is held for 60 seconds.

From the 25 selected pillars that were tested, 19 showed the behavior illustrated in Figure 3.47, and the results were discarded. The remaining 6 pillars, however, allowed pure compression tests. SEM images of one of the pillars subjected to pure compression tests before, and after the test, are shown in Figure 3.48. As seen Figure 3.48.a) and b), the alignment and regularity of the contraction during wetting are almost perfect. Also, it is important to note that the pillars had a region of partially wet CNTs on top forming a dome of height ~5-7 μm for pillars with total lengths ~40-100 μm. The dimensions of the 6 CNT/SU-8 pillars successfully tested are presented in Table 3.8.

Table 3.8: Dimensions of the 6 CNT/SU-8 Pillars Successfully Tested in Compression.

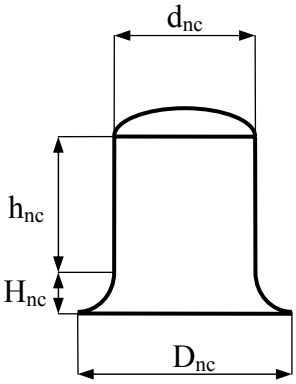

Pillar	d_{nc} [μm]	D_{nc} [μm]	d_{nc}/D_{nc}	h_{nc} [μm]	H_{nc} [μm]	h_{nc}/H_{nc}
1	25.8	38.5	0.67	42	7	6
2	27.1	38.5	0.7	40	5	8
3	27.9	38.5	0.72	41	6	6.8
4	29.5	38.5	0.76	42.4	4	10.6
5	27.3	38.5	0.71	38.8	4	9.7
6	28.2	38.5	0.73	41.8	5	8.36

During the compression test, this dome is flattened by the punch, as seen in Figures 3.48.c) and d). It is also important to note the formation of cracks (see Figure 3.48.c and d, and Figure 3.50.b) during the compression test in all 6 specimens that were tested successfully in pure compression.

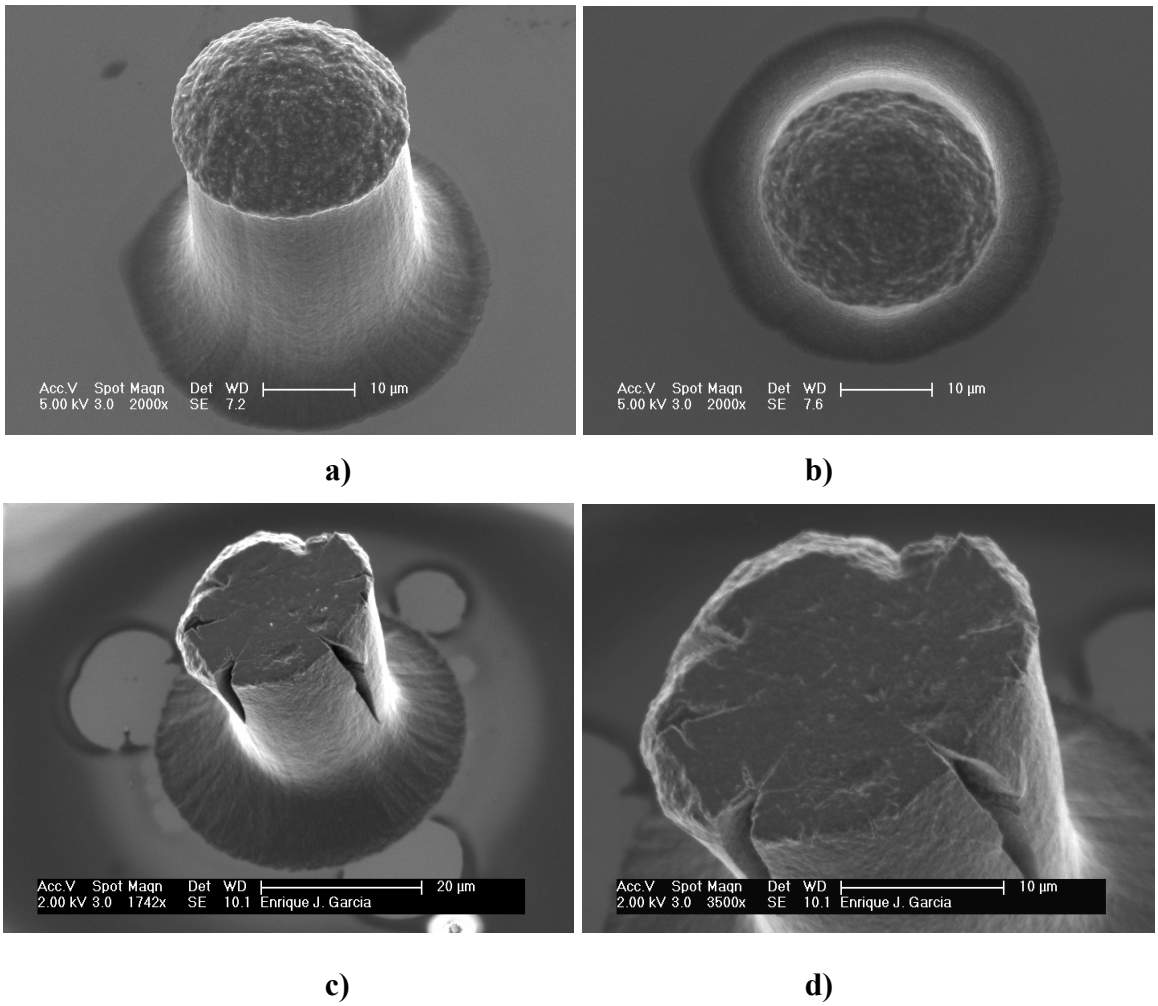

Figure 3.48: SEM images of a) vertical CNT/SU-8 nanocomposite pillar; b) top view of the pillar, showing verticality and regular contraction; c) pillar after compression test (note that the dome has been flattened out during the test); d) closer view of the flattened dome.

A typical load-depth curve obtained from the 6 compression tests is shown in Figure 3.49. The initial phase of the test flattened the dome. The cracks shown in Figures 3.48.c) and d) are believed to be formed at the region of the load-depth curve marked as (2), and that correspond to a softening of the nanocomposite pillar (decrease of the slope of the curve). After the dome was flattened, the slope of the load-depth curve increases considerably, evidence of the stiffness of the CNT-reinforced SU-8 under the dome.

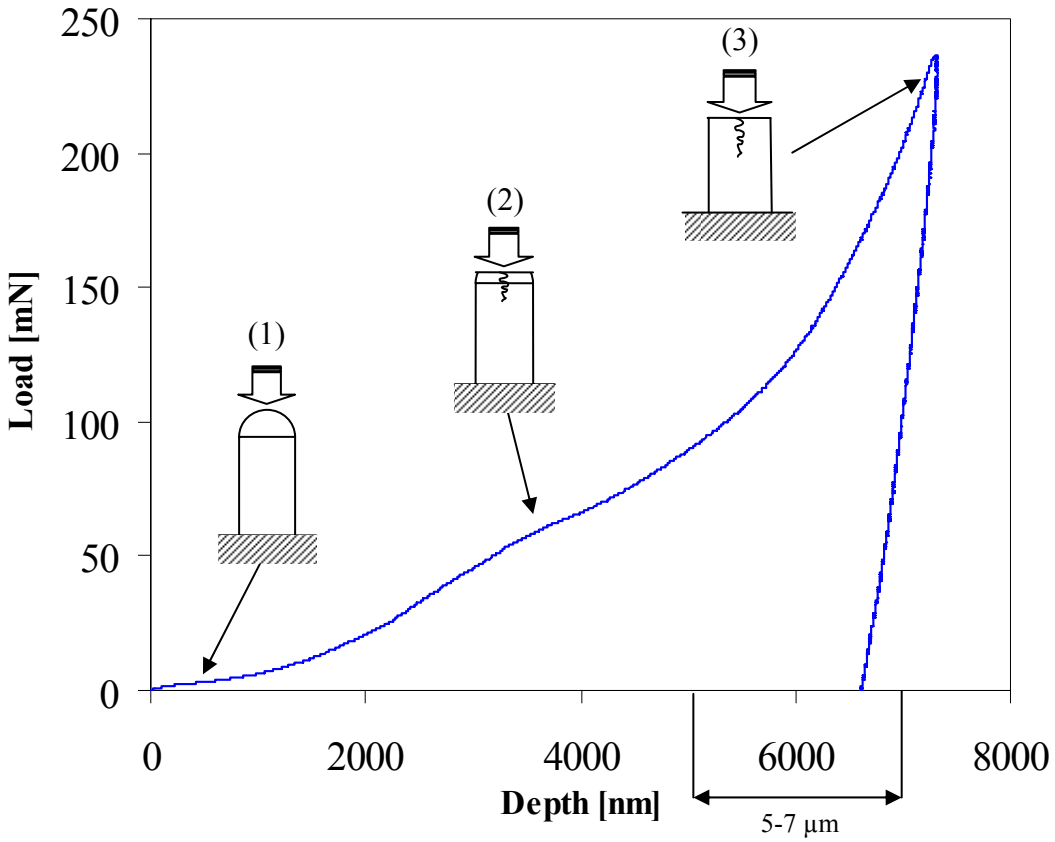

Figure 3.49: Representative load-depth curve for good compression tests. The illustration shows the initial phase where the dome is flattened (1), the formation of the cracks (2), and a change in slope once the CNT/SU-8 nanocomposite below the dome takes the load (3).

Another pillar that was successfully subjected to a compression test is shown in Figure 3.50. As shown in Figure 3.50.b), cracks were formed during the compression test for this pillar too. The corresponding load-depth curve obtained for this pillar is shown in Figure 3.51. The same softening region that appeared for the previous pillar (see Figure 3.49) is present for the load-depth curve for the compression test of the pillar shown in Figure 3.50, but is less severe than in Figure 3.49, likely because the cracks are smaller.

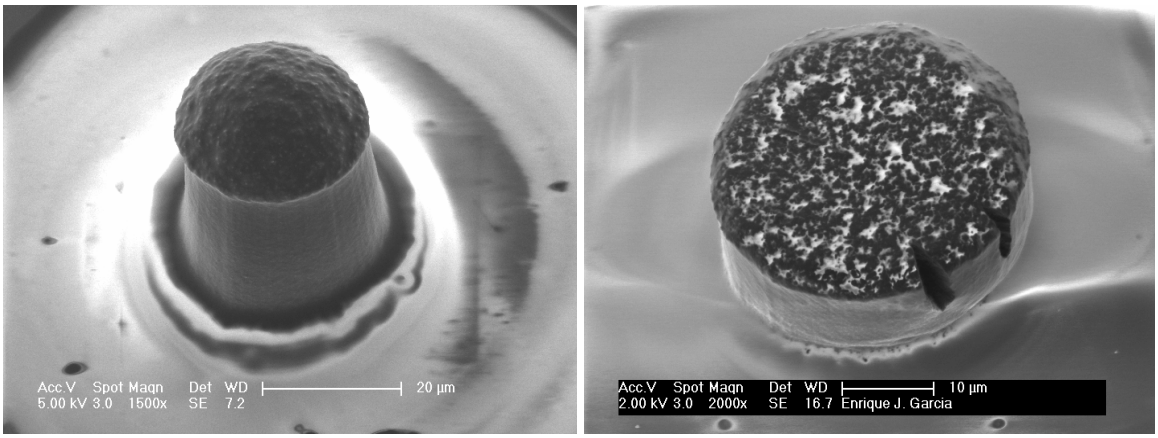

a) **b)**

Figure 3.50: SEM images of a) vertical CNT/SU-8 nanocomposite pillar; b) pillar after compression test (note that the dome has been flattened out during the test).

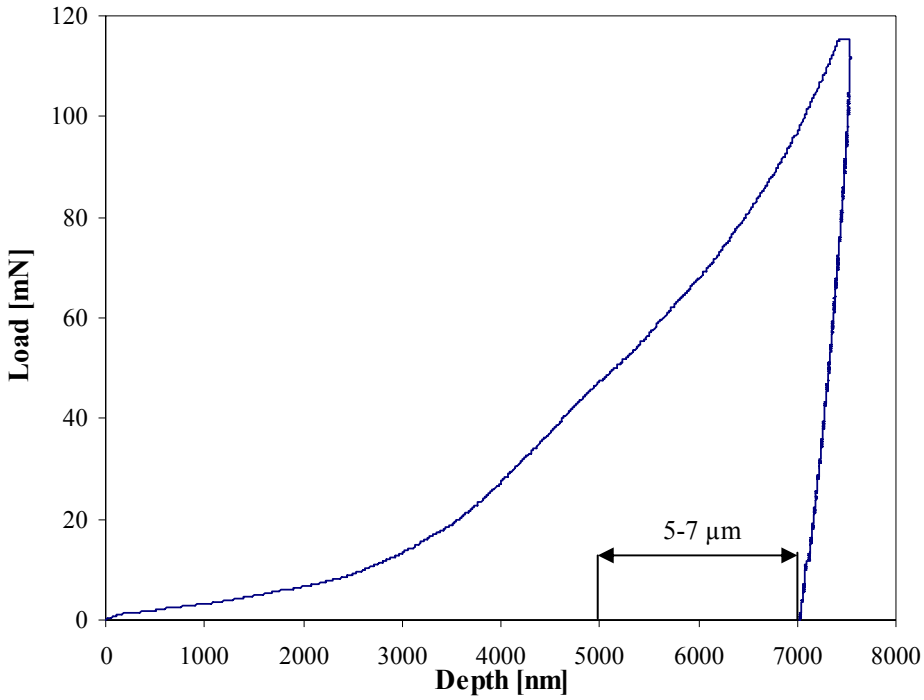

Figure 3.51: Load-depth curve obtained for the pillar shown in Figure 3.50.

The load-depth curves for the compression tests show that due to the presence of the dome, there is no linear-elastic region that can be analyzed to determine the elastic modulus during loading. Due to limitations on the deflection range in the nanoindenter,

further compression beyond ~7 μm was not possible. However, the Oliver-Pharr's indentation technique can be used to analyze the unloading region. The results obtained from the unloading analysis of the compression tests applied for unreinforced SU-8 and CNT/SU-8 pillars are compared in Table 3.9. The effective reinforcement for these pillars is close to 220%, increasing the Young's modulus from 3.7 to 11.8 GPa. Also, it is important to note that the standard deviation for these pillars (1.409 GPa) is larger than the results obtained for unreinforced SU-8, possibly due to the reduced number of valid tests (6) available.

Table 3.9: Comparison of the Young's modulus of unreinforced SU-8 and CNT/SU-8 pillars obtained from compression tests.

	Unreinforced SU-8	CNT/SU-8 Nanocomposite	Reinforcement
Young's modulus [GPa]	3.693 ± 0.309	11.815 ± 1.409	219.9%

The reinforcement for the CNT-reinforced SU-8 is close to 220%. This increase is considerable compared to the 25% obtained for the CNT/EpoThin nanocomposite films and the 70% for the CNT-reinforced EpoThin pillars subjected to compression. For these CNT/SU-8 pillars, as was observed with the CNT/EpoThin ones, due to the contraction of the pillars during wetting the volume fraction of CNTs is increased. The same technique used for the determination of the effective area for the CNT/EpoThin pillars (see Figure 3.40) allowed estimating the volume fraction of the regularly contracted CNT/SU-8 nanocomposite pillars. The volume fraction changes from the original 0.9% to 2% due to this contraction. The ideal Young's modulus for the CNT/SU-8 nanocomposite calculated using the rule of mixtures presented in equation (3.7), is 23.6 GPa, two times

larger than the 11.8 GPa obtained from the compression tests. As the volume fraction is similar to the one obtained for the CNT/EpoThin pillars, it is possible to compare both results. The reinforcement goes from 70% and a ratio between idealized model and experimental of 3.67 for the EpoThin nanocomposites to 220% and a ratio of 2 for the CNT-reinforced SU-8. The improvement in the effective reinforcement in the case of the SU-8 nanocomposites is attributed to a better distribution of the epoxy around the CNTs (avoiding the formation of aggregates and voids, and wetting individual CNTs), and to a better alignment of the wet CNTs.

3.5 Summary of Nanocomposite Testing

The feasibility of hybrid composite materials strongly depends on the two factors studied in this chapter: wetting of the carbon nanotubes with commercial polymers and effective reinforcement of the matrix by the CNTs.

The wetting results from the two sets of tests that used the high-viscosity conductive epoxy clearly show that the capillarity effect wets CNTs even in the most adverse (*i.e.*, highly viscous) conditions. This finding may be particularly interesting for manufacturing processes (infusion processes) such as resin infusion molding (RIM) or resin transfer molding (RTM) where the wetting of the fiber is often a limiting factor. The resins generally used in these processes have much lower viscosities (around 10 cPs at the process temperature [135]) than the conductive epoxy used for this test. The viscosities for these infusion-process resins are the same order of magnitude as the SU-8 used in the third set of wetting tests and in the nanocompression tests. Therefore, good

wetting is likely from the polymer resins commercially used with the CNT forests grown in this work.

As mentioned in the introduction for section 3.4, direct measurements of the mechanical properties of the CNT/polymer nanocomposite materials are preferred to indirect measurements based on structural models. Traditional nanoindentation tests have been performed in other works to obtain the hardness and Young's modulus of thin films containing randomly oriented CNTs dispersed in the matrix using the different techniques presented in section 2.2.2. However, there are no previous results of direct measurements of the Young's modulus of nanocomposites containing well-aligned CNTs, such as the ones used for this work. This research is the first work to report direct measurements for the Young's modulus, not only using traditional nanoindentation techniques, but also using compression tests applied on nanocomposite micropillars along the CNT axis. The results obtained using the modified Oliver-Pharr unloading analysis are consistent with the analysis of the loading region of the load-displacement curve in our tests. The addition of well-aligned CNTs to a polymer matrix effectively reinforces the matrix mechanical properties of the CNT/polymer nanocomposite materials, as seen in section 3.4. The results obtained indicate that epoxies with low viscosities (on the order of 1 to 10 cPs, the viscosity of RTM commercial epoxies at the process temperature) are more effectively reinforced than higher viscosity epoxies, such as EpoThin (200 cPs at room temperature). It is also important to remember that the effective reinforcement obtained for the two CNT/epoxy nanocomposites tested is below the idealized rule of mixtures presented in section 3.4, but considerably higher than using randomly oriented CNTs

embedded into the polymer matrix (2.5 times less volume fraction of CNTs is needed to obtain the same level of reinforcement provided by randomly oriented CNTs).

Both wetting and mechanical tests contribute to demonstrate the feasibility of fabricating hybrid architectures based on aligned forest of CNTs grown using the thermal CVD method. Two such architectures will be explored in the next chapter.

Chapter 4. Fabrication and Testing of Hybrid Composites

4.1 Introduction

The combination of CNTs, (polymer) matrices, and advanced fibers to create so-called hybrid composites is seen as a practical approach to deriving structural/multifunctional benefits from CNTs. The purpose of this chapter is to explore the feasibility and scalability of different architectures of hybrid CNT/traditional composites. Two different architectures will be studied: The first one is based on the CVD growth of CNTs perpendicular (radially) to the fibers' surface. In the second one, well-aligned densely packed CNTs were placed on a prepreg ply of a traditional composite material to study manufacturability of a new interlayer toughening concept.

The first architecture reinforces the composite materials by using aligned long MWCNTs grown on fiber surfaces, where the CNT length is on the order of the fiber diameter or greater. The CVD process used in this work allows the fast growth of 3-mm long aligned CNTs. In order to better represent real hybrid composite architectures, the growth of the CNTs on the fibers was limited to 30 μm, still an order magnitude longer than previous studies [106], and likely an order of magnitude greater than desired for

interlaminar and intralaminar reinforcement. Posterior wetting of the fibers with CNTs embedded is expected to allow effective reinforcement.

In the second architecture, composite mechanical properties can be improved by reinforcing with CNTs the weakest point of the laminate assembly: The interface between plies of composites. Well-aligned CNTs are placed perpendicular to the plane of the laminate and wet, to assess feasibility of creating nano-stitches between the plies, as discussed in section 4.3.

The final goal for both configurations is to create macro-scale hybrid composite architectures that on the one hand improve the structural performance of the traditional composite materials, and on the other hand take advantage of properties of the CNTs to create multifunctional materials. This work explores, and demonstrates, the feasibility of the fabrication of both architectures using the thermal CVD CNT growth process described in section 3.2.

4.2 Hybrid Composites Using CNTs Grown on the Fibers' Surface

Perhaps the most promising results to date on hybrid composites are related to the improvement in the fiber/matrix interface by growing CNTs on the surface of the fibers. Several studies have shown that growing carbon nanotubes on the surfaces of fibers by CVD methods [118] significantly increases the surface area over which to transfer load (*e.g.*, from 1.77 to 17.2 m^2/g after growing 500-nm-long CNTs on the surface of graphite fibers [106]), thus increasing the interface shear strength (15% measured improvement with the CNTs previously mentioned [106]). Lastly, the CNTs produce a local stiffening

of the polymer matrix near the interface, contributing to an increase of the load transfer. However, the CNT lengths obtained to date vary from 200 nanometers to 1-2 microns [100],[106], and due to the limited length of the CNTs the reinforcement of the matrix is limited to the vicinity of the fiber.

Effective use of CNTs in a composite material demands well-aligned CNTs that are also well-dispersed in the matrix. The growth of CNTs grown radially on the surface of the fiber allows a dense, controlled distribution of the CNTs in the matrix. The thermal CVD method used in this work [109] yields considerably longer CNTs than the studies found in the literature. Due to this capability, the reinforcement of the matrix is not limited to the vicinity of the fiber/matrix interface. The CNT lengths are greater than the fiber diameters and long enough to fully populate the matrix region between fibers in a typical aligned-fiber advanced composite ply to create interlaminar toughening of the entire matrix. CNT weight fractions (~ volume fraction) obtained in this study (~2% after contraction) for CNTs in a polymer matrix are on the same order as the ones obtained by embedding CNTs into polymer matrices using sonication or other methods of dispersion by others. No additional dispersion step is needed when the CNTs are grown directly on the fiber surface. An effective reinforcement of the entire matrix is envisioned using this method, provided that the wetting of the CNTS-on-fiber structure with a polymer is possible.

The possible degradation of the mechanical properties of the fibers subjected to the process for growing CNTs, a process that requires high temperatures and the fiber being exposed to chemicals was investigated. Tensile tests were applied to single fibers in

the different stages of the process to determine their basic mechanical properties. Results are provided in section 4.2.2.

4.2.1 Growth of Carbon Nanotubes on the Surface of Alumina Fibers

The process used to grow the CNTs on the surface of the fibers is a variation of the thermal CVD process described in section 3.2 with Si wafers as a substrate. John Hart, in MIT's Department of Mechanical Engineering performed the growth of the CNTs.

For CNT forests growth on Al_2O_3 fibers, strands are cut from a commercially-available (McMaster-Carr) aluminum oxide (Al_2O_3) fiber cloth. Each strand consists of several hundred fibers each approximately 11 μm in diameter with a high volume fraction (~65%), as shown in Figure 4.1.a and Figure 4.1.b.

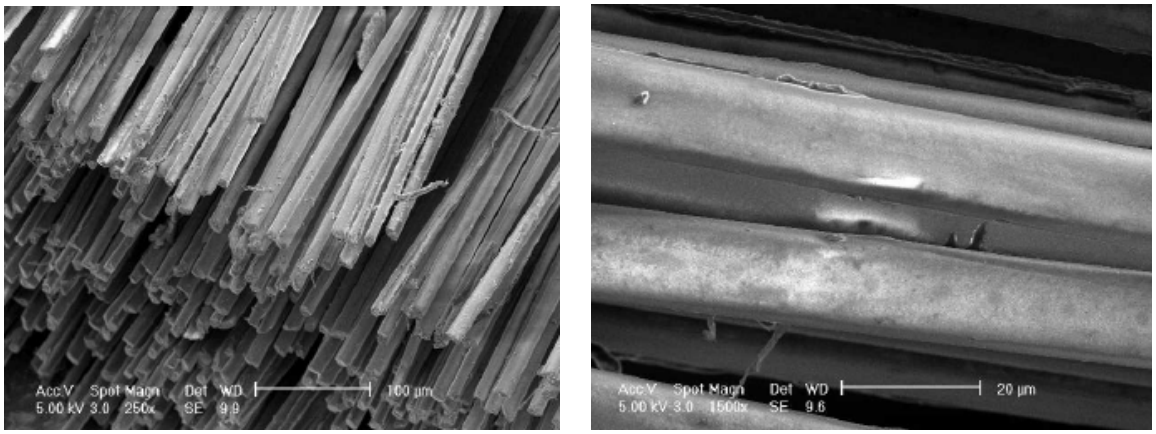

a) **b)**

Figure 4.1: SEMs of a) Pure alumina fibers; b) Close-up of pure alumina fibers.

The strands are soaked for 5 minutes in a 10 mM solution of $Fe(NO_3)_3 \cdot H_2O$ dissolved (by stirring and sonication) in isopropanol, and allowed to dry in ambient air. The CNT growth process is then the same as the one described for the CNT pillars in

section 3.2. A strand of alumina fibers after the CNT growth process is shown in Figure 4.2.a. The typical CNT growth rate for this process is about 2 μm per minute and the final length of the aligned CNTs is around 30 microns, as seen in Figure 4.2.c. The CNT long axis is oriented perpendicular to the fiber surface. The pictures were taken using an FEI/Philips XL30 FEG SEM.

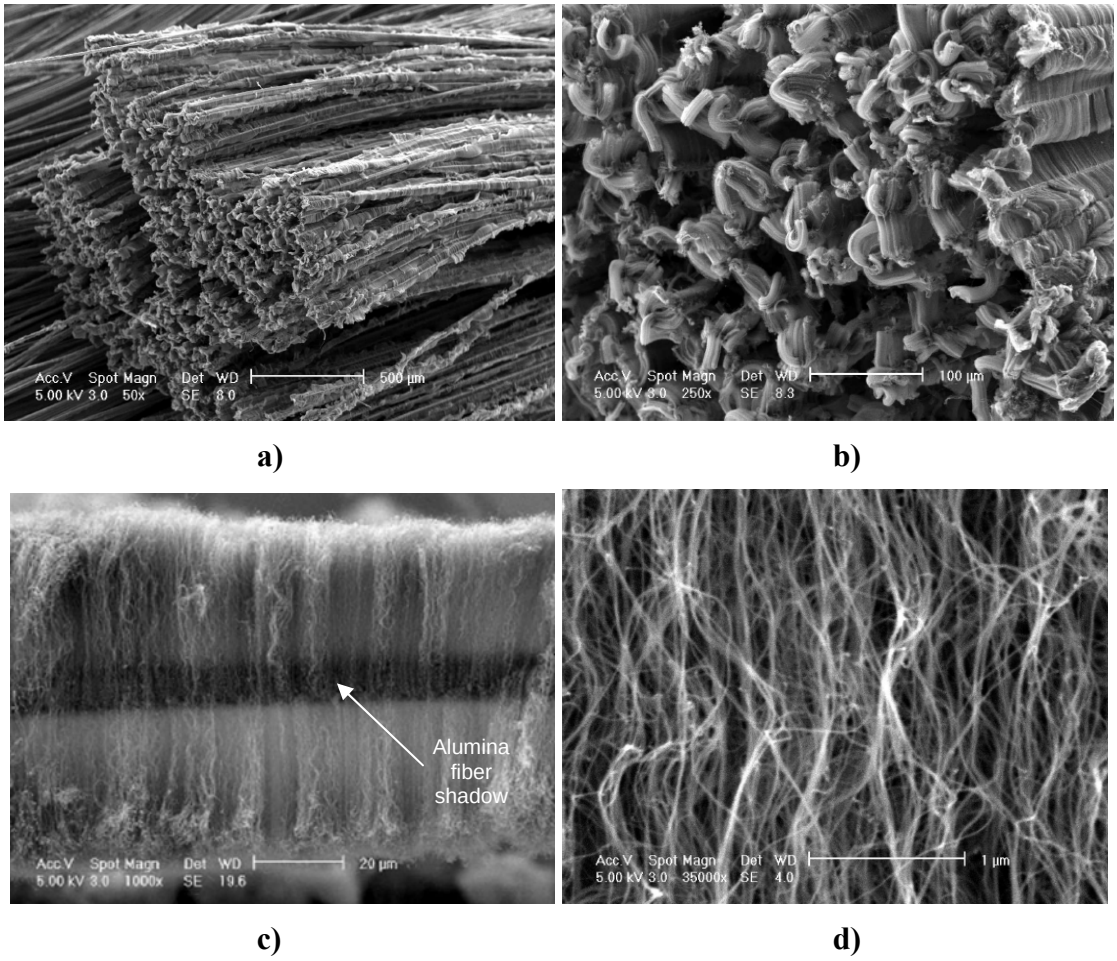

Figure 4.2: SEMs of a) Alumina fibers with CNTs grown on their surfaces; b) Closer view of the alumina fiber bundle with CNTs grown on the surface; c) Alumina fiber (shadow behind CNTs) with well-aligned, 30-μm long CNTs grown on its surface; d) Alignment of the CNTs grown on the surface of alumina fibers.

4.2.2 Single Fiber Tensile Test

As discussed previously, long (30 micron) MWCNTs were grown on commercially-available alumina fibers. The basic mechanical properties (elastic modulus, strength) of the alumina fibers in each step of the process were determined by single-fiber tensile tests and compared to assess degradation due to the CNT growth process.

4.2.2.1 Experimental Methods

Experiments were performed to compare the mechanical properties of the alumina fibers with and without CNT forests grown on the surface. A standard static tensile test, ASTM C 1557-03 [119], was applied to single fibers at different steps of the process (as-received fibers, fiber soaked in catalyst, and fibers after the CNT growth process) to measure modulus and strength. These tests served to examine whether the mechanical properties of the fibers are affected by the CVD process used to grow the CNTs. Previous work on the growth of CNTs on fibers does not report results on this important issue.

An Instron 8848 MicroTester with a calibrated 10-N load cell was used to perform the tensile tests. The microtester can apply and measure static loads ranging from 5 N to 2 kN. The resolution is 1 mN for load and 1 micron for displacement. Single fibers in this work failed at ~200 mN and ~600 μm displacement. The single fibers were carefully separated from bundles like the ones shown in Figure 4.3 and mounted with epoxy on cardboard tabs following the procedures in ASTM C-1557-03 [119]. Fiber length is ~50 mm, and CNT length is ~30 μm.

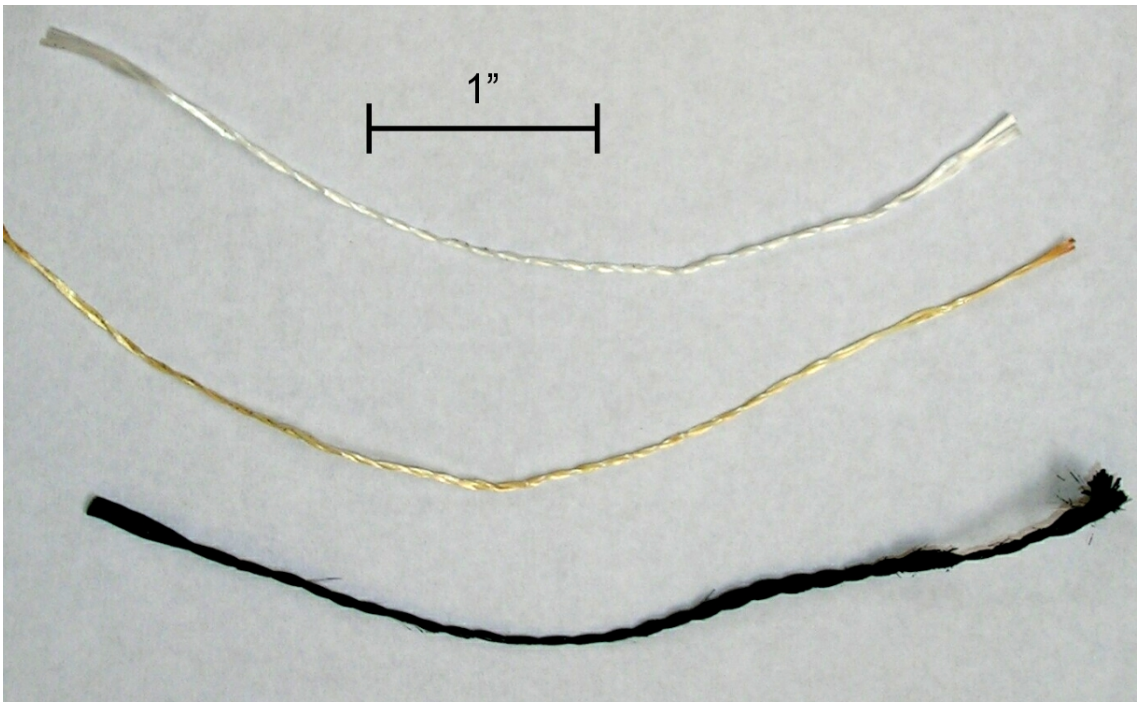

Figure 4.3: (top to bottom) Bundles of pure alumina fibers, fiber bundles soaked in catalyst, and fiber bundles with CNTs grown on their surfaces.

The tabs were then mounted on the machine (see Figure 4.4) and the tensile tests were performed at the ASTM recommended displacement rate of 8 μm/s. Load-displacement graphs were obtained for 10 samples of the pure alumina fiber, 6 of the alumina fiber wet with catalyst, and 10 of the final alumina fibers with CNTs grown on their surface. The load-displacement data were transformed into stress-strain plots to obtain fiber longitudinal modulus and strength. A nominal fiber area of 95 μm^2 (diameter of 11 μm) was used.

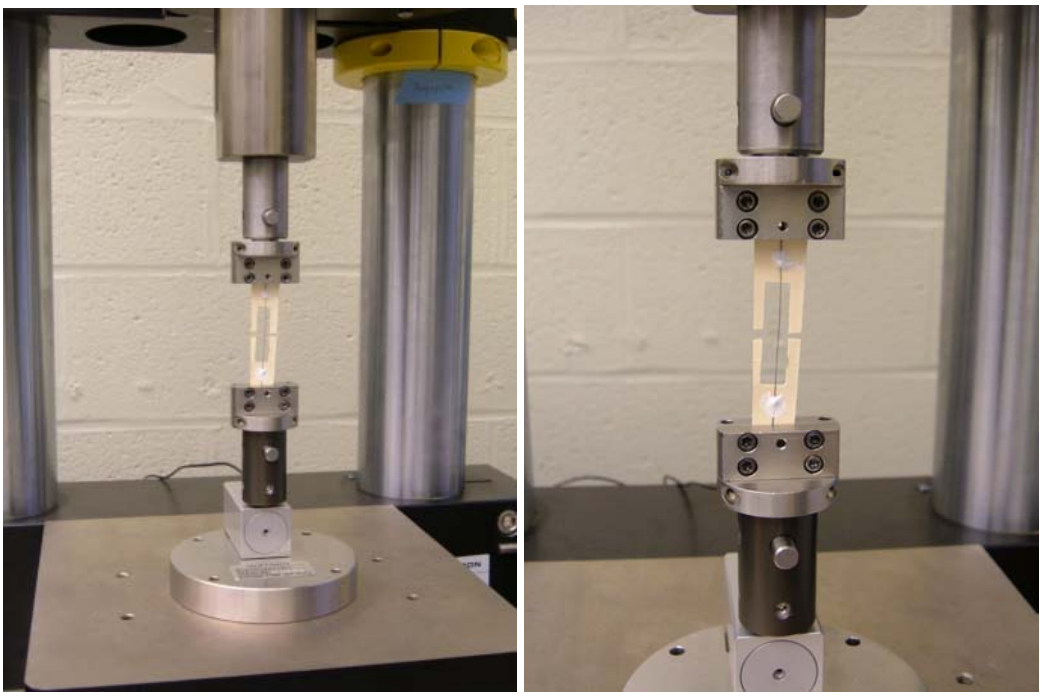

a) **b)**

Figure 4.4: a) Tab with a single alumina fiber with CNTs grown on its surface mounted on the microtester ready to start the tensile test; b) closer view of the assembly before starting the test.

Fiber strength is inherently associated with flaws in the fibers, and is characterized here using the Weibull distribution [120]. The Weibull distribution represents the probability of failure for a fiber at a particular stress (tensile strength), and can be expressed as:

$$p(x) = \begin{cases} \frac{\alpha}{\beta}\left(\frac{\alpha}{\beta}\right)^{\alpha-1} e^{-\left(\frac{x}{\beta}\right)^{\alpha}} & x \geq 0 \\ 0 & x < 0 \end{cases} \tag{4.1}$$

where β is the location parameter, α is the scale factor, and x is the parameter of interest, here strength. The location parameter, β, can be approximated by the average tensile strength:

$$\beta \approx \bar{x} \tag{4.2}$$

The scale factor, α, can also be approximated by the ratio between β (~average) and the standard deviation, S:

$$\alpha \approx \frac{\bar{x}}{S} \tag{4.3}$$

These approximations are employed in the data reported here. Results for these tests are presented in section 4.2.2.2.

4.2.2.2 Results and Discussion

In order for the first architecture described in this chapter to be feasible, the mechanical properties of the fibers should be maintained during the CNT process growth. Tensile tests were applied to fibers in each step of the process to assess whether the fibers were degraded, as described in section 4.2.2.1. The results for these 26 tests, summarized in Table 4.1, demonstrate that basic mechanical properties of the alumina fibers are maintained throughout the CNT growth process.

Table 4.1: Experimental modulus and strength results for pure alumina fibers, fibers soaked with catalyst and fibers after the CNT growth process.

	Tensile strength [GPa]		**Young's modulus [GPa]**		**Strain-to-failure [%]**	
	Mean	**Standard deviation**	**Mean**	**Standard deviation**	**Mean**	**Standard deviation**
Pure alumina fiber	2.19	0.19	135	6.38	1.63	0.13
Alumina soaked in catalyst	2.30	0.21	138	12.6	1.73	0.06
Alumina fibers with CNTs	2.28	0.09	134	11.3	1.63	0.16

Typical stress-strain curves for the alumina fibers at the three different stages of the process are shown in Figure 4.5. The single alumina fibers displayed classically linear-elastic brittle behavior. No important deviation of the properties was detected as shown in Table 4.1.

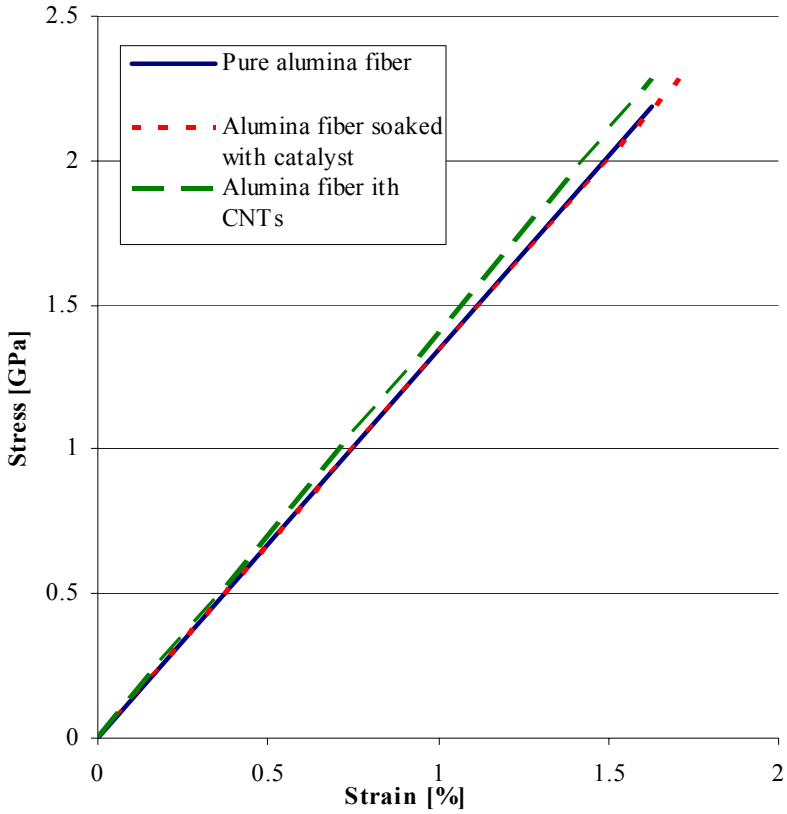

Figure 4.5: Typical single-fiber stress-strain curves

As mentioned in section 4.2.2.1, tensile strength can be approximated by a Weibull distribution, following Equation (4.1). The location parameter, β, and the shape factor, α, were calculated for all three fiber conditions according to Equations (4.2) and (4.3) respectively. The Weibull parameters for alumina fibers at each step of the process (dry fiber, fiber soaked in catalyst, and fiber after the CNT growth process) are given in Table 4.2.

Table 4.2: Weibull parameters for the tensile strength of alumina fibers.

	α	β
Pure alumina fiber	11.23	2.19
Alumina soaked in catalyst	11.21	2.30
Alumina fibers with CNTs	24.67	2.28

The Weibull distribution of the tensile strength is shown in Figure 4.6. As seen in the graph, the statistical distribution of the tensile strength is maintained almost constant after soaking the fibers with the catalyst. However, it is possible to detect an important difference after the fibers are subjected to the high-temperature CNT growth process. The distribution narrows considerably, possibly due to the reduction of residual stresses at the high temperatures reached in the oven.

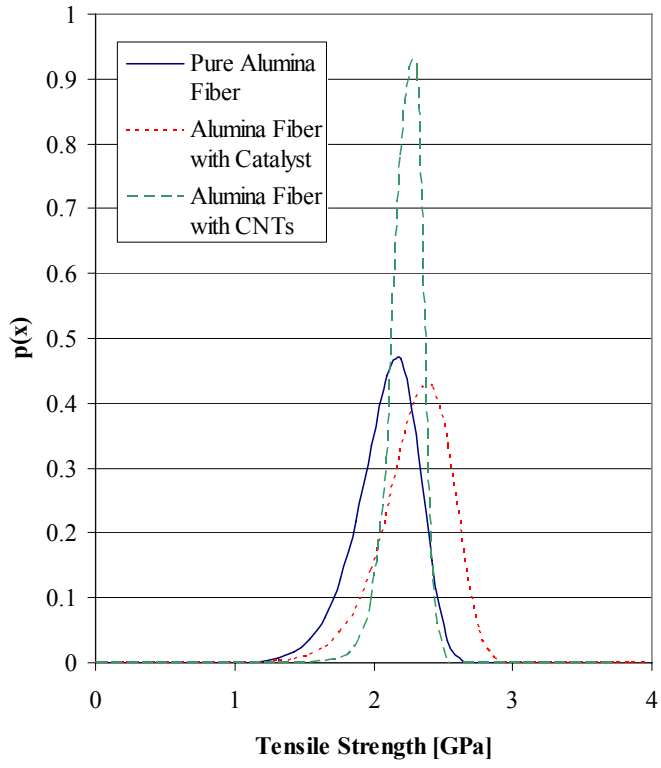

Figure 4.6: Weibull probability distribution for the tensile strength of the pure alumina fibers, fibers soaked with catalyst and fibers after the CNT growth process.

4.2.3 Summary

The uniquely long CNTs created by the growth process used in this work show promise for increasing the surface area available for load transfer between the polymer matrix and the fiber with grown CNTs. The data and results in this section indicate no degradation in strength and stiffness for alumina fibers undergoing the CVD CNT growth process. In addition to the increase in the surface area and the stiffening of the polymer, new reinforcement mechanisms should appear due to the length of the CNTs: aligned CNTs from different fibers can overlap one another and produce a further reinforcement of the matrix through bridging. The entanglement between CNTs grown on different fibers would also increases the load transfer between fibers and will likely help suppress or bridge matrix cracks that appear – effectively toughening the composite. This last bridging mechanism has been reported in the literature for CNTs in resins (no fibers present), but was limited due to very low weight fractions (lower than 5% to avoid the formation of agglomerates [52]) of CNTs randomly oriented and somewhat dispersed in a polymer matrix [55], [58]. An important advantage of the current method arises from the fact that CNTs are grown in-situ on the fiber surface, likely avoiding the problems related to the dispersion of the CNTs in the matrix.

4.3 Hybrid Laminated Composites Using CNTs at the Interface between Plies

The second hybrid composite architecture investigated is based on the addition of well-aligned CNTs to reinforce the matrix-rich region between plies of a traditional composite material.

The concept of reinforcing the region between plies had been used in previous studies with limited success. As mentioned in chapter 2, Dzenis *et al.* [91]-[92] introduced an additional layer of carbon nanofibers (CNFs) between plies of composite material. The CNFs used are randomly oriented in the plane of the laminate and have mechanical properties that are an order of magnitude lower than the CNTs, both limiting factors for the effectiveness of the reinforcement. Gibson [138] introduced a thin film of randomly oriented CNTs between plies, and mechanical tests showed no apparent improvement in the properties of the composite material. In both cases the reinforcement was introduced in the form of an additional layer.

The hybrid architecture proposed in this work is based on the patent-pending architecture presented by Wardle and Kim [123], and further developed by Wardle, García, Hart, and Slocum [115]. Vertically-aligned 20- to 30-μm long CNTs are placed between plies of graphite/epoxy prepregs and wet by the epoxy contained in the prepreg during curing. This architecture has two main advantages over Dzenis and Gibson's solutions: First, no additional layer is introduced in the laminate, and second, and more important, the CNTs are perpendicular to the ply/laminate plane, reinforcing the matrix in the direction where it is most needed. The aligned CNTs act as "nano-stitches" between the plies, bridging cracks produced at the matrix-rich interface, and also strengthening

and stiffening the interface. Analysis [123] has demonstrated the toughening is possible with CNTs in this configuration.

The CNT fabrication procedure for this hybrid architecture is described in [115]: First, CNTs are grown on silicon wafers using the thermal CVD process previously presented. The wafer is placed on top of a graphite/epoxy prepreg and the assembly is heated to reduce the viscosity of the prepreg's epoxy that wets the CNTs. Due to the low adhesion between the CNTs and their original silicon substrate, once the CNTs are wet by the first ply, it is possible to transplant them by mechanically removing the silicon wafer. The second layer of prepreg would then be added on top of the assembly. The complete laminate containing CNTs in the interface is then subjected to the curing cycle recommended by the prepreg manufacturer.

The most important factor for the feasibility of the fabrication process is the wetting of the CNTs by the epoxy in the prepreg. This work contains promising preliminary results that show that wetting of the CNTs by the epoxy contained in the prepreg and transplantation of these wet CNTs from their original substrate to the prepreg is possible, with CNT alignment perpendicular to the ply/laminate plane also maintained.

4.3.1 Growth of Carbon Nanotubes on Silicon Wafers

As mentioned previously, forests of CNTs were required to test the effective wetting of the CNTs by the epoxy contained in commercial prepregs. As opposed to the pattern of pillars of CNTs described in section 3.2, forests of CNTs were required for this test, modifying slightly the process: A continuous catalyst layer was deposited on 6" Si wafers. In this case no pattern was applied to the catalyst, because the desired

configuration was a forest of CNTs. The wafers with the catalyst layer were cut into 15-mm wide square pieces to fit in the quartz tube furnace (22-mm diameter). The thermal CVD process used to grow the CNT forests is the same described in section 3.2. CNT growth is performed in the same single-zone atmospheric pressure quartz tube furnace (Lindberg) previously used. The process parameters were also maintained. An example of the resulting dense forests of well-aligned, 200-μm long CNTs is shown in Figure 4.7.

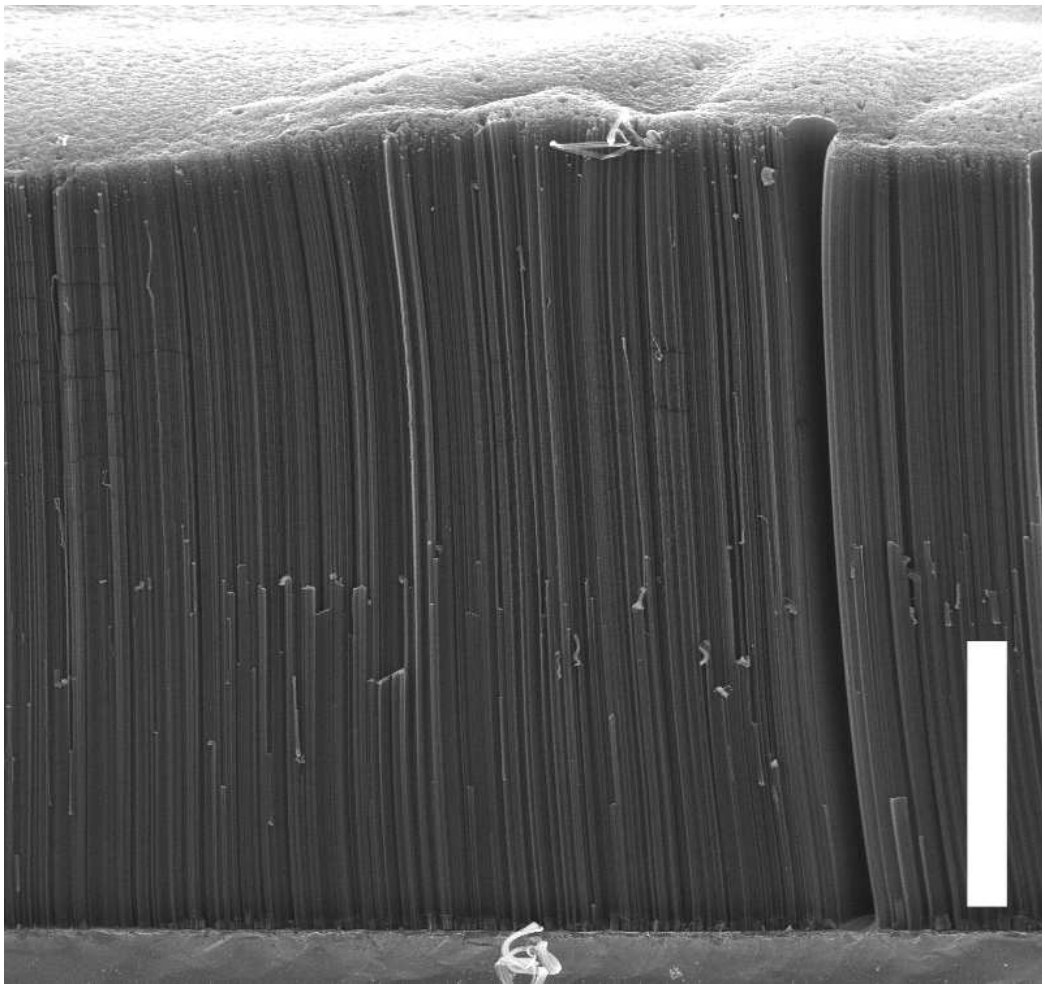

Figure 4.7: SEM of cross-section of a vertically aligned CNT forest grown using the thermal CVD process (Scale bar 70 μm).

4.3.2 Wetting of CNT Forests on Graphite Fiber/Epoxy Prepregs

The goal of this section is to verify the feasibility of the fabrication process established for the second hybrid architecture described in the introduction of this section. In this architecture, the CNTs are placed in between the plies of a prepreg laminate. Therefore, the epoxy needed for the wetting of the CNTs during the fabrication process comes from two different layers of prepreg (above and below the forest). The height for the CNTs (15 to 30 μm) needed for the hybrid architecture should be on the order of the inter-ply matrix region (~10 μm). The assembly should follow the curing process from the manufacturer, to avoid the flow of epoxy out of the laminate.

For this preliminary work, however, much more stringent wetting conditions were applied: The forest could only be wet by one layer of prepreg, instead of two, and no mold or confinement system was designed for the epoxy to avoid it flowing from the prepreg. Last, the available forests of CNTs used for the wetting tests were 300-μm long (at least one order of magnitude longer than needed for the hybrid architecture).

4.3.2.1 Experimental Methods

In this section, results are presented on the wetting of CNT forests placed on top of graphite fiber/epoxy prepreg tape (CSTsales C-PP150, thickness of 152 μm). For the tests, a 20 mm x 40 mm uncured prepreg strip was placed on a glass slide. A square 15-mm silicon wafer containing a dense forest of well-aligned, 300-μm long CNTs was placed on top of the prepreg with the CNTs in contact with the prepreg. A weight (20, 50, or 100 grams, corresponding to pressures of 870, 2170, and 4350 Pa) was placed on top of the assembly, as seen in the diagram in Figure 4.8.

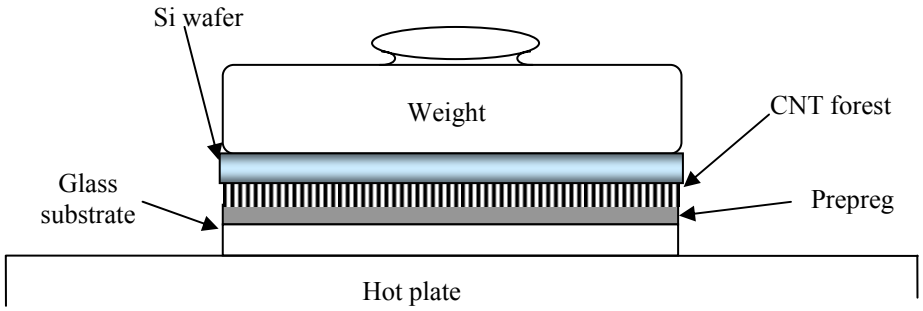

Figure 4.8: Diagram of the nano-stitching fabrication assembly (not to scale).

The curing process for the graphite epoxy system recommended by the manufacturer had two steps: In a first step, the temperature was increased at a constant rate of 3 ºC/sec to a temperature between 80 and 95 ºC. This temperature is to be maintained constant for 20 min. Then, the temperature is increased at the same rate used previously (3 ºC/sec) to 140 ºC and maintained for 60 minutes. After that, the assembly is cooled until it returns to room temperature. In the nanostitch fabrication here, no attempt to stop the resin from flowing was taken. After 2 hours, the prepreg and the Si wafer were separated by mechanical means. Parts of the forest were effectively transplanted from the wafer to the prepreg. SEM was used to check the wetting of the transplanted CNTs.

The process parameters varied are the weight placed on top of the assembly (ranging from 20 to 100 grams) and the initial temperature (80 and 93 ºC were tested). The largest weight (100 grams, 4350 Pa) rumpled the 300-μm long CNT forest and was only used in the initial tests. No results will be presented on this. The 20-g (870 Pa) and 50-g (2170 Pa) weighs used in the rest of the tests showed no appreciable differences. Therefore, the results presented in this work are just related to the change of the initial temperature.

4.3.2.2 Results and Discussion

Initial Temperature: 80 ºC for 20 min; Curing Temperature: 140 ºC for 60 min.

Using the lowest recommended initial temperature, two different methods were used to place the wafer containing the CNTs. In the first method, the prepreg was heated to the initial temperature and after 5 minutes the wafer was placed on top and maintained there for the rest of the process. After separating the two substrates (prepreg and wafer), SEM pictures were taken. The process produced irregular wetting of the forest, and large regions of the forest were not wet at all, and hence not transplanted to the prepreg. The regions that were effectively transplanted (~45% of the surface) presented different levels of wetting of the CNTs, as shown in Figure 4.9.

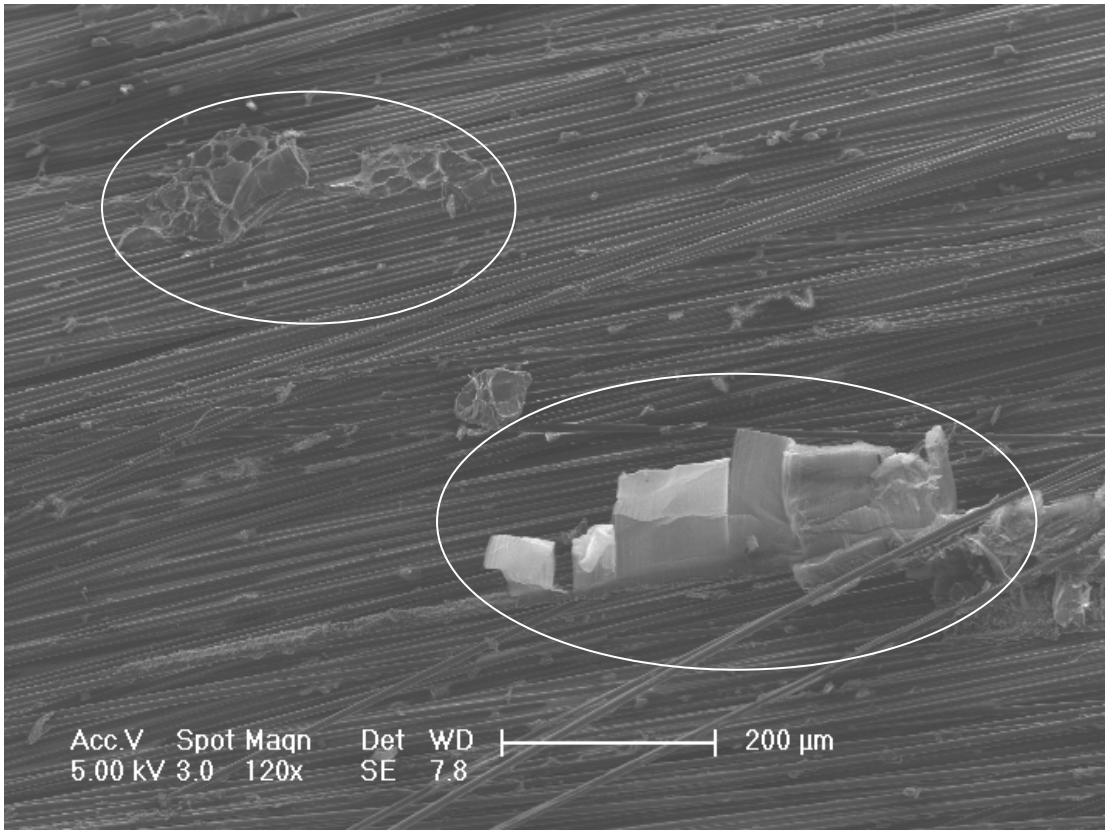

Figure 4.9: Large regions without CNTs transplanted. Two small regions (inside white circles) with CNTs transplanted are evidence of irregular wetting.

The two regions of CNTs transplanted that are shown on Figure 4.9 are the two main types of wetting found in the samples. On the bottom right, CNTs that are wet only at the base (as shown in the close-up pictures in Figure 4.10) are visible. Similarly to the SEM in Figure 3.10, the change in color marks the transition between the wet region and the region with pure CNTs (see Figure 4.10.a). From the SEM image shown in Figure 4.10.a), the height that the epoxy penetrated into the CNT structure is ~80 μm (image taken at 30º of inclination). The alignment of the CNTs is maintained in the wet region, as shown in Figure 4.10.b). The adhesion between the CNTs (wet at the base, as shown in Figure 4.10.c) and the prepreg tape was enough to allow the CNTs to be transplanted. However, the CNTs were not fully wet. As shown in Figure 4.10.b), the graphite fibers below the partially wet CNT forest are not covered with epoxy. As mentioned previously, during the test nothing impeded the epoxy flow to the bottom of the prepreg tape, thus reducing the amount of resin in contact with the CNTs. Therefore, a possible explanation for the lack of complete wetting is that the epoxy available on the surface of the prepreg was not enough to fully wet the CNTs. It is important to note that the resin available was "cannibalized" by the CNTs, leaving the graphite fibers below them without epoxy, as shown in Figure 4.10.b). The lack of epoxy appeared with this configuration (long CNTs on top of a single prepreg laminate), but would likely not be present in the foreseen hybrid architecture (~15 to 30 μm-long CNTs between *two* prepreg layers): First, shorter CNTs will require less epoxy to be wet. Second, epoxy from both prepreg plies will be available to wet the CNTs. Finally, the epoxy will not be allowed to flow out of the laminate during the curing process inside the autoclave, as occurred in these tests.

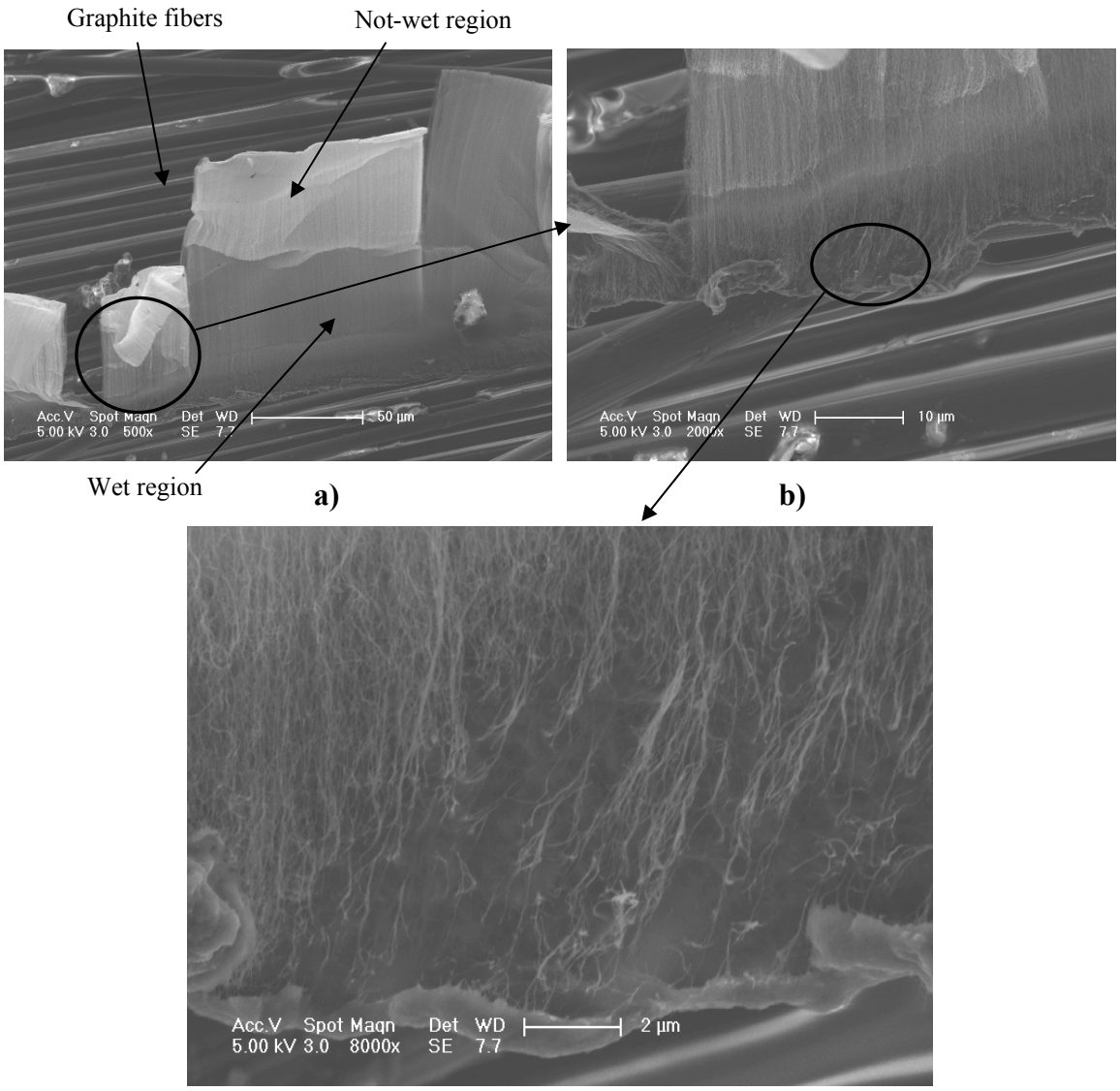

Figure 4.10: Close-ups of the irregularly wet region shown in Figure 4.9 (bottom right): a) General view; b) Close-up of the wet base of the pillars connected to the fibers of the prepreg; c) Closer view of the wet region at the base of the pillars.

The CNT region on the top left of Figure 4.9, on the contrary, appear fully wet with CNTs creating a honeycomb structure due to the contraction generated by the capillary forces during suction of the epoxy. The cell structure is consistent with previous results appeared in the literature [121] and also with the results shown in section 3.3 (see Figure 3.11 and Figure 3.19). A close-up of the honeycomb structure is shown in Figure

4.11. As seen in Figure 4.11.b), the walls of the honeycomb structure have a thickness of ~2 μm and do not appear to have voids inside the walls. It is also important to note in this SEM image that even if the CNT forest is highly contracted, the alignment of the CNTs is maintained.

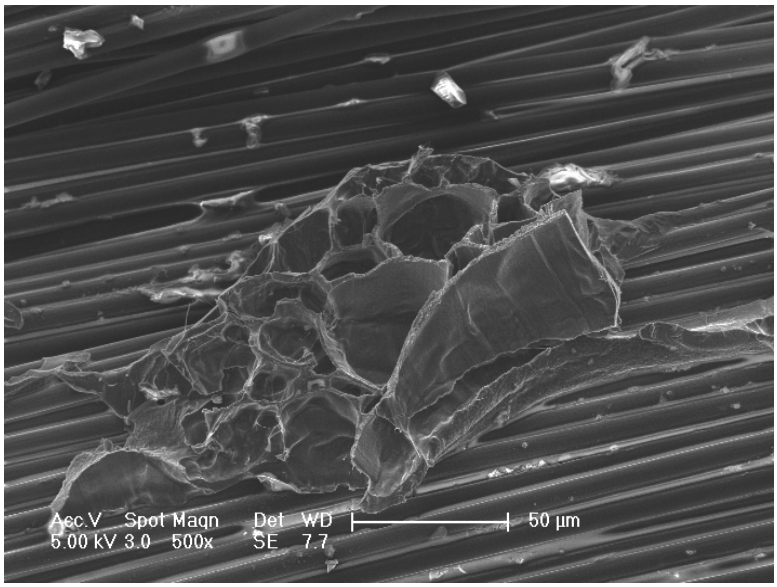

a)

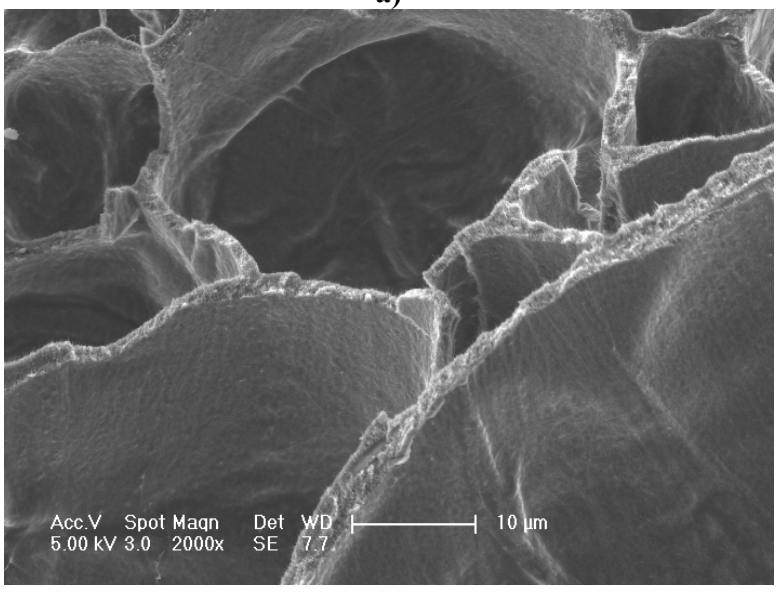

b)

Figure 4.11: a) Close up of the honeycomb structure shown in Figure 4.9 (top left); b) Closer view of the cells with thin (~2 μm) aligned CNT nanocomposite walls.

For the second method the CNTs were in contact with the prepreg before starting the curing process. The results were more regular, creating larger (~60% of the surface, 30% larger than with the first method) regions of transplanted CNTs. As shown in Figure 4.12, Regions of fully wet CNTs (see Figure 4.12.b) as well as CNTs wet only at the base (see Figure 4.12.a).

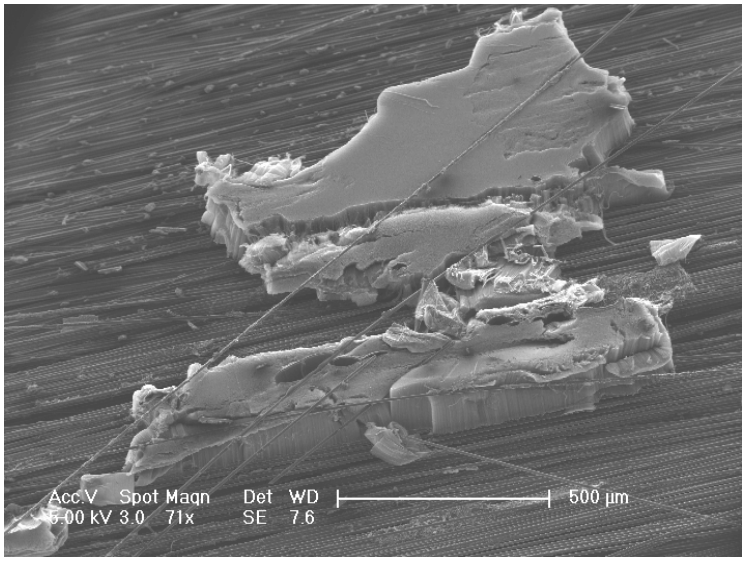

a)

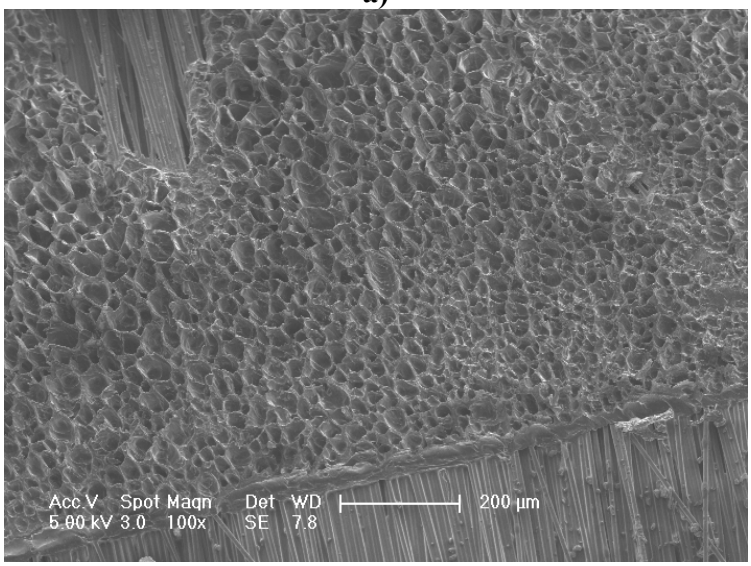

b)

Figure 4.12: Wetting of forests transplanted to the prepreg using the second testing method (CNTs in contact before heating the prepreg): a) Transplanted CNTs with wetting only at the base; b) Larger transplanted region of forest with CNTs completely wet and forming a regular honeycomb-like pattern.

As can be seen in Figure 4.12.b), the honeycomb structure was also present in the fully wet CNT forests, but in larger regions. Two close-ups of the honeycomb structure with thicker walls are shown in Figure 4.13. The walls are thicker than in the previous set of tests (~2 μm), ranging from 4 μm to almost 10 μm at some junctions.

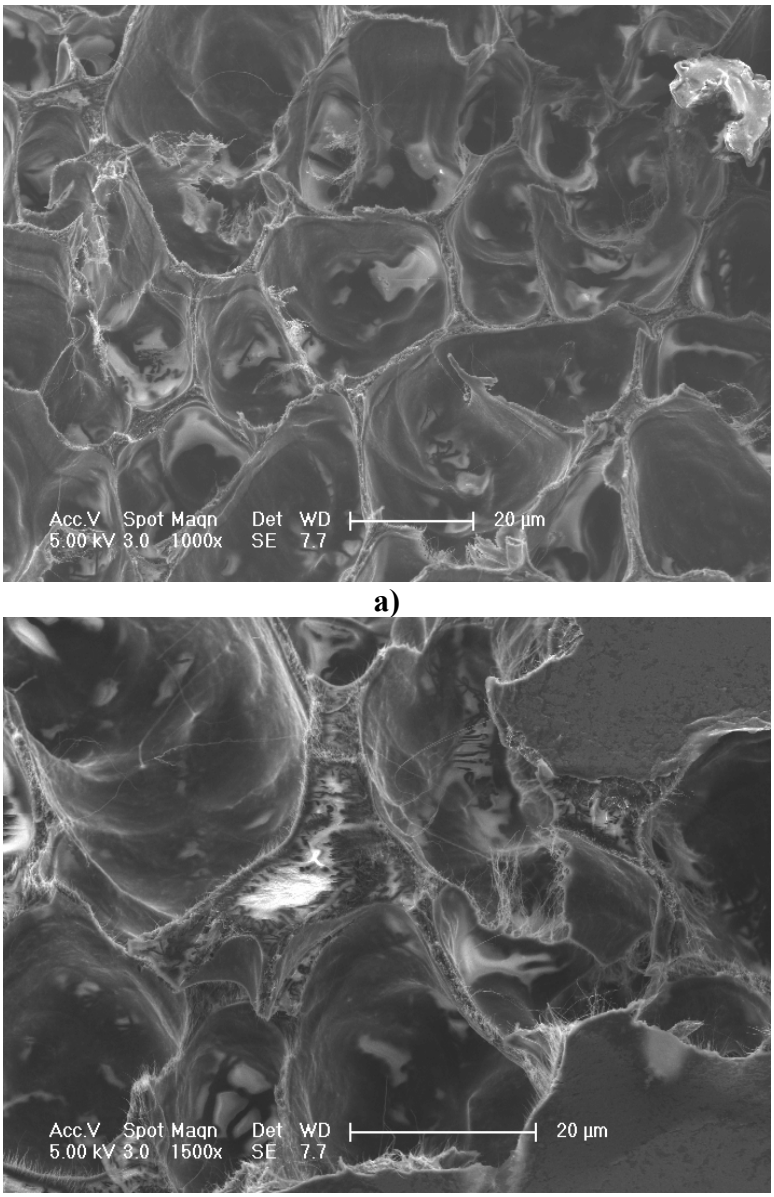

Figure 4.13: SEMs of a) completely wet CNTs creating honeycomb structures slightly thicker than in the previous set of tests (~4-5 μm); b) nanocomposite honeycomb region with maximum ~10-μm thick cell walls.

The adhesion of the wet CNTs to the prepreg layer is shown in Figure 4.14. The alignment of the CNTs is maintained, even if the contraction into the long CNT forest is strong enough to create the honeycomb structure.

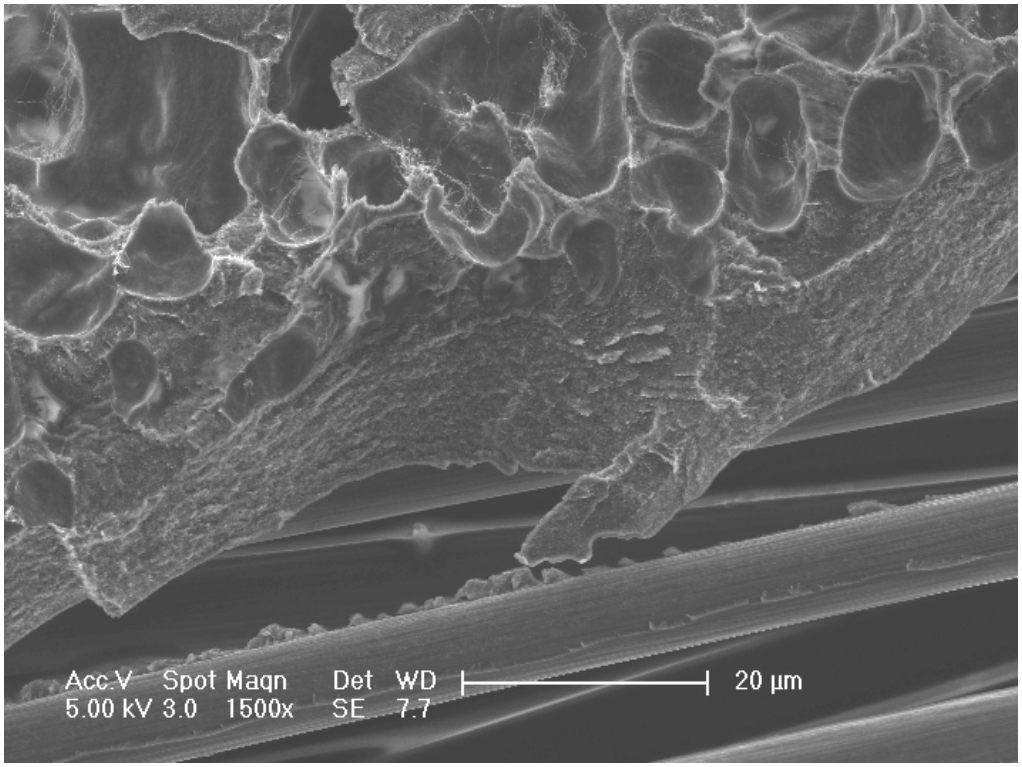

Figure 4.14: SEM of the interconnection of the nanocomposite and the fibers in the prepreg.

For this set of samples the wetting of the CNTs in some regions was effective enough to make the epoxy adhere to the catalyst so that the thin catalyst layer was separated from the wafer that originally contained the CNTs, as shown in Figure 4.15. Even if the adhesion of the catalyst layer is a proof of the effective wetting of the CNTs, it should be avoided in the fabrication process of the hybrid composites.

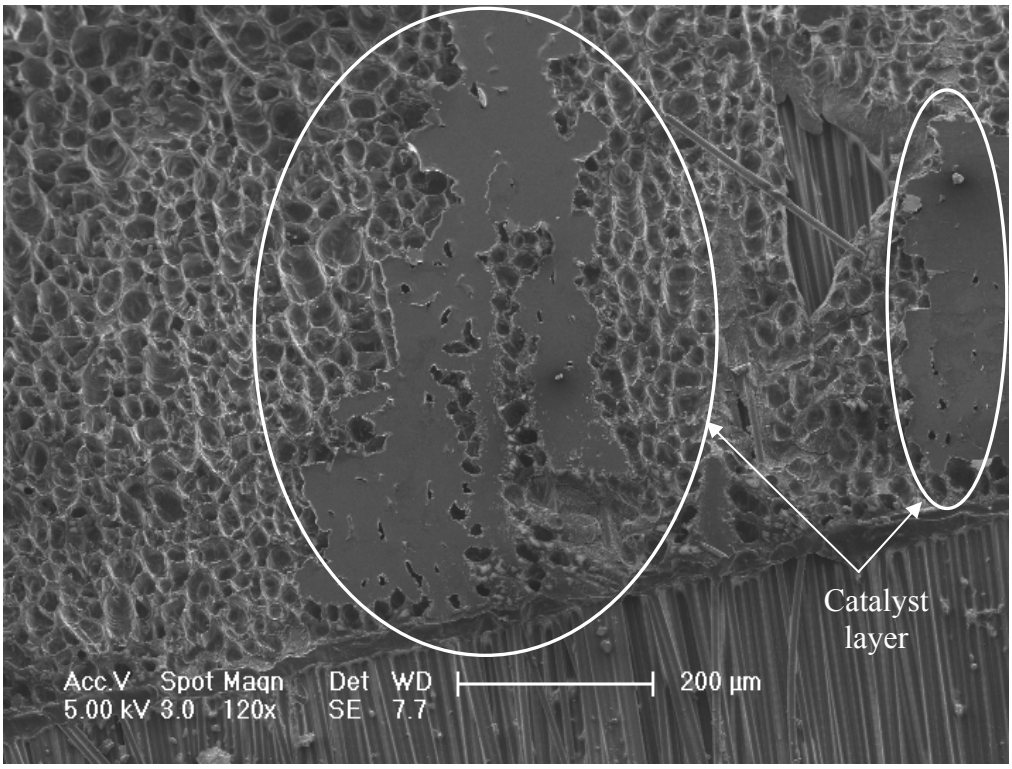

Figure 4.15: SEM of catalyst layer strongly adhered to the nanocomposite (and attached to the prepreg) and separated from the original Si substrate with this layer.

Initial Temperature: 95 ºC for 20 min; Curing Temperature: 140 ºC for 60 min.

For this set of samples the process was maintained the same as in the last set presented in the previous section, but with the initial temperature set to 95 ºC (maximum initial temperature recommended by the manufacturer). Again, the two characteristic regions (fully-wet, honey-combed CNTs and regions of CNTs wet at the base) appeared. The area of the regions transplanted was 20% higher than at the lower temperature, increasing to 70% of the total area of the original dense forest, and also the thickness of the walls (~15-30 µm) was greater, as shown in Figures 4.16 and 4.17. No catalyst layer was attached to the transplanted CNTs for these tests.

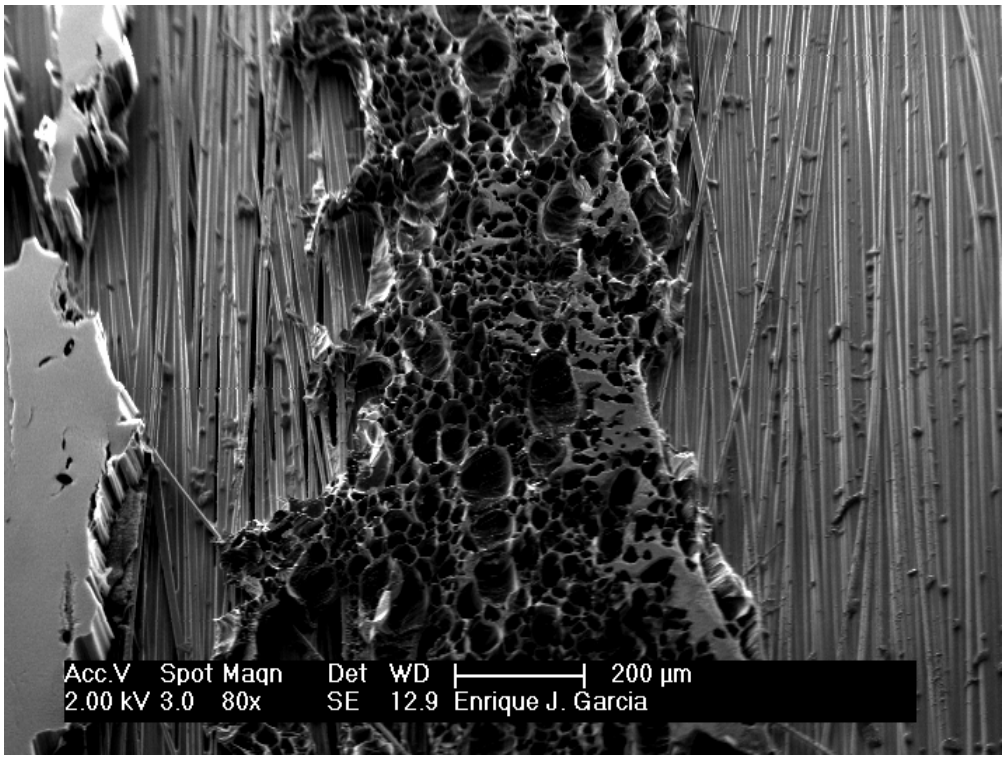

Figure 4.16: SEM of larger regions of transplanted CNTs: completely wet (center), and wet at the base, but not to the top of the CNTS (left region).

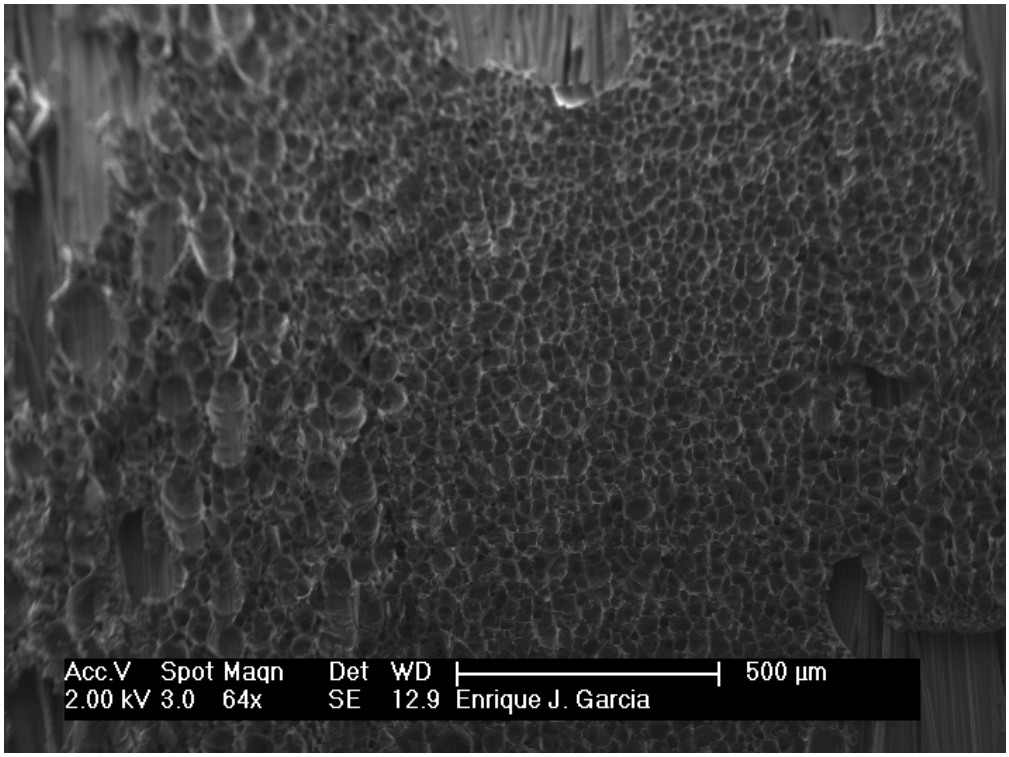

Figure 4.17: SEM of larger regions of completely wet transplanted CNT forming regularly spaced honeycomb structures.

The resulting hybrid composite, containing the CNT/epoxy honeycomb structure, was diesawed (using a DAD-2H/6T disco abrasive system). This technique allowed assessment of the effectiveness of the wetting of the CNTs (absence of voids inside the CNT/epoxy walls), as well as the adhesion of the CNTs to the prepreg tape. The disco abrasive system itself is very aggressive and poor adhesion between the prepreg and the CNT/epoxy walls would allow separation of the wet CNTs from the prepreg surface. In addition to the stresses generated during the cutting process, the cooling system of the equipment, based on water jets projected to the edge of the saw, also generates loads on the walls that may detach them from the substrate if the adhesion was not strong. As seen in Figure 4.18, however, the CNT/epoxy cell structure withstood the loads generated during the diesawing process, evidence of good adhesion to the prepreg tape.

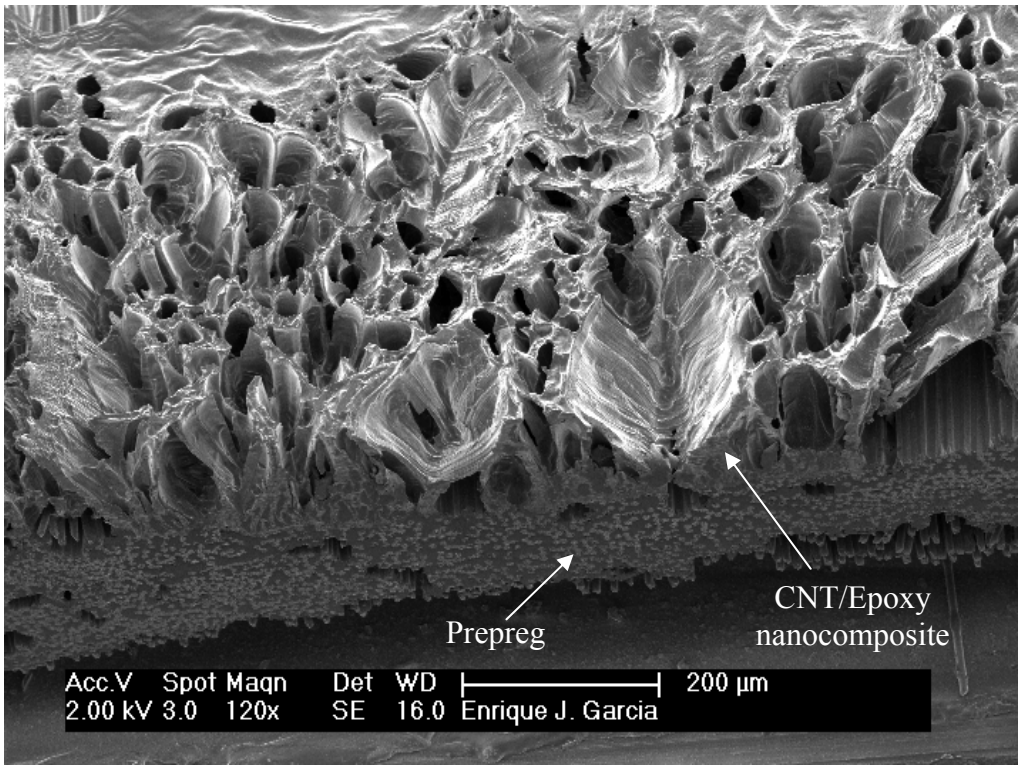

Figure 4.18: SEM of the hybrid composite cross section generated by the disco abrasive system. The fully wet CNT/epoxy honeycomb structure is well adhered to the prepreg ply.

Closer SEM images are shown in Figure 4.19. The CNT/epoxy walls are fully wet, and do not present any voids, showing good wetting. Note also that the CNT and prepreg regions are interpenetrating each other, as shown in Figure 4.19.b). This effect is believed to increase the effectiveness of the reinforcement in the hybrid architecture (CNT layer between two plies of prepreg).

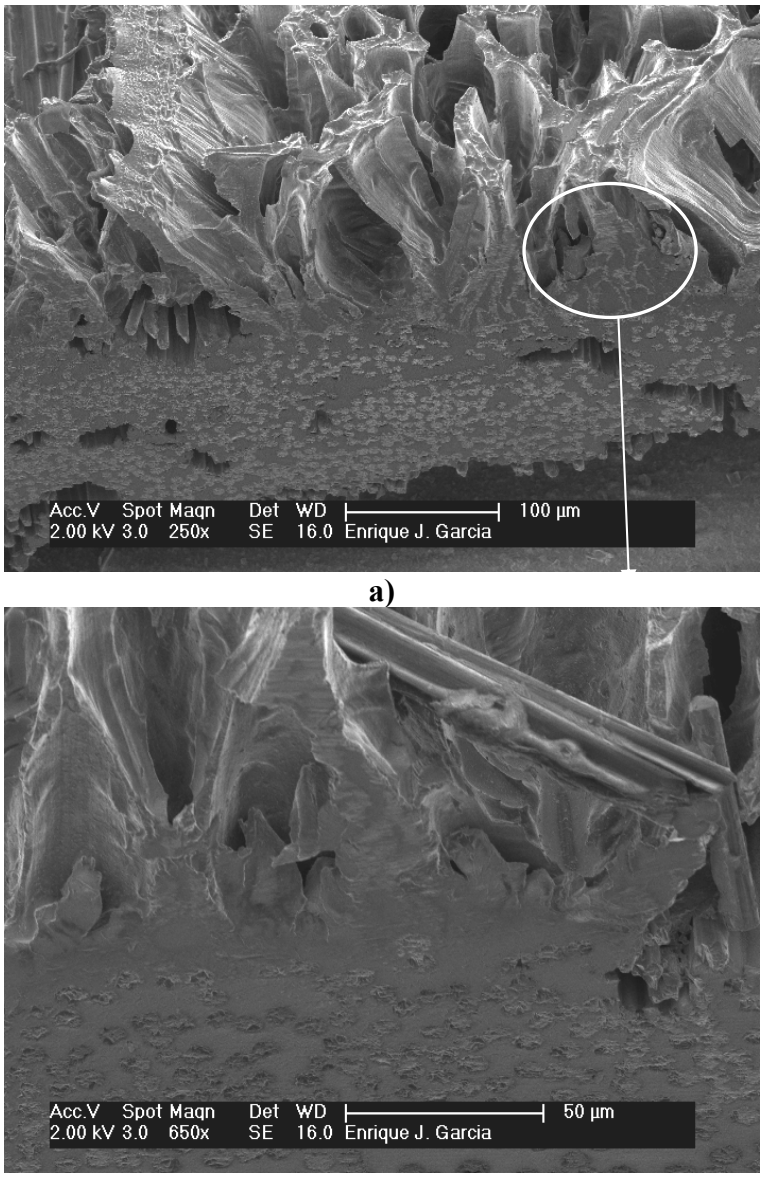

Figure 4.19: SEMS of a) Close-up of the diesawed region connecting the wet CNT honeycomb structure with the prepreg layer; b) Closer view of the region highlighted in a).

4.3.3 Summary

The results presented in this section have demonstrated wetting of aligned CNT forests by graphite/epoxy prepreg to forma true hybrid composite. Even with more severe conditions than the ones found in the fabrication of this architecture (long CNTs transplanted to only one prepreg ply, rather than between two), the wetting of the CNTs is excellent. Wetting is more effective when the CNTs are in contact with the prepreg before ramping up the temperature, which was shown to be a more effective process than heating the prepreg and putting the CNTs in contact afterwards (surface covered by transplanted CNTs 30% larger than using the lowest initial temperature). Using the highest initial temperature recommended by the manufacturer (95 ºC) provided even more effective wetting. Not only the area of transplanted fully wet CNTs was 20% larger than using the lowest initial temperature (85ºC), but also the honeycomb structure formed at 95ºC was more regularly distributed and had thicker walls. Importantly, the method that demonstrated the best wetting is the most similar to envisioned cure cycle for the hybrid composite using multiple prepreg layers with a CNT forest between each ply.

4.4 Summary of Hybrid Composites

After the preliminary tests presented in this work, the two hybrid architectures described earlier appear to be feasible for fabrication. For the first architecture, based on CNTs grown radially on the surface of advanced fibers, it was necessary to prove that the mechanical properties of the fibers were not deteriorated by the CVD growth process. As seen in section 4.2.2, the Young's modulus, the tensile strength and the strain-to-failure of the fibers are not changed after applying the catalyst, or after the growth process.

For the second hybrid architecture (vertically-aligned CNTs in between the plies of graphite/epoxy prepreg laminates), the most important factor to determine its feasibility is the effective wetting of the CNTs using the epoxy contained in the prepregs themselves. The reasons for this are two: First, by wetting the CNTs with the epoxy, the creation of an extra layer (and hence, an increase in the weight) can be avoided. Moreover, not adding extra epoxy to wet the CNTs favors the penetration of the CNTs in the ply structure, which should translate into increased bridging (nanostiching effect) of the matrix-rich region between plies.

In both cases mechanical tests at the macroscale will be necessary to demonstrate the effectiveness of the reinforcement obtained by adding CVD-grown CNTs to the composite material for the two architectures described.

Chapter 5. Conclusions and Recommendations

In this thesis, different composite architectures based on carbon nanotubes as reinforcement in polymer-matrix advanced composites were investigated. The focus of the project was to experimentally demonstrate the feasibility of the fabrication of nanocomposites (CNT/polymer) and hybrid composites (CNT/polymer/advanced fibers). Wetting of CNTs by several polymers, and mechanical characterization of the nanocomposites and advanced fibers with CNTs grown on their surface was investigated. The contributions made towards these goals are presented next, before recommendations for future research efforts are made.

5.1 Contributions

Contributions from this project towards realizing nano- and hybrid composites containing well-aligned, long, fast-grown CNTs can be divided into 7 areas:

1. A thorough analysis of the analytical and experimental results of the mechanical properties of pure CNTs was provided. Analytical and experimental results for the different nanocomposite and hybrid composite architectures based on CNT-reinforcement of polymers in the extant literature were also presented.

2. From the wide variety of different processes available to grow CNTs, the thermal CVD process was identified to be the most promising for structural applications for several reasons: First, the thermal CVD process reported in this work yields dense forests of well-aligned, long CNTs with a growth rate approaching 200 μm per minute, with advantages in growth rate, alignment and quality of the CNTs over those which have so far been utilized to create CNT-based composite materials (nanocomposites and hybrid composites). The existing growth rate of this process is considered to be high enough (and lengths of CNTs desired are small enough, ~5 μm) to scale-up the growth method into a continuous process and in the future to integrate it into the fabrication of composite materials, as shown in the patent developed during this research [115]. Second, due to the self-alignment of the CNTs produced during growth, the nanocomposites containing such CNTs overcome many of the problems traditionally associated with randomly oriented CNTs embedded in polymer matrices (especially dispersion and alignment). This work is the first to report the use of the thermal CVD process to grow CNTs as reinforcement for structural applications: reinforcement of polymers (nanocomposites) and two different architectures of hybrid composites.

3. Wetting of the CNTs grown with the thermal CVD process was addressed experimentally. This work is the first to report on wetting of CVD-grown well-aligned CNTs with commercial epoxies, including high-viscosity epoxies (no solvents added to reduce the viscosity of the polymer). Experimental results allowed identification of the most important parameters that play a role in the

effectiveness of the CNT wetting by polymers: Viscosity of the polymer matrix, method of introducing polymer to the CNTs used, volume fraction of the CNTs, and shape (presence of sharp corners) and dimensions (cross sectional area, and height) of the CNT pillars/forests to be wet. From the results, it is possible to determine that the issues related to dispersion and alignment for randomly oriented CNT-reinforced polymers can be effectively overcome for aligned thermal CVD-grown CNTs. Results for wetting using epoxies with different viscosities and curing times also showed that the wetting process is fast enough (100-μm CNT forests are wet by SU-8 in ~1 second) to allow the scalability of the CNT wetting process to a continuous fabrication process. In the most extreme case, a highly-viscous epoxy with a curing time of 20 minutes at room temperature (~7 minutes before solidification) was used, and as shown in section 3.3, the epoxy penetrated into the CNT pillars and reached a height of 80 μm, at least 2.5 times more than needed in the fabrication of the hybrid architectures described in chapter 4. The CNT wetting using epoxies with lower viscosities and longer curing times (longer times at low viscosity) is much faster, and more effective. The results obtained support the feasibility of continuous processes to fabricate nanocomposites and hybrid composites containing fully wet CNTs.

4. A new submersion wetting process (see Figure 3.8) was developed to increase the effectiveness of the wetting of CNTs using low viscosity epoxies. Using this method, the contraction due to the penetration of the epoxy through capillarity effects is better controlled, maintains the original pillar shape and CNT alignment inside the nanocomposite. Without this method, the fabrication of regularly

contracted pillars (see Figure 3.14, and Figure 3.48) used for mechanical testing would have not been possible.

5. Mechanical characterization of the nanocomposites fabricated with the two commercial epoxies (EpoThin and SU-8) was performed using a nanoindenter. Berkovich and spherical nanoindentation tests and a nanocompression test using a flat punch allowed direct experimental assessment of the reinforcement of the nanocomposites due to the addition of CNTs. The results are the first reported experimental direct measurements of mechanical properties of CVD-grown aligned CNT nanocomposites. The results obtained show effective reinforcement of the polymer matrix by adding well aligned CNTs. The regularity of the contraction and the alignment of the CNTs are improved with lower viscosity epoxies. Due to this fact, and as seen from the mechanical tests applied to these nanocomposites, nanocomposites created with matrices having lower viscosities also provide better reinforcement. The reinforcement is more effective for the SU-8 epoxy resin, with a lower viscosity than for the EpoThin. For CNT/SU-8 nanocomposites with 2% volume fraction of CNTs, the modulus increase is 220%. A volume fraction of 5% of CNTs (upper limit of reported volume fraction) is needed in the case of randomly oriented CNTs embedded into an epoxy resin to obtain a similar increase in modulus [124]. This is in agreement with the model developed by Odegard *et al.* [66], which showed that the reinforcement is 3 times more effective when the nanotubes are oriented in the direction of the load.

6. Two different hybrid architectures were explored using the thermal CVD-grown CNTs. The first architecture is based on the growth of CNTs on the surface of advanced fibers that would be subsequently wet with epoxy. The thermal CVD process used in this work generated CNTs on the fibers at least one order of magnitude longer than previously published results. This work is also the first one to report a complete analysis of the stability of the mechanical properties of fibers before and after the CVD growth process. The properties (Young's modulus, tensile strength, and strain-to-failure) are maintained after the CVD process, which confirms the viability of this hybrid architecture.

7. The second architecture investigated in this work places well-aligned CNTs on plies of a prepreg tape laminate. These CNTs are perpendicular to the plane of the laminate, reinforcing the matrix in the optimal direction. Other works have focused on the use of polymer films containing randomly oriented CNTs [138] or carbon nanofibers [91] placed between plies, with limited success. This is the first work to show experimental results on the feasibility of the fabrication of hybrid architectures based on long, well-aligned, CVD-grown CNTs.

5.2 Recommendations

Based on the contributions and the conclusions drawn from the current research, the following future research areas are identified:

1. The CVD process used in this work has a rapid growth rate (up to 200 μm/min) and it is highly reliable. However, it is not currently a capability to control easily the volume fraction of CNTs (set to around 0.9%) or the adhesion of the CNTs to the substrate (fairly weak). Further development in the CVD process should be focused on better understanding the CNT growth process to be able to tailor these two characteristics. The volume fraction could increase the reinforcement for the nanocomposite and hybrid composites. Controlling the catalyst deposition process could provide a better control over the final volume fraction of the nanotubes, and over their diameters and number of walls. Promising results have been reported in the literature to control the size [140], and spacing in the catalyst pattern using polymer films [141]-[142] and micro-printing deposition techniques [143]. Control of the adhesion of the CNTs to the substrate will also be crucial for the fabrication of hybrid architectures (good adhesion for the CNTs grown on the surface of fibers, reduced adhesion for the CNT forest to be placed between plies).

2. Initial results obtained in this research show that effective wetting of CVD grown CNTs is possible. For low viscosity resins it is also possible to control the contraction due to capillarity effects and also to maintain alignment of the CNTs. However, further knowledge of the wetting process is highly desirable. A high-

speed camera could help define the mechanisms and routes that occur during the wetting process. As mentioned in the previous paragraph, different volume fractions of CNTs should be tested to determine if the wetting is still possible with an increased amount of CNTs, and if it is, if the reinforcement is still effective. Also, different commercial epoxies used in composite applications (*e.g.*, RTM epoxies) should also be tested at different temperatures, including the temperatures used during the curing process.

3. The effective reinforcement of the CNT/epoxy nanocomposites tested in this work is around 220% using 2% volume fraction of CNTs. However, as seen in section 3.4.2, these results are far from the idealized rule-of-mixtures model. One of the factors that might be affecting the reinforcement is the adhesion between the CNTs and the epoxy resins [67]. Methods to functionalize the CNTs should, therefore, be studied to enhance reinforcement. Functionalization can also help minimize formation of CNT aggregates [26], and theoretically could help minimize the formation of voids and cell structures.

4. The pillars fabricated to perform compression tests contained a dome of CNT/epoxy nanocomposite that could not be microtomed. This dome was flattened during the compression tests, which impeded the analysis of the loading region of the load-depth curve. In order to analyze the loading region, two possible solutions could be explored: Applying a second compression test on the pillars tested successfully; and using focused ion beam (FIB) equipment to remove the dome from the nanocomposite pillar prior to testing.

5. In parallel to the development of new wetting tests, mechanical tests should be performed on the specimens fabricated using the two hybrid composite architectures described in chapter 4. Tests of immediate interest are:
   - For the architecture based on CNTs grown on the surface of fibers, single fiber fragmentation test (to determine the increase in interfacial shear strength), tensile tests on bundles of fibers containing CNTs and wet with epoxy, tensile tests of laminates, 3-point bending, and Mode I fracture tests.
   - For the architecture based on CNT forests placed between plies of a laminate, tensile tests of laminates, 3-point bending, and Mode I fracture tests should be performed.

6. The two architectures described in this work seem to be the most immediate and promising applications for the CVD-grown CNTs. However, there are other architectures that could also be interesting to explore (*e.g.*, films created by knocking over CNT pillars).

7. The fabrication of small specimens of hybrid composites is possible. However, the success of the hybrid composite architectures presented in this work depends on the scalability of the overall process and also on the compatibility with "traditional" composite materials manufacturing processes. Both the scalability and compatibility should be addressed in future studies. The furnace used in this work has a small diameter (22 mm) and is not prepared for continuous operation. A larger furnace, possibly with continuous processing capabilities, is envisioned to address issues as the controlled growth of CNT forests over larger areas, and

the continuous application of catalyst. Methods to continuously apply the catalyst, grow the CNTs, place the CNTs in contact with the prepreg (only for the second hybrid architecture presented), to wet, and finally to cure the hybrid composite should be developed taking into account the processes used to fabricate traditional composites and the results from this thesis.

8. Finally, the outstanding combination of mechanical, thermal, and electrical properties of CNTs has been discussed in chapter 2. Further studies should also focus on multifunctional applications that take full advantage of this combination of properties. CNT based hybrid architectures are envisioned to create a new generation of materials capable of performing two or more functions at the same time (*e.g.*, outer layers of the fuselage of airplanes with electrical conduction and damping capabilities). Tests should be developed and performed to assess this multifunctionality.

Bibliography

[1] S. Iijima, "Helicoidal microtubes of graphitic carbon," Nature 354 (1991), 56-58.

[2] E. T. Thostenson, Z. Reng, and T. Chou, "Advances in the science and technology of carbon nanotubes and their composites: a review," Composites Science and Technology 61 (2001), 1899-1912.

[3] E. T. Thostenson, C. Li, and T.-W. Chou, "Nanocomposites in context," Composites Science and Technology 65 (2005) 491–516.

[4] R. Z. Ma, J. Wu, B. Q. Wei, J. Liang, and D. H. Wu, "Processing and properties of carbon nanotubes-nano-SiC ceramic," Journal of Materials Science 33 21 (1998), 5243–5246.

[5] X. Chen, J. Xia, J. Peng, W. Li, and S. Xie, "Carbon-nanotube metal-matrix composites prepared by electronless plating," Composites Science and Technology 60 2 (2000), 301–306.

[6] C. L. Xu, B.Q. Wei, R. Z. Ma, J. Liang, X. K. Ma, and D. H. Wu, "Fabrication of aluminum-carbon nanotube composites and their electrical properties," Carbon 37 5 (1999), 855–858.

[7] D. S. Bethune, C. H. Kiang, M. S. Devries, G. Gorman, R. Savoy, J. Vazquez *et al.*, "Cobalt-catalyzed growth of carbon nanotubes with single-atomic-layer walls," Nature 363 (1993), 605–607.

[8] C. Journet, W. K. Maser, P. Bernier, A. Loiseau, M. L. de la Chapelle, and S. Lefrant, "Large-scale production of single-walled carbon nanotubes by the electric-arc technique," Nature 388 (1997), 756–758.

[9] Z. Shi, Y. Lian, F.H. Liao, X. Zhou, Z. Gu, and Y. Zhang., "Large scale synthesis of single-wall carbon nanotubes by arc discharge method," Journal of Physics and Chemistry of Solids 61 7 (2000), 1031–1036.

[10] A. G. Rinzler, J. Liu, H. Dai, P. Nikolaev, C. B. Fuman, and F. J. Rodriguez-Macias, "Large-scale purification of single-wall carbon nanotubes: Process, product and characterization," Applied Physics A 67 1 (1998), 29–37.

[11] Y. Zhang and S. Iijima, "Formation of single-wall carbon nanotubes by laser ablation of fullerenes at low temperatures," Applied Physics Letters 75 20 (1999), 3087–3089.

[12] P. Nikolaev, M.J. Bronikowski, R.K. Bradley, F. Fohmund, D.T. Colbert, and K.A. Smith, "Gas-phase catalytic growth of single-walled carbon nanotubes from carbon monoxide," Chemical Physics Letters 313 1-2 (1999), 91–97.

[13] M. Ge and K. Sattler, "Bundles of carbon nanotubes generated by vapor-phase growth," Applied Physics Letters 64 6 (1994), 710–711.

[14] Z. F. Ren, Z. P. Huang, J. W. Xu, D. Z. Wang, J. G. Wen, and J. H. Wang, "Growth of a single freestanding multiwall carbon nanotube on each nanonickel dot," Applied Physics Letters 75 8 (1999), 1086–1088.

[15] Z. F. Ren, Z. P. Huang, J. W. Xu, J. H. Wang, P. Bush, and M. P. Siegal, "Synthesis of large arrays of well-aligned carbon nanotubes on glass," Science 282 (1998), 1105–1107.

[16] Z. P. Huang, J. W. Xu, Z. F. Ren, J. H. Wang, M. P. Siegal, and P.N. Provencio, "Growth of highly oriented carbon nanotubes by plasma-enhanced

hot filament chemical vapor deposition," Applied Physics Letters 73 26 (1998), 3845–3847.

[17] G. Che, B. B. Lakshmi, C. R. Martin, E. R. Fisher, and R. S. Ruoff, "Chemical vapor deposition based synthesis of carbon nanotubes and nanofibers using a template method," Chemistry of Materials 10 1 (1998), 260–267.

[18] W. Z. Li, S. S. Xie, L. X. Qian, B. H. Chang, B. S. Zou, and W. Y. Zho, "Large-scale synthesis of aligned carbon nanotubes," Science 274 (1996), 1701–1703.

[19] P. G. Collins and P. Avouris, "Nanotubes for electronics," Scientific American 283 6 (2000), 62–69.

[20] T. Rueckes, K. Kim, E. Joselevich, G.Y. Tseng, C.-L. Cheung, and C.M. Lieber, "Carbon nanotube-based nonvolatile random access memory for molecular computing," Science 289 (2000), 94–97.

[21] R. S. Ruoff and D.C. Lorents, "Mechanical and thermal-properties of carbon nanotubes," Carbon 33 7 (1995), 925–930.

[22] J. P. Lu, "Elastic properties of single and multilayered nanotubes," Journal of the Physics and Chemistry of Solids 58 11 (1997), 1649–1652.

[23] R. Al-Jishi and G. Dresselhaus, "Lattice dynamical model for graphite," Physical Review B 26 8 (1982), 4514–4522.

[24] M. M. J. Treacy, T. W. Ebbesen, and T. M. Gibson, "Exceptionally High young's modulus observed for individual carbon nanotubes," Nature 381 (1996), 680–687.

[25] E. W. Wong, P. E. Sheehan, and C. M. Lieber, "Nanobeam mechanics: elasticity, strength, and toughness of nanorods and nanotubes," Science 277 (1997), 1971–1975.

[26] J. P. Salvetat, G. A. D. Briggs, J. M. Bonard, R. R. Bacsa, A. J. Kulik, and T. Stöckli, "Elastic and shear moduli of single-walled carbon nanotube ropes," Physical Review Letters 82 5 (1999), 944–947.

[27] M. F. Yu, O. Lourie, M. Dyer, K. Moloni, and T. Kelly, "Strength and breaking mechanism of multi-walled carbon nanotubes under tensile load," Science 287 (2000), 637–640.

[28] H. J. Qi, K. B. K. Teo, K. K. S. Lau, M. C. Boyce, W. I. Milne, J. Robertson, and K.K. Gleason, "Determination of mechanical properties of carbon nanotubes and vertically aligned carbon nanotube forests using nanoindentation," J. Mech. Phys. Solids 51 (2003), 2213 – 2237.

[29] B. I. Yakobson, C. J. Brabec, and J. Bernholc, "Nanomechanics of carbon tubes: instabilities beyond linear response," Phys. Rev. Lett. 76 14 (1996), 2511–2514.

[30] A. Pantano, M. C. Boyce, and D. M. Parks, "Mechanics of deformation of single and multiwalled carbon nanotubes," J. Mech. Phys. Solids 52 4 (2004), 789-821.

[31] Y. Saito, T. Yoshikawa, S. Bandow, M. Tomita, and T. Hayashi, "Interplayer spacing in carbon nanotubes," Phys. Rev. B 48 3 (1993), 1907–1909.

[32] X. Sun, C. H. Kiang, M. Endo, K. Takeuchi, T. Furuta, and M. S. Dresselhaus, "Stacking characteristics of graphene shells in carbon nanotubes," Phys. Rev. B 54 18 (1996), 12629–12632.

[33] C. H. Kiang, M. Endo, P. M. Ajayan, G. Dresselhaus, and M. S. Dresselhaus, "Size effects in Carbon Nanotubes," Phys. Rev. Lett. 81 9 (1996), 1869–1872.

[34] J. Cumings and A. Zettl, "Low friction nanoscale linear bearing realized from multiwall carbon nanotubes," Science 289 (2000), 602–604.

[35] M. F. Yu, B. I. Yakobson, and R. S. Ruo, “Controlled sliding and pullout of nested shells in individual multiwalled carbon nanotubes,” J. Phys. Chem. B 104 (2000), 8764–8767.

[36] P. Poncharal, Z. L. Wang, D. Ugarte, and W. A. de Heer, “Electrostatic dejections and electromechanical resonances of carbon nanotubes,” Science 283 (1999), 1513–1516.

[37] J. P. Lu, “Elastic properties of carbon nanotubes and nanoropes,” Phys Rev Lett 79 7 (1997), 1297–300.

[38] C. Y. Li and T. W. Chou, “Elastic properties of single-walled carbon nanotubes in transverse directions,” Phys Rev B 69 (2004), 073401.

[39] C. Y. Li and T. W. Chou, “A structural mechanics approach for the analysis of carbon nanotubes,” Int J Solids Struct 40 (2003), 2487–99.

[40] B. H. Bodily and C. T. Sun, “Structural and equivalent continuum properties of single-walled carbon nanotubes,” Int J Mater Product Technol 18 4–6 (2003), 381–397.

[41] B. I. Yakobson, M. P. Campbell, C. J. Brabec, and J. Bernholc, “High strain rate fracture and C-chain unraveling in carbon nanotubes,” Comput Mater Sci 8 4 (1997), 341–348.

[42] T. Belytschko, S. P. Xiao, G. C. Schatz, and R. S. Ruoff, “Atomistic simulations of nanotube fracture,” Phys Rev B 65 23 (2002), 235430.

[43] B. I. Yakobson, G. Samsonidze, and G. G. Samsonidze, “Atomistic theory of mechanical relaxation in fullerene nanotubes,” Carbon 38 (2000), 1675–1680.

[44] M. F. Yu, B. S. Files, S. Arepalli, and R. S. Ruoff, “Tensile loading of ropes of single wall carbon nanotubes and their mechanical properties,” Physical Review Letters 84 24 (2000), 5552–5555.

[45] S. Xie, W. Li, Z. Pan, B. Chang, and L. Sun, "Mechanical and physical properties on carbon nanotube," Journal of Physics and Chemistry of Solids 61 7 (2000), 1153–1158.

[46] R. Andrews, D. Jacques, A.M. Rao, T. Rantell, F. Derbyshire, and Y. Chen. Nanotube composite carbon fibers. Applied Physics Letters 75 9 (1999), 1329–1331.

[47] B. Vigolo, P. Poulin, M. Lucas, P. Launois, and P. Bernier, "Macroscopic fibers and ribbons of oriented carbon nanotubes," Applied Physics Letters 81 No. 7 (2002), 1210–1212.

[48] H. Ye, H. La, N. Titchenal, Y. Gogotsi, and F. Ko, "Reinforcement and rupture behavior of carbon nanotubes-polymer nanofibers," Applied Physics Letters 85 No. 10 (2004), 1775-1777.

[49] J. Njuguna and K. Pielichowski, "Polymer nanocomposites for Aerospace Applications: Properties," Advanced Engineering Materials 5 11 (2003), 769-778.

[50] J. Njuguna and K. Pielichowski, "Polymer nanocomposites for Aerospace Applications: Characterization," Advanced Engineering Materials 6 4 (2004), 204-210.

[51] X. Xu M. M. Thwe, C. Shearwood, K. Liao. Mechanical properties and interfacial characteristics of carbon-nanotube-reinforced epoxy thin films," Applied Physics Letters 81 No. 15 (2002), 2833-2835.

[52] L. S. Schadler, S. C. Giannaris, and P.M. Ajayan, "Load transfer in carbon nanotube epoxy composites," Applied Physics Letters 73 26 (1998), 3842–3844.

[53] C. Wei, K. Cho, and D. Srivastava, "Chemical bonding of polymer on carbon nanotube," Materials Research Society Symposium Proceedings 675 (2001), W.4.7.1-5.

[54] H.D. Wagner, O. Lourie, Y. Feldman, and R. Tenne, "Stress-induced fragmentation of multiwall carbon nanotubes in a polymer matrix," Applied Physics Letters 72 2 (1998), 188–190.

[55] O. Lourie and H.D. Wagner. Transmission electron microscopy observations of fracture of single-wall carbon nanotubes under axial tension," Applied Physics Letters 73 24 (1998), 3527–3529.

[56] O. Lourie and H. D. Wagner, "Evidence of stress transfer and formation of fracture clusters in carbon nanotube-based composites," Composites Science and Technology 59 6 (1999), 975–977.

[57] A. H. Barber, S. R. Cohen, S. Kenig, and H. D. Wagner, "Interfacial fracture energy measurements for multi-walled carbon nanotubes pulled from a polymer matrix," Composite Science and Technology 64 15 (2004), 2283-2289.

[58] D. Qian, E. C. Dickey, R. Andrews, and T. Rantell, "Load transfer and deformation mechanisms in carbon nanotube-polystyrene composites," Applied Physics Letters 76 20 (2000), 2868–2870.

[59] E. T. Thostenson and T. W. Chou, "Aligned multi-walled carbon nanotube-reinforced composites: processing and mechanical characterization," Applied Physics 35 (2002), L77-L80.

[60] M. S. P. Shaffer and A. H. Windle, "Fabrication and characterization of carbon nanotube/poly (vinyl alcohol) Composites," Advanced Materials 11 (1999), 937–941.

[61] G. G. Tibbetts and J. McHugh, “Mechanical properties of vapor-grown carbon fiber composites with thermoplastic matrices,” Journal of Materials Research 14 (1999), 2871.

[62] Z. Jia, Z. Wang, C. Xu, J. Liang, B. Wei, and D. Wu, “Study on poly(methyl methacrylate)/carbon nanotube composites,” Materials Science and Engineering A 271 1–2 (1999), 395–400.

[63] V. Lordi and N. Yao, “Molecular mechanics of binding in carbon-nanotube-polymer composites,” Journal of Materials Research 15 12 (2000), 2770–2779.

[64] P. M. Ajayan, L. S. Schadler, C. Giannaris, and A. Rubio, “Single-walled nanotube-polymer composites: strength and weaknesses,” Advanced materials 12 10 (2000), 750–753.

[65] L. Jin, C. Bower, and O. Zhou, “Alignment of carbon nanotubes in a polymer matrix by mechanical stretching,” Applied Physics Letters 73 9 (1998), 1197–1199.

[66] G. M. Odegard, T. S. Gates, K. E. Wise, C. Park, and E. J. Siochi, “Constitutive modeling of nanotube-reinforced composites,” Composites Science and Technology 63 (2003), 1671-1687.

[67] S. Frankland, A. Caglar, D. W. Brenner, and M. Griebel, “Reinforcement mechanisms in polymer nanotube composites: simulated non-bonded and cross-linked systems,” MRS Fall Meeting, Boston, MA (2000).

[68] R. J. Chen, Y. Zhang, D. Wang, and H. Dai, “Noncovalent sidewall functionalization of single-walled carbon nanotubes for protein immobilization,” Journal of the American Chemical Society 123 (2001), 3838–3839.

[69] A. Star, J. F. Stoddart, D. Steuerman, M. Diehl, A. Boukai, and E. W. Wong, “Preparation and properties of polymer-wrapped singlewalled carbon

nanotubes," Angewandte Chemie International Edition in English 40 9 (2001), 1721–1725.

[70] A. Dufresne, M. Paillet, J. L. Putaux, R. Canet, F. Carmona, and P. Delhaes, "Processing and characterization of carbon nanotube/poly(styrene-co-butyl acrylate) nanocomposites," Journal of Materials Science 37 (2002), 3915-3923.

[71] A. Miravete, P. Laborde-Lahoz, W. Maser, T. Martínez, A. Benito, T. Seeger, P. Cano, and R. Guzmán de Villoria, "Mechanical Characterization of Carbon Nanotube Composite Materials," Mechanics of Advanced Materials and Structures 12 (2005), 1-7.

[72] M. C. Paiva, B. Zhou, K. A. S. Fernando, Y. Lin, J. M. Kennedy, and Y.-P. Sun, "Mechanical and morphological characterization of polymer-carbon nanocomposites from functionalized carbon nanotubes," Carbon 42 (2004), 2849-2854.

[73] F. H. Gojny, M. H. G. Wichmann, U. Köpke, B. Fiedler, and K. Schulte, "Carbon nanotube-reinforced epoxy-composites: enhanced stiffness and fracture toughness at low nanotube content," Composites Science and Technology 64 (2004), 2363-2371.

[74] S. G. Kim, Z. F. Ren W. Z. Li, T. A. El-Aguizy, J. Y. Jeong, and Y. B. Jeon, "Transplanting carbon nanotubes," Applied Physics Letters 85 24 (2004), 5995-5997.

[75] J. F. Waters, L. Riester, M. Jouzi, P. R. Guduru, and J. M. Xu, "Buckling instabilities in multiwalled carbon nanotubes under uniaxial compression," Applied Physics Letters 85 (2004), 1787.

[76] C. Poe, J. R. Reeder, and F. G. Yuan, "Fracture Behavior of a Stitched Warp-Knit Carbon Fabric Composite," NASA/TM-2001-210868 (2001).

[77] E. H. Glaessgen, I. S. Raju, and C. C. Poe, “Modeling the influence of stitching on delamination growth in stitched warp-knit composite lap joints,” NASA Langley Research Center, Hampton, VA, 23681.

[78] E. H. Glaessgen and I. S. Raju, “Three-dimensional effects in the plate element analysis of stitched textile composites,” Proceedings of the 40th AIAA/ASME/ASCE/AHS/ASC Structures, Structural Dynamics, and Materials Conference and Exhibit St. Louis, Missouri (1999), AIAA-99-1416.

[79] P. B. Stickler, M. Ramulu, “Investigation of mechanical behaviour of transverse stitched T-joints with PR520 resin in flexure and tension,” Composite Structures 52 (2001), 307-314.

[80] P. B. Stickler and M. Ramulu, “Parametric analyses of stitched composite T-joints by the finite element method,” Materials and Design 23 (2002), 751–758.

[81] L. E. Stanley and D. O. Adams, “Development and Evaluation of Stitched Sandwich Panels,” NASA/CR-2001-211025 (2001).

[82] R. Krueger and T. K. O'Brien, “A shell/3d modeling technique for the analysis of delaminated composite laminates,” Nasa Langley Research Center.

[83] C. G. Dávila, “Solid-To-Shell Transition Elements for the Computation of Interlaminar Stresses,” Computing Systems in Engineering 5 2 (1994), 193-202.

[84] A. J. Hart, A. H. Slocum, and L. Royer, “Growth of conformal single-walled carbon nanotube films from Mo/Fe/Al_2O_3 deposited by electron beam evaporation,” Carbon 44 (2006) 348–359.

[85] L. X. Zheng, M. J. O’Connell, S. K. Doorn, X. Z. Liao, Y. H. Zhao, E. A.Akhadov, M. A. Hoffbauer, B. J. Roop, Q. X. Jia, R. C. Dye, D. E. Peterson,

S.M. Huang, J. Liu, and Y. T. Zhu, "Ultralong single-wall carbon nanotubes," Nature Materials 3 (2004), 673-676. Letters.

[86] C. J. Lee, D. W. Kim, T. J. Lee, Y. C. Choi, Y. S. Park, Y. H. Lee, W. B. Choi, N. S. Lee, G.-S. Park, and J. M. Kim, "Synthesis of aligned carbon nanotubes using thermal chemical vapor deposition," Chemical Physics Letters 312 (1999), 461–468.

[87] M. Meyyappan, L. Delzeit, A. Cassell, and D. Hash, "Carbon nanotube growth by PECVD: a review," Plasma Sources Sci. Technol. 12 (2003), 205-216.

[88] B. G. Demczyk, Y. M. Wang, J. Cumings, M. Hetman, W. Han, A. Zettl, and R. O. Ritchie, "Direct mechanical measurement of the tensile strength and elastic modulus of multiwalled carbon nanotubes," Materials Science and Engineering A 334 (2002), 173–178.

[89] S. Govindjee and J. L. Sackman, "On the use of continuum mechanics to estimate the properties of nanotubes," Solid State Communications 110 (1999), 227–230.

[90] A. B. Dalton, S. Collins, E. Muñoz, J. M. Razal, V. H. Ebron, J. P. Ferraris, J. N. Coleman, B. G. Kim, and R. H. Baughman, "Super-tough carbon-nanotube fibres," Nature 423 (2003), 703.

[91] Y. Dzenis, "Spinning Continuous Fibers for Nanotechnology," Science 304 (2004), 1917-1919.

[92] Y. A. Dzenis and G. Larsen, "Delamination resistant composites prepared by small diameter fiber reinforcement at ply interfaces," U.S. patent pending (2001) 6,265,333.

[93] H. W. Zhu, C. L. Xu, D. H. Wu, B. Q. Wei, R. Vajtai, and P. M. Ajayan, "Direct Synthesis of Long Single-Walled Carbon Nanotube Strands," Science 296 (2002), 884-886.

[94] M. Zhang, K. R. Atkinson, and R. H. Baughman, "Multifunctional Carbon Nanotube Yarns by Downsizing an Ancient Technology," Science 306 (2004), 1358-1361.

[95] M. Zhang, S. Fang, A. A. Zakhidov, S. B. Lee, A. E. Aliev, C. D. Williams, K. R. Atkinson, and R. H. Baughman, "Strong, Transparent, Multifunctional, Carbon Nanotube Sheets," Science 309 (2005), 1215-1219.

[96] S. Kumar, T. D. Dang, F. E. Arnold, A. R. Bhattacharyya, B. G. Min, X. Zhang, R. A. Vaia, C. Park, W. W. Adams, R.H. Hauge, R. E. Smalley, S. Ramesh, and P. A. Willis, "Synthesis, Structure, and Properties of PBO/SWNT Composites," Macromolecules (2002), 35, 9039-9043.

[97] Y.-L. Li, I. A. Kinloch, and A. H. Windle, "Direct Spinning of Carbon Nanotube Fibers from Chemical Vapor Deposition Synthesis," Science 304 (2004), 276-278.

[98] N. A. Koratkar, B. Wie, and P. M. Ajayan, "Multifunctional Structural Reinforcement featuring carbon nanotubes films," Composites Science and Technology 63 (2003), 1525-1531.

[99] B. J. Hinds, N. Chopra, T. Rantell, R. Andrews, V. Gavalas, and L. G. Bachas, "Aligned Multiwalled Carbon Nanotube Membranes," Science 303 (2004), 62-65.

[100] C. Bower, W. Zhu, S. Jin, and O. Zhou, "Plasma-induced alignment of carbon nanotubes," Applied Physics Letters 77 6 (2000), 830.

[101] Z.-G. Zhao, L.-J. Ci, H.-M. Cheng, and J.-B. Bai, "The growth of multi-walled carbon nanotubes with different morphologies on carbon fibers," Carbon 43 (2005) 663-665.

[102] L. J. Ci, Z. G. Zhao, and J. B. Bai, "Direct growth of carbon nanotubes on the surface of ceramic fibers," Carbon 43 (2005) 883-886.

[103] R. Saha and W. D. Nix, "Effects of the substrate on the determination of thin film mechanical properties by nanoindentation," Acta Materialia 50 (2002) 23–38.

[104] S. Zhu, C.-H. Su, S. L. Lehoczky, I. Muntele, and D. Ila, "Carbon nanotubes growth on carbon fibres," Diamond and Related Materials 12 (2003) 1825–1828.

[105] M. F. De Riccardis, D. Carbone, T. Dikonimos Makris, R. Giorgi, N. Lisi, and E. Salernitano, "Anchorage of carbon nanotubes grown on carbon fibres," Carbon 44 (2006), 671-674.

[106] E. T. Thostenson, W. Z. Li, D. Z. Wang, and Z. F. Ren, and T. W. Chou, "Carbon nanotubes/carbon fiber hybrid multiscale composites," Journal of Applied Physics 9 (2002), 6034-6037.

[107] R. H. Baughman, A. A. Zakhidov, and W. A. de Heer, "Carbon Nanotubes – The Route Toward Applications," Science 297 (2002), 787-792.

[108] D.-M. Yoon, B.-J. Yoon, K.-H. Lee, H. Seok Kim, and C. G Park, "Synthesis of carbon nanotubes from solid carbon sources by direct microwave irradiation," Carbon 44 7 (2006), 1339-1343.

[109] A. J. Hart, and A. H. Slocum, "Nucleation, Rapid Growth, and Mechanical Stability of Millimeter-Scale Aligned Carbon Nanotube Structures Growth by Thermal CVD at Atmospheric Pressure," Journal of Physical Chemistry B. Submitted for publication (2005).

[110] A. J. Hart, A. H. Slocum, and L. Royer, "Growth of conformal single-walled carbon nanotubes films from Mo/Fe/Al_2O_3 deposited by electron beam evaporation," Carbon, in press, (2005).

[111] A. J. Hart and A. H. Slocum, "Flow-mediated nucleation and rapid growth of millimeter-scale aligned carbon nanotube structures from a thin-film catalyst," J. Physical Chemistry B, vol. 110, no.16, pp. 8250-8257, 2006.

[112] B. Q. Wei, R. Vajtai, Y. Jung, J. Ward, R. Zhang, G. Ramanath, and P. M. Ajayan , "Assembly of Highly Organized Carbon Nanotube Architectures by Chemical Vapor Deposition," Chem. Mater 15 (2003), 1598-1606.

[113] M. F. Ashby. *Materials Selection for Mechanical Design.* Ed. 2. Amsterdam, Boston, Elsevier Butterworth-Heinemann (1999).

[114] T. L. Anderson, *Fracture Mechanics: Fundamentals and Applications*, Ed.2. Boca Raton, FL : Taylor & Francis (1994).

[115] E. J. García, A. J. Hart, A. H. Slocum, and B. L. Wardle, "Production of Reinforced Composite Materials and Aligned Carbon Nanotubes," MIT TLO Case 12029 (2005).

[116] W. K. Chu, J. W. Mayer, and M. A. Nicolet, *Backscattering spectrometry,* Academic Press, New York (1978).

[117] E. J. García, A. J. Hart, B. L. Wardle, and A. H. Slocum. Fabrication and Testing Of Long Carbon Nanotubes Grown On the Surface of Fibers for Hybrid Composites. Proceedings of 47th AIAA/ASME/ASCE/AHS/ASC Structures, Structural Dynamics, and Materials Conference (2005), AIAA-2006-1854.

[118] S. Fan, M. G. Chapline, N. R. Franklin, T. W. Tombler, A. M. Cassell, and H. Dai. "Self-Oriented Regular Arrays of Carbon Nanotubes and Their Field Emission Properties," Science 283 (1999), 512.

[119] ASTM C 1557 – 03, "Standard Test Method for Tensile Strength and Young's Modulus of Fibers," ASTM International (2003).

[120] E. G. Harlow and L. Phoenix, "The Chain-of-Bundles Probability Model for the Strength of Fibrous Materials," Journal of Composite Materials, 12, 1978.

[121] N. Chakrapani, B. Wei, A. Carrillo, P. M. Ajayan, and Ravi S. Kane, "Capillarity-driven assembly of two-dimensional cellular carbon nanotube foams," PNAS 101 (2004), 4009-4012.

[122] ASTM D 4018 – 99 (Reapproved 200, "Standard Test Methods for Properties of Continuous Filament Carbon and Graphite Fiber Tows," ASTM International (2004).

[123] B. L. Wardle and S. G. Kim, "Nano-engineered material architectures: Ultra-tough hybrid nanocomposite system," MIT TLO Case 11260 (2005).

[124] X. Li, H. Gao, W. A. Scrivens, D. Fei, X. Xu, M. A. Sutton, A. P. Reynolds, and M. L. Myrick, "Nanomechanical characterization of single-walled carbon nanotube reinforced epoxy composites," Nanotechnology 15 (2004) 1416–1423.

[125] X. Li and B. Bhushan, "A review of nanoindentation continuous stiffness measurement technique and its applications," Materials Characterization 48 (2002), 11–36.

[126] B. Bhushan and X. Li, "Nanomechanical characterisation of solid surfaces and thin films," International Materials Review 48 (2003), 125–64.

[127] W. C. Oliver and G. M. Pharr, "An Improved Technique for Determining Hardness and Elastic Modulus Using Load and Displacement Sensing Indentation Experiments," Journal of Materials Research 7 (2003), 1564–83.

[128] I. N. Sneddon, "The relation between load and penetration in the axisymmetric Boussinesq problem for a punch of arbitrary profile," International Journal of Engineering Science 3 (1965), 47–56.

[129] W. Fang, H-Y Chu, W-K Hsu, T-W Cheng, and N-H Tai, "Polymer-Reinforced, Aligned Multiwalled Carbon Nanotube Composites for Microelectromechanical Systems Applications," Adv. Mater. 2005, 17, 2987–2992.

[130] D. Newey, M. A. Wilkins, and H. M. Pollock, "An ultra-low-load penetration hardness tester," Journal of Physics E (1982), 119-122.

[131] http://www.micromaterials.co.uk/

[132] A. C. Fischer-Cripps, *Nanoindentation*, Mechanical engineering series. (Berlin, Germany). Springer, 2004.

[133] A. Gilat, R. K. Goldberg, and G. D. Roberts, "Strain Rate Sensitivity of Epoxy Resin in Tensile and Shear Loading," NASA/TM—2005-213595 (2005).

[134] J .R. Greer and W. D. Nix, "Size dependence of mechanical properties of gold at the sub-micron scale," Appl. Phys. A 80 (2005), 1625–1629.

[135] http://www.hexcel.com/NR/rdonlyres/B9DAF85C-DFA5-4158-8CE5-22A8F7146A94/0/HexFlowRTM6.pdf

[136] C. A. Cooper, S. R. Cohen, A. H. Barber, and H. D. Wagner, "Detachment of nanotubes from a polymer matrix," Applied Physics Letters 81 20 (2002), 3873-3875.

[137] ASTM D638-03, "Standard Test Method for Tensile Properties of Plastics," ASTM International (2003).

[138] R. F. Gibson, V. Anumandla, X. Wu, and D. Bettinger, "Experimental Characterization of Delamination in Unidirectional Carbon/Epoxy Composite Specimens Featuring a Carbon Nanotube-Enhanced Ply Interface," Proceedings of the SEM Annual Conference & Exposition on Experimental and Applied Mechanics (2005), 71-79.

[139] http://www.assda.asn.au/asp/index.asp?pgid=17971

[140] C. L. Cheung, A. Kurtz, H. Park, and C. M. Lieber, "Diameter-controlled Synthesis of Carbon Nanotubes," Journal of Physical Chemistry 106 (2002), 2429-2433.

[141] R. D. Bennett, A. C. Miller, N. T. Kohen, P. T. Hammond, D. J. Irvine, and R. E. Cohen, "Strategies for Controlling the Planar Arrangement of Block Copolymer Micelles and Inorganic Nanoclusters," Macromolecules 38 (2005), 10728-10735.

[142] R. D. Bennett, A. J. Hart, and R. E. Cohen, "Controlling the Morphology of Carbon Nanotube Films by Varying the Areal Density of Catalyst Nanoclusters Using Block Copolymer Micellar Thin Films," Advance Materials. Submitted for publication (2006).

[143] R. D. Bennett, A. J. Hart, A. C. Miller, P. T. Hammond, D. J. Irvine, and R. E. Cohen, "Patterning of Block Copolymer Micellar Thin Films Using Microcontact Printing and Applications in Carbon Nanotube Synthesis," Langmuir. Submitted for publication (2006).

[144] http://tds.loctite.com/tds5/docs/HYSA1C-EN.PDF

[145] http://www.microchem.com/products/pdf/SU8_2002-2025.pdf